Petrology, Zircon U-Pb Geochronology, and REE Geochemistry of Granulites from the Lützow-Holm Complex, East Antarctica: Implications for the *P-T-t* Evolution of Gondwana Collisional Orogens

January 2020

Yusuke TAKAMURA

Petrology, Zircon U-Pb Geochronology, and REE Geochemistry of Granulites from the Lützow-Holm Complex, East Antarctica: Implications for the *P-T-t* Evolution of Gondwana Collisional Orogens

A Dissertation Submitted to
the Graduate School of Life and Environmental Sciences,
the University of Tsukuba
in Partial Fulfillment of the Requirements
for the Degree of Doctor of Philosophy in Science
(Doctoral Program in Earth Evolution Sciences)

Yusuke TAKAMURA

Contents

Abstract

Zircon U-Pb geochronology is known as one of the best dating tools having been widely applied to various magmatic, metamorphic, and detrital grains. Particularly, the application of micro-analytical instruments such as SHRIMP and LA-ICP-MS to the dating technique enables us to precisely evaluate complex geological processes recorded in single zircon grains. For the determination of metamorphic ages, rare earth element (REE) patterns of zircons/monazites and coexisting minerals, particularly garnet, are often combined with U-Pb data to infer prograde, peak, and retrograde ages, which help our understanding of metamorphic processes in convergent plate margins. This study thus applies the technique in combination with petrological data to high-grade metamorphic rocks from the East African-Antarctic Orogeny (EAAO) formed through complex collisional events during late Neoproterozoic-Cambrian Gondwana amalgamation, and unravel pressure-temperature-time (*P-T-t*) evolution of the region. This study focuses on the Lützow-Holm Complex (LHC), East Antarctica, which is regarded as one of the regional high-grade metamorphic terranes in the EAAO. Previous studies suggested that the metamorphic grade systematically increases from the northeastern part (amphibolite facies) to the southwestern part (granulite facies) of the complex. Recent studies have proposed two stages of metamorphism in this area, however, these studies mainly focused on the southwestern granulite-facies area. This study particularly focused on high-grade rocks from Tenmondai Rock area, one of the exposures in the amphibolite to lower granulite transition zone along the Prince Olav Coast, northeastern LHC. In addition, a granulite from Sudare Rock area which is located in the southern part of the Lützow-Holm Bay is also examined to evaluate *P-T-t* paths throughout the LHC.

In this study, three mafic granulites (samples Ts11021003A, Ts11021007H, and Ts11021106A) and two amphibolites (Ts11021001A and Ts11021006B) collected from Tenmondai Rock, and one mafic granulite (Ts11011002A) from Sudare Rock have been analyzed. Skeletal garnet in sample Ts11021106A surrounded by orthopyroxene + plagioclase symplectite suggests the progress of reactions such as garnet + quartz → orthopyroxene + plagioclase, which indicate near-isothermal decompression probably along a clockwise *P-T* path. Similar symplectite textures are also present in sample Ts11011002A. Whole-rock geochemical data show characteristic Nb and Ti negative anomalies in spider diagrams, depletion of HREE, and Th-enriched characters in some discrimination diagrams, suggesting a magmatic arc-related setting. The application of phase equilibrium modeling in the system NCKFMASHTO for the garnet-bearing mafic granulite (Ts11021106A) indicates that the peak assemblage (garnet + orthopyroxene + plagioclase + ilmenite + quartz + K-feldspar and melt) was stable at a *P-T* range of 850-900°C and 7.5-8.5 kbar. The condition is consistent with the result of geothermobarometry (805-845°C at 8 kbar and 6.5-9.3 kbar at 800°C), which also confirms that the area underwent peak granulite-facies metamorphism, higher than previous results (750°C and 7.2-7.5 kbar). The application of geothermobarometry to the sample from Sudare Rock (Ts11011002A) yielded granulite-facies peak *P-T* conditions. In addition, U-Pb dating of zircons in mafic granulites from Tenmondai Rock (Ts11021106A) and Sudare Rock (Ts11011002A) were performed by LA-ICP-MS, and yielded similar middle Neoproterozoic ages (ca. 800-700 Ma) from igneous zircon cores and late Neoproterozoic to Cambrian ages (ca. 650-500 Ma) from metamorphic rims and/or structureless grains. Metamorphic zircons in sample Ts11021106A (Tenmondai Rock) show enriched normalized-Lu/Gd values and negative Eu/Eu* $(=\mathrm{Eu_N}/(\mathrm{Sm_N}\times\mathrm{Gd_N})^{1/2})$ anomalies for ca. 520-510 Ma zircon. These results suggest the consumption of garnet and the growth of plagioclase caused by the breakdown of garnet and formation of orthopyroxene + plagioclase symplectite during near-isothermal decompression. In sample Ts11011002A (Sudare Rock), although no Eu/Eu* anomaly was observed, the normalized Lu/Gd values increase at ca. 560-510 Ma. This might suggest that the timing of near-isothermal decompression caused by rapid exhumation in Sudare Rock could be earlier than that of Tenmondai Rock.

The published U-Pb and REE data of zircons in mafic rocks with similar symplectite textures from the Highland Complex, Sri Lanka, show older zircon ages of ca. 560-520 Ma with higher Lu/Gd values. This indicates a correlation between the central LHC and the Highland Complex, and is consistent with previous studies that inferred petrological, geochemical and geochronological similarities between the two complexes. The obtained *P-T-t* path can be well compared with model *P-T-t* path predicted by channel flow as a potentially dominant mechanism of rapid exhumation of Gondwana collisional orogen.

Keywords: Gondwana, the Lützow-Holm Complex, *P-T-t* path, Zircon U-Pb dating, Rare earth element, symplectite, channel flow

List of Figures

List of Tables

Chapter 1. Introduction

Previous petrological, geochemical and geochronological studies on the East African-Antarctic Orogen (EAAO), exposed in East Africa-India-Sri Lanka-East Antarctica region, suggest that this orogen was formed through complex subduction-accretion-collision processes of various Neoproterozoic arc components and Meso- to Neoarchean microcontinents during the latest Neoproterozoic to Cambrian Gondwana amalgamation (e.g., Meert, 2003; Jacobs and Thomas, 2004; Collins and Pisarevsky, 2005; Collins et al., 2007a, b, 2014; Meert and Lieberman, 2008; Santosh et al., 2009, 2014, 2015, 2016, 2017). The Lützow-Holm Complex (LHC) of East Antarctica is a granulite- and amphibolite-facies terrane formed during Neoproterozoic to Cambrian high-grade metamorphism, which is comparable with the timing of the EAAO (e.g., Hiroi et al., 1991: Shiraishi et al., 1994). Recent geochemical and geochronological studies proposed that the LHC is composed of Neoarchean (ca. 2.5 Ga), Paleoproterozoic (ca. 1.8 Ga) and Neoproterozoic (ca. 1.0 Ga) magmatic components collided together during the final amalgamation stage of Gondwana (e.g., Dunkley et al., 2014; Takahashi et al., 2018). The LHC has been correlated with other Gondwana regions, particularly Sri Lanka. Yoshida et al. (1992) proposed that the metasedimentary units exposed along Lützow-Holm Bay region (Ongul and Skallen Group) could be correlated to those of the Highland Complex, Sri Lanka. The LHC and the Highland Complex are also interpreted as a supracrustal basin developed in a suture zone during Gondwana amalgamation (e.g., Shiraishi et al., 1994). Kazami et al. (2016) reported geochemical and geochronological features of orthogneisses from Akarui Point located on the northeastern part of the LHC and argued their similarities with the Kadugannawa Complex of Sri Lanka. Neoproterozoic (ca. 1.0 Ga) volcanic arc affinities in the LHC has been compared with the Vijayan Complex of Sri Lanka, which is also regarded as Neoproterozoic magmatic arc, and interpreted to have been a single Neoproterozoic volcanic arc called 'northern LH-Vijayan Complex' (Tsunogae et al., 2015, 2016; Takahashi et al., 2018). Takamura et al. (2018) also correlated the LHC to the Highland Complex of Sri Lanka as parallel suture zones based on the age distribution of detrital zircons in metasediments. Kitano et al. (2018), however, proposed another model suggesting that the Highland and Wanni Complexes could be correlated with Skallen Group and Ongul-Okuiwa Groups in the LHC, respectively, based on the ages of igneous zircons in orthogneisses.

Similarities of metamorphic pressure and temperature *(P-T)* conditions between the LHC and the Highland Complex have also been discussed (e.g., Yoshida et al., 1992; Takamura et al., 2015; Osanai et al., 2016a). Both Skallen Group (southwestern part of the LHC) and the Highland Complex (Sri Lanka) were proposed as a granulite-facies metamorphic terrane, particularly including ultrahigh-temperature (UHT) metamorphic rock (e.g., Kriegsman and Schumaher, 1999; Osanai et al., 2004, 2006, 2016a; Sajeev and Osanai, 2004a, 2004b; Sajeev et al., 2007; Yoshimura et al., 2008; Kawasaki et al., 2011; He et al., 2018). Recent studies also show similar clockwise *P-T* paths from the two regions suggesting similar metamorphic processes during late Neoproterozoic collisional event (e.g., Sajeev et al., 2007; Yoshimura et al., 2008; Kawakami and Hokada, 2010; Kawasaki et al., 2011; Takamura et al., 2015; Osanai et al., 2016a; Dharmapriya et al., 2017).

The timing and duration of metamorphism can also be one of the keys to understand the metamorphic process and evaluate the spatial and temporal relationship among metamorphic terranes. U-Pb dating using zircon and/or monazite has been widely applied to various metamorphic rocks because of high closure temperature of U-Pb system and physical/chemical durability of the minerals. Some previous studies carried out zircon and monazite U-Pb dating for both the LHC and Sri

Lankan terranes, and yielded older (~650-580 Ma) and younger (~560-500 Ma) metamorphic age populations suggesting polymetamorphism (e.g., Hokada and Motoyoshi, 2006; Kawakami et al., 2016; Osanai et al., 2016b). He et al. (2018), however, proposed 'long-lived metamorphism' that continued over 100 m.y. from late Neoproterozoic (ca. 660 Ma) to Cambrian (ca. 520 Ma) based on petrological *P-T* estimations, zircon U-Pb geochronology, and rare earth element geochemistry of mafic granulites from the Highland Complex.

Previous studies attempted to link metamorphic pressure and temperature *(P-T)* conditions and mineral isotopic dating using trace elements in zircon and/or monazite (e.g., Rubatto, 2017 and references therein) for understanding *P-T* evolution of orogenic belts. Particularly, rare earth elements (REE) in these accessory minerals are well studied because the growth and consumption of REE-bearing host minerals can control enrichment and depletion of REE content in accessory minerals. For example, zircons in equilibrium with garnet show flat normalized heavy REE (HREE) pattern because garnet is the main host mineral for HREE (e.g., Rubatto, 2002; Whitehouse and Platt, 2003). In addition, feldspar is well known as an effective host of Eu and yields negative Eu anomaly of coexisting minerals (e.g., Rubatto, 2002; Buick et al., 2010). Some previous studies applied these features as indicators of garnet and/or feldspar growth and/or consumption during the progress of metamorphism, and they made a linkage to petrological *P-T* estimation (e.g., Imayama et al, 2012; Rubatto et al., 2013). Applications of 'petrochronology' have also been adopted to evaluate the timing and duration of metamorphism in Gondwana collisional orogeny (e.g., Kadowaki et al., 2019).

P-T-time (*P-T-t*) paths can be a key to compare the metamorphic processes among different terranes. In addition, *P-T-t* paths can be used for evaluation of the mechanism of deformation and/or exhumation; for example, Kohn et al. (2008, 2014) compared two modeled *P-T-t* paths (based on 'channel flow model' [e.g., Beaumont et al., 2001, 2004; Jamieson et al., 2002, 2004] and 'critical taper model' [e.g., Henry et al., 1997; Bolinger et al., 2006], respectively) and observed *P-T-t* paths of metamorphic rocks in the Himalayan range, and inferred the mechanism of exhumation. Thus, the *P-T-t* path obtained for metamorphic rock can be a key to unravel the evolution process of orogens on the past Earth.

This study reports new petrological, geochemical and zircon U-Pb geochronological data from the northeastern LHC, one of the regions with limited previous studies of *P-T-t* evolution. In addition, REE contents in zircon from northeastern and southwestern parts of the LHC have been analyzed to identify several age groups, link them to growth and/or consumption of the minerals caused by changing metamorphic *P-T* conditions, and unravel *P-T-t* paths of the study areas. Finally, the data are compared with the zircon U-Pb and REE data from other Gondwana fragments to evaluate the *P-T-t* evolution of Gondwana collisional orogen, particularly the timing of exhumation.

Chapter 2. Geological background

2.1. The Lützow-Holm Complex, East Antarctica

2.1.1. General geology and metamorphism

The Lützow-Holm Complex (LHC) is located from northeast to southwest along Prince Harald and Prince Olav Coasts of East Antarctica (Fig. 1). Its boundary between the western Rayner Complex to the east, and the Yamato-Belgica Complex and the Sør Rondane Mountains to the west and south, are not exposed. The LHC is dominantly composed of felsic to intermediate orthogneisses (charnockite, biotite-hornblende gneiss, dioritic gneiss) with various metasediments (pelitic and psammitic rocks, quartzite, and marble) and metabasites (mafic granulite, amphibolite, and ultramafic rock) (e.g., Shiraishi et al., 1989). Previous petrological and geothermobarometric studies have indicated that its metamorphic grade increases from amphibolite facies in the northeast to granulite facies in the southwest (e.g., Hiroi et al., 1991; Tsunogae et al., 2015) (Fig. 1). The highest-grade metamorphic rocks are exposed at Rundvågshetta in the southwesternmost part of the complex. The peak *P-T* condition of Rundvågshetta has been estimated at 1040°C and 13-15 kbar that was followed by retrograde metamorphism of 950°C at 8 kbar and 830°C at 6.1 kbar along a clockwise *P-T* path (Kawasaki et al., 2011). Similar UHT conditions have been reported from granulites in adjacent localities, such as Skallen and Skallevikshalsen (Osanai et al., 2004; Yoshimura et al., 2004). In contrast, Tsunogae et al. (2014) estimated peak *P-T* condition for charnockites from Rundvågshetta and adjacent Vesleknausen as 800-850°C and suggested that the UHT event is a local phenomenon and only recorded in dry Mg-Al-rich pelitic rocks in this region. Lower peak metamorphic *P-T* conditions have been estimated from the transition zone between granulite- and amphibolite-facies zones such as 770-880°C at 6-9 kbar from Byôbu Rock and Gobanme Rock (Satish-Kumar et al., 2006), 750°C at 7.2-7.5 kbar from Tenmondai Rock (Hiroi et al., 1983a), and 770-790°C at 7.7-9.8 kbar from Akarui Point (Kawakami et al., 2008). In contrast, higher temperatures of 825-900°C were obtained from Akarui Point by the application of ternary-feldspar geothermometry (Nakamura et al., 2013). Iwamura et al. (2013) reported the first evidence of peak UHT metamorphism (900-920°C at 5-6 kbar) and clockwise P-T path from sapphirine- and spinel-bearing metagabbro of Akarui Point, and proposed that the LHC might be further separated into several crustal blocks by shear zones as inferred from geophysical data of Nogi et al. (2013).

2.1.2. Geochronology

Available geochronological data from the LHC suggest late Neoproterozoic to early Cambrian (550-520 Ma) high-grade metamorphism (e.g., Asami et al., 1997; Hokada and Motoyoshi, 2006; Shiraishi et al., 1994, 2003, 2008; Tsunogae et al., 2014, 2015, 2016). Shiraishi et al. (1994) performed systematic SHRIMP zircon U-Pb dating for ortho- and paragneisses from several localities in the LHC (e.g., Austhovde, Rundvågshetta, Telen, Ongul, Akarui Point) and obtained peak metamorphic ages as 550-520 Ma. Asami et al. (1997) reported CHIME ages for monazite in biotite gneisses from East Ongul and Mt. Vechernyaya as 537-533 Ma. Satish-Kumar et al. (2006) performed electron microprobe dating of monazites from Byôbu Rock and obtained late Neoproterozoic ages (ca. 660-480 Ma) with the average apparent age of 557±33 Ma. Hokada and Motoyoshi (2006) also performed CHIME monazite age dating for pelitic granulites from Skallen and obtained two age groups; 650-580 Ma (prograde metamorphic age) and 560-500 Ma (peak metamorphic age). Dunkley (2007) reported a spread of SHRIMP zircon age from ca. 600 to 500 Ma, and inferred that the 550-530 Ma event corresponds to retrograde metamorphism of the LHC after the peak metamorphism at >550 Ma. Tsunogae et al. (2014) obtained 591 Ma and 548 Ma SHRIMP zircon ages from a partially melted feldspathic rock from Vesleknausen and interpreted the ages as the timing of partial-melting stage and retrograde metamorphic age, respectively, suggesting that the peak metamorphism took place between 591 and 548 Ma. Fraser et al. (2000) reported K/Ar and ^{40}Ar/^{39}Ar ages of hornblende and biotite in granulites from Rundvågshetta, and inferred this region cooled to ca. 350°C to ca. 300°C by ca. 500 Ma. Nakajima et al. (1988) obtained Rb-Sr whole-rock isochron age of migmatitic gneisses from Tenmondai Rock as 780±70 Ma. Rb-Sr mineral isochron age obtained for hornblende-biotite gneiss from Oku-iwa Rock (431±14 Ma) has also been regarded as a cooling age (Kawano et al., 2006).

Nd-model ages from the northeastern (eastern Prince Olav Coast and northern Sôya Coast) and western LHC (Prince Harald Coast) show late Mesoproterozoic to early Neoproterozoic ages (ca. 1.25-1.0 Ga) (Shiraishi et al., 2008 and references therein). In contrast, those from the southern LHC (southern Sôya Coast) indicate Neoarchean to early Paleoproterozoic ages (ca. 2.70-2.29 Ga). Shiraishi et al. (2003) reported early Neoproterozoic zircon U-Pb ages from orthogneisses including trondhjemite from Cape Hinode (1040-913 Ma) and hornblende-biotite gneiss from Innhovde (1028, 992 and 924 Ma), and proposed possible arc magmatism during early Neoproterozoic. Tsunogae et al. (2015) also reported early Neoproterozoic zircon U-Pb ages (999-965 Ma) for felsic orthogneisses from Kasumi Rock, Tama Point, Innhovde and Futatu-iwa. Kazami et al. (2016) obtained slightly younger but nearly consistent magmatic ages (847 Ma) with some older xenocrysts (1026-881 Ma) and ages of subsequent thermal events (807-667 Ma) for felsic orthogneiss from Akarui Point. On the other hand, Shiraishi et al. (1994, 2008) reported Neoarchean (ca. 2.5 Ga) magmatic zircons from Ongul and

Rundvågshetta regions. Tsunogae et al. (2014, 2016) also obtained similar 2.5 Ga magmatic ages from charnockite and mafic granulite from Vesleknausen and Sudare Rock and suggested Neoarchean crustal growth. Some recent studies reported Paleoproterozoic magmatic zircon ages of ca. 2.1-1.8 Ga from orthogneisses from Austhovde, Skallevikshalsen, Skallen, and Telen (Dunkley et al., 2014; Takahashi et al., 2018). Shiraishi et al. (1994, 2003) analyzed zircons in metasediments and obtained Archean to Paleoproterozoic ages (2887-1855 Ma) from West Ongul, Telen, and Rundvågshetta. They also reported Neoproterozoic ages from zircon in a metasediment from Telen (1064-966 Ma). Dunkley et al. (2014) also reported Archean to Paleoproterozoic (3.3-1.8 Ga) U-Pb detrital zircon ages from Botnnuten, Rundvågshetta, Skallevikshalsen, Telen and Skarvsnes, and Mesoproterozoic to Neoproterozoic ages (1.3-0.62 Ga) from Skarvsnes and East Ongul. Takamura et al. (2018) performed systematic U-Pb dating for detrital zircons and obtained late Meso- to Neoproterozoic ages (1.1-0.63 Ga) and Neoarchean to Paleoproterozoic ages (2.8-2.4 Ga) from the northeastern (Tenmondai Rock, Akarui Point, West Ongul and Langhovde) and southwestern (Skallevikshalsen, Sudare Rock and Austhovde) LHC, respectively.

2.2 Geological outline of the study area

2.2.1. Tenmondai Rock

Tenmondai Rock is an exposure located near the northeasternmost part of the 'transitional zone' of Hiroi et al. (1991) in the Prince Olav Coast (Fig. 1). The dominant lithologies of this area are biotite- and hornblende-bearing gneiss and migmatitic biotite- and hornblende-bearing gneiss with minor garnet- and biotite-bearing gneiss, amphibolite, gneissose granite, and pelitic gneiss. They are elongated parallel to the regional NW-SE foliation and intruded by discordant granite and pegmatite (Fig. 2). Hiroi et al. (1983b) reported the coexistence of three polymorphs of aluminum silicate (sillimanite, kyanite, and andalusite) in spinel-andalusite-bearing kyanite-sillimanite-garnet-biotite gneiss from Tenmondai Rock, and regarded sillimanite as stable phase at the peak metamorphism, kyanite as metastable relic, and andalusite as a later phase formed during thermal event related to emplacement of granite and pegmatite. Hiroi et al. (1983a) proposed peak metamorphic *P-T* condition as ca. 7.2-7.5 kbar at 750°C based on garnet-biotite geothermometers (Thompson, 1976; Goldman and Albee, 1977; Ferry and Spear, 1981) and garnet-plagioclase-sillimanite-quartz geobarometer (Newton and Haselton, 1981). Recently, Baba et al. (2019) reconsidered metamorphic conditions for pelitic gneisses of Tenmondai Rock using geothermobarometry and mineral equilibrium modeling. They have suggested peak *P-T* conditions as 8-9 kbar and 750-800 °C and subsequent near-isobaric cooling. Nakajima et al. (1988) reported Rb-Sr whole-rock ages as 780±70 Ma, although they questioned the quality of their own geochronological data. Dunkley et al. (2014) reported SHRIMP zircon U-Pb ages of 581±7 Ma and 540±7 Ma from sillimanite-bearing metamorphosed granitic dyke as protolith and metamorphic ages, respectively.

2.2.2. Sudare Rock

Sudare Rock is a small exposure located on the Sôya Coast, the southwestern part of the LHC (Fig. 1). The dominant lithologies of the region are pelitic gneiss, biotite-hornblende gneiss, charnockite, marble, calc-silicate gneiss, and ultramafic rock. All of these rocks show NW-SE trending foliation dipping gently toward NE as defined by thin alternation of the lithologies (Fig. 3). Some previous studies suggested

Neoarchean to Paleoproterozoic (ca. 2500-2200 Ma) protolith ages based on U-Pb geochronology of zircons in charnockite (Dunkley et al., 2014; Tsunogae et al., 2016) and pelitic gneiss (Takamura et al., 2018). Tsunogae et al. (2016) also reported the zircon Lu-Hf isotopic data indicating that the protolith magma was sourced from Paleo- to Neoarchean juvenile components mixed with reworked ancient crustal materials. Metamorphic *P-T* conditions were calculated using a hornblende-plagioclase geothermometer for charnockite as 740-760 °C at 7 kbar, which corresponds to the condition of a retrograde stage (Tsunogae et al., 2016).

Chapter 3. Petrography and Geochemistry

3.1. Petrography

In this study, 38 samples from eight outcrops of Tenmondai Rock and three samples from one outcrop of Sudare Rock collected by the 52nd Japanese Antarctic Research Expedition (JARE-52) during 2010-2011 were examined. Particularly, five metabasites of Tenmondai Rock and one metabasite of Sudare Rock were analyzed in detail (Tables 2 and 3). The sample localities are shown in Figures 2 and 3. Polished thin sections were prepared for petrographic study at the University of Tsukuba, Japan. A brief description of the localities and their geological features, as well as salient petrographic characters of the examined samples, are given below.

3.1.1. Tenmondai Rock

3.1.1.1. Ts11021001A

Sample Ts11021001A is a garnet-bearing amphibolite collected from the northeastern part of Tenmondai Rock (S68° 26’ 39.98”; E41° 43’ 26.075”). It occurs as a boudin of about a few m in length (Fig. 4a). In hand specimen, the rock has no foliation and lineation. It is characterized by the existence of coarse-grained porphyroblastic garnet in medium-grained matrix. The rock consists of plagioclase (40-50 vol. %), amphibole (30-40 vol. %), garnet (~5 vol. %), biotite (<5 vol. %), quartz (<5 vol. %), ilmenite (5-10 vol. %) and accessory apatite and zircon (Figs. 4b, 5a, b). Plagioclase is xenoblastic and medium grained (0.2-0.5 mm). Greenish-brown amphibole is subidioblastic and medium to coarse grained (0.3-1.0 mm). Garnet occurs as porphyroblastic, subidioblastic to xenoblastic, and fine to medium (0.1-1.0 mm) grains, and contains many inclusions such as apatite, plagioclase, and quartz. Fine- to medium-grained (0.1-1.0 mm) xenoblastic biotite mostly coexists with amphibole and/or opaque minerals. Quartz is xenoblastic, fine to coarse grained, and shows weak wavy extinction. Most ilmenites show lamellae which are composed of hematite. In addition, some Fe-Ti oxides contain fine-grained pyrite inclusions.

3.1.1.2. Ts11021003A

Sample TS11021003A is a mafic granulite that occurs as a boudin of about a few 10 cm in length within foliated garnet-biotite gneiss (Fig. 4d). This rock is medium grained without foliation. It is composed of plagioclase (40-50 vol. %), orthopyroxene (20-30 vol. %), amphibole (20-30 vol. %), biotite (10-20 vol. %), quartz (5-10 vol. %), and Fe-Ti oxide (mainly ilmenite) (<5 vol. %) as well as fine-grained zircon and apatite as accessory minerals (Figs. 5c, d). Xenoblastic and medium- to coarse-grained (0.5-1.5 mm) plagioclase shows core-rim texture under crossed-polar observation (Fig. 5d). Orthopyroxene is xenoblastic and fine to medium grained (0.1-0.5 mm). Amphibole occurs as greenish-brown, subidioblastic to xenoblastic, and fine to coarse grained (0.1-2.0 mm). Fine- to coarse-grained (0.3-1.5 mm) biotite is subidioblastic. Orthopyroxene, amphibole, and biotite are often associated (Figs. 5c, d). Quartz is medium to coarse grained (0.5-1.5 mm) and fills the matrix of other minerals. Ilmenite contains lamellae of hematite.

3.1.1.3. Ts11021006B

Sample Ts11021006B is an amphibolite from Tenmondai Rock (S68° 26’ 34.66”; E41°

42’ 54.899”). It occurs as lenses within quartzofeldspathic gneiss and is associated with small ultramafic blocks (Figs. 4e, f). The rock consists of plagioclase (50-60 vol. %), amphibole (20-30 vol. %), biotite (10-20 vol. %), and calcite (<5 vol. %) (Figs. 5e, f) with accessory zircon, apatite, and opaque minerals composed of ilmenite with hematite lamellae, pyrite, and chalcopyrite. Plagioclase and amphibole show granoblastic texture (Fig. 5e). Plagioclase is subidioblastic to xenoblastic, and medium to coarse grained (0.5-3.0 mm). Greenish-brown amphibole is subidioblastic and medium to coarse grained (1.0-3.0 mm). Some parts of amphibole are replaced by calcite (Fig. 5f). Coarse-grained (1.0-2.0 mm) biotite show subidioblastic shape and is often associated with amphibole and opaque minerals.

3.1.1.4. Ts11021007H

Sample Ts11021007H is a mafic granulite from Tenmondai Rock (S68° 26’ 38.039”; E41° 42’ 47.124”). It occurs as boudins within foliated pelitic gneiss with a pegmatite intrusion (Figs. 4g, h). This rock occurs as the core of a boudin surrounded by garnet-rich mafic layer (Fig. 4g). In hand specimen, the rock is medium to coarse grained without any foliation and lineation (Fig. 4h). The sample is composed of plagioclase (30-40 vol. %), amphibole (20-30 vol. %), orthopyroxene (10-20 vol. %), biotite (10-20 vol. %), quartz (5-10 vol. %), opaque mineral (5-10 vol. %) and accessory apatite and zircon (Figs. 5g, h). Plagioclase is xenoblastic and fine to medium grained (0.1-1.0 mm), and shows core-rim texture under crossed-polar observation. Greenish-brown amphibole is subidioblastic to xenoblastic and medium grained (0.5-1.0 mm). Orthopyroxene is subidioblastic and fine to coarse grained (0.1-3.0 mm). Subidioblastic and medium- to coarse-grained (0.5-1.5 mm) biotite often coexist with amphibole and orthopyroxene, and shows radial aggregate (Fig. 5g). Xenoblastic and fine- to medium-grained (0.1-1.0 mm) quartz fills the matrix of other subidioblastic mineral grains. Opaque minerals are medium grained (0.3-0.5 mm) and xenoblastic, and composed of Fe-Ti oxide with/without lamellae of hematite. Accessory zircon and apatite are very fine-grained (<0.1 mm) and idioblastic to subidioblastic.

3.1.1.5. Ts11021106A

Sample Ts11021106A is a mafic granulite collected from Tenmondai Rock (S68° 26' 41.64"; E41° 43' 4.368"). It occurs as lenses of about a few m in length within foliated pelitic gneiss. The hand specimen shows no obvious foliation or lineation (Figs. 4i, j). The rock is mostly medium to coarse grained, however, coarse-grained garnet occurs as porphyroblast (Fig. 4j). It consists of plagioclase (30-40 vol. %), biotite (15-20 vol. %), quartz (10-15 vol. %), orthopyroxene (10-15 vol. %), garnet (5-10 vol. %), and accessory apatite, zircon, rutile, Fe-Ti oxide (mainly ilmenite), pyrite, and chalcopyrite (Figs. 6a-d). Plagioclase is xenoblastic and fine to medium grained (0.1-1.0 mm), some of which show obscure-shaped core (Pl_1)-rim (Pl_2) texture under crossed-polar observation. Biotite is xenoblastic to subidioblastic and fine to medium grained (0.3-1.0 mm). Xenoblastic and fine- to medium-grained quartz (0.1-1.0 mm) shows weak wavy extinction. Orthopyroxene in matrix (Opx_1) is subidioblastic and medium to coarse grained (0.5-1.5 mm), and rarely present as intergrowth with opaque minerals. Porphyroblastic garnet is skeletal in shape, medium to coarse grained (1.0-3.0 mm), and contains numerous inclusions of apatite, plagioclase, quartz, rutile, and polycrystalline inclusions with well-developed negative crustal shape (Fig. 6i). The garnet is partly surrounded by symplectite composed of fine-grained (<0.5 mm) orthopyroxene and plagioclase (Opx_2 and Pl_2, respectively) with minor Fe-Ti oxide and biotite. These textures suggest the progress of the following FMAS continuous reaction

(1):

$$\mathrm{Grt + Qtz \pm melt \rightarrow Opx + Pl \pm Ilm \pm Bt} \qquad (1)$$

The above reaction texture has been reported from many high-grade terranes worldwide (e.g., Harley, 1989) probably suggesting near-isothermal decompression or decompressional cooling after peak metamorphism.

Idioblastic to subidioblastic and fine-grained (0.1-0.5 mm) apatite occurs either in matrix or as inclusions in garnet. Zircon grains show rounded shape and are very fine grained (<0.1 mm), and mostly occur in the matrix. Rutile is also very fine grained (<0.1 mm) and idioblastic to subidioblastic, and occurs only as inclusions in garnet. Fine- to medium-grained (0.5-1 mm) and xenoblastic Fe-Ti oxide shows hematitic lamellae and some grains contain pyrite and chalcopyrite as inclusion (Fig. 6d). They occur only in the matrix, and no inclusion of Fe-Ti oxide is found in garnet. These may suggest that rutile was formed together with garnet during prograde metamorphism, whereas Fe-Ti oxide has grown during peak to retrograde stage, after the breakdown of garnet. Polycrystalline inclusions with negative-crustal shape in garnet might be evidence of the existence of some kind of melt. The inclusions are mainly composed of calcite and hydrous silicates such as pyrophyllite (Fig. 6i).

3.1.2. Sudare Rock

3.1.2.1. Ts11011002A

Sample Ts11011002A is a mafic granulite collected from Sudare Rock (S69° 42' 39.96"; E39° 12' 41.58") and occurs as a boudin with foliated garnet-biotite gneiss and quartzofeldspathic gneiss (Fig. 4k). In hand specimen, the rock is medium-grained with no foliation, and contains porphyroblastic coarse-grained garnet surrounded by plagioclase (Fig. 4l). It consists of plagioclase (40-50 vol. %), clinopyroxene (15-20 vol. %), amphibole (15-20 vol. %), biotite (5-10 vol. %), Fe-Ti oxide (mainly ilmenite) (5-10 vol. %), garnet (<5 vol. %), orthopyroxene (<5 vol. %) with accessory quartz, zircon and apatite (Figs. 7a-d). Xenoblastic and fine- to medium-grained (0.1-1.0 mm) plagioclase is the main component of the matrix (Pl_1). Clinopyroxene is medium grained (0.5-1.0 mm) and subidioblastic. Greenish brown amphibole is subidioblastic and medium to coarse grained (0.5-1.5 mm). Biotite is fine to medium grained (0.1-1.0 mm) and subidioblastic. Fine- to medium-grained (0.2-1.0 mm) and subidioblastic to xenoblastic Fe-Ti oxide, pyrite, and minor chalcopyrite occur in matrix and/or in garnet as inclusions. Coarse-grained and subidioblastic garnet (1.0-5.0 mm) occurs as porphyroblast containing numerous inclusions of apatite, plagioclase, quartz, Fe-Ti oxide, pyrite and chalcopyrite. Minor orthopyroxene also occur as medium-grained (0.5-1.0 mm) and subidioblastic mineral (Opx_1). Garnet is partly surrounded by symplectite which consists of orthopyroxene (Opx_2) and plagioclase (Pl_2) suggesting the progress of the following FMAS continuous reaction possibly caused by near-isothermal decompression:

$$\mathrm{Grt + Qtz \rightarrow Opx + Pl} \qquad (2)$$

Quartz is very minor in this sample, however, it remains as fine-grained inclusions (<0.2 mm) in plagioclase and garnet (Figs. 7e-i). In addition, idioblastic and fine-grained (0.1-0.5 mm) apatite and zircon occur widely in the thin section.

3.2. Mineral chemistry

Mineral chemical analyses were carried out using an electron microprobe analyzer (JOEL JXA8530F) at the Chemical Analysis Division of the Research Facility Center for Science and Technology, the University of Tsukuba. The analyses were performed under conditions of 15 kV accelerating voltage and 10 nA sample current for all minerals, and the data were regressed using an oxide-ZAF correction program supplied by JEOL.

3.2.1. Garnet

The garnet in an amphibolite (Ts11021001A) from Tenmondai Rock shows higher X_{Mg} (=Mg/(Fe + Mg)) (0.324-0.381), spessartine component (=Mn/(Fe + Mg + Ca + Mn)x100), and slightly higher grossular-component (=Ca/(Fe + Mg + Ca + Mn)x100) ($Alm_{37-44}Pyr_{19-23}Grs_{14-23}Spr_{13-26}$) than that in mafic granulite from the same region (Ts11021006A) (0.239-0.302, $Alm_{57-65}Pyr_{20-25}Grs_{9-19}Spr_{2-5}$). Garnet in mafic granulite from Sudare Rock (Ts11011002A) is enriched in grossular (0.199-0.278, $Alm_{52-60}Pyr_{15-21}Grs_{18-24}Spr_{3-5}$) (Figs. 8e, f). In addition, the core of garnet in Ts11021001A is enriched in grossular and depleted in spessartine components ($Alm_{37-44}Pyr_{22-23}Grs_{19-23}Spr_{13-20}$) than those of rim ($Alm_{37-41}Pyr_{19-23}Grs_{14-16}Spr_{23-26}$). In contrast, garnet in sample Ts11021106A is compositionally nearly homogeneous, although Ca-rich portions occur as ‘islands’ ($Alm_{57-60}Pyr_{20-25}Grs_{14-19}Spr_{2-3}$) surrounded by Ca-poor parts ($Alm_{60-65}Pyr_{22-25}Grs_{9-14}Spr_{3-5}$) with skeletal and porphyroblastic garnet grains (Figs. 6e-h). Although garnet in Ts11011002A is mostly homogeneous ($Alm_{57-60}Pyr_{15-21}Grs_{18-20}Spr_{3-5}$), some grains in the sample are slightly Ca-rich and Fe-poor ($Alm_{52-53}Pyr_{19.9-20.2}Grs_{1924.2-24.3}Spr_{2.8-3.2}$) (Figs. 7e-h). In this study, Ca-rich ‘islands’ and Ca-poor matrix of garnet are regarded as core and rim, respectively.

3.2.2. Pyroxenes

The orthopyroxenes in the examined samples are mostly classified as enstatite (Fig. 8c). The X_{Mg} of orthopyroxene in samples Ts11021106A (Tenmondai Rock) and Ts11011002A (Sudare Rock) (garnet-bearing mafic granulite) are lower (0.537-0.560 and 0.485-0.500, respectively) than those of garnet-free mafic granulites from Tenmondai Rock (Ts11021003A and Ts11021007H; 0.612-0.658 and 0.588-0.594, respectively). Symplectitic orthopyroxene in sample Ts11021106A is slightly enriched in Al content (0.092-0.118 pfu) than that of orthopyroxene in matrix (0.080-0.099 pfu). Although orthopyroxene in sample Ts11011002A is compositionally nearly homogeneous in terms of X_{Mg} and Al content, Ca content of symplectitic orthopyroxene is slightly higher (0.030 pfu) than that in matrix (0.020 pfu). The clinopyroxene in sample Ts11011002A is Mg-rich (X_{Mg} = 0.606-0.612) and compositionally nearly homogeneous in terms of Fe-Mg ratio (Fig. 8c).

3.2.3. Plagioclase

The plagioclase in amphibolites (Ts11021001A and Ts11021006B) show albite-rich composition ($An_{34-43}Ab_{56-61}Or_{0.9-1.3}$ and $An_{24-27}Ab_{72-74}Or_{0.7-1.6}$, respectively) than those of mafic granulites (Fig. 8d). Although plagioclase in mafic granulites from Tenmondai Rock shows relatively higher anorthite component, it shows wide compositional ranges. Particularly, plagioclase in matrix has compositional zoning; relatively anorthite-poor core (Ts11021003A: $An_{49-52}Ab_{47-50}Or_{0.6-0.8}$, Ts11021007H: $An_{46-48}Ab_{51-53}Or_{0.6-0.7}$, and Ts11021106A: $An_{54-60}Ab_{39-47}Or_{0.6-1.2}$) and anorthite-rich rim (Ts11021003A: $An_{76-85}Ab_{15-23}Or_{0.1-0.3}$, Ts11021007H: $An_{72-78}Ab_{22-28}Or_{0.1-0.4}$, and Ts11021106A:

$An_{75-85}Ab_{15-25}Or_{0.2-0.6}$) (Figs. 5d, 5h, 6c and 8d). In addition, compositions of plagioclase inclusion in garnet and symplectitic plagioclase in sample Ts11021106A indicate higher anorthite component ($An_{82-84}Ab_{16-18}Or_{0.1-0.2}$ and $An_{75-85}Ab_{15-25}Or_{0.2-0.6}$, respectively), which overlap with the composition of rim of the matrix plagioclase (Pl_2) (Figs. 6e-h, 8d). On the other hand, plagioclase in matrix and in garnet within sample Ts11011002A from Sudare Rock shows albite-rich composition ($An_{44-50}Ab_{48-53}Or_{2-3}$), while that forming symplectite is anorthite-rich ($An_{82}Ab_{17}Or_{0.4-0.5}$) (Figs. 7g, 8d).

3.2.4. Biotite

The biotite in most samples shows a negative correlation of TiO_2 with X_{Mg} (Fig. 8b) Particularly, rim of biotite in samples Ts11021003A and Ts11021007H tends to be enriched in X_{Mg} (0.672-0.707) and depleted in TiO_2 content (2.73-3.72 wt. %) than those of core (0.660-0.675, 3.36-3.99 wt.%, respectively). In contrast, rim of biotite in samples Ts11021001A and Ts11021106A indicates slightly higher TiO_2 content (3.08-4.26 wt. %) than that of core (2.63-3.84 wt. %). Biotite in sample Ts11011002A from Sudare Rock shows the lowest X_{Mg} (0.516-0.523) and the highest TiO_2 content (5.59-5.71 wt. %) among examined samples (Fig. 8b).

3.2.5. Calcic amphibole

The calcic amphibole in the analyzed samples from Tenmondai Rock are characterized by high Ca and Na + K contents of 1.68-1.88 per formula unit (pfu) and 0.53-0.84 pfu, respectively, and is classified mostly as edenite and pargasite (Fig. 8a). On the other hand, calcic amphibole in sample Ts11011002A (Sudare Rock) shows slightly lower X_{Mg} (0.485-0.487) than other samples from Tenmondai Rock (0.563-0.640), and is classified as ferro-pargasite (Fig. 8a). Compositional zoning is observed for amphiboles from some samples. For example, rim of amphibolite in samples Ts11021003A and Ts11021006B is slightly enriched in Si and depleted in Na + K, Ca, and Ti (Si = 6.54-6.63 and 6.55-6.78 pfu, (Na + K) = 0.53-0.62 and 0.61-0.80 pfu, Ca = 1.79-1.82 and 1.82-1.86 pfu, Ti = 0.19-0.21 and 0.16-0.23 pfu) than core (Si = 6.38-6.49 and 6.48-6.53 pfu, (Na + K) = 0.60-0.65 and 0.79-0.84 pfu, Ca = 1.81-1.88 and 1.82-1.86 pfu, Ti = 0.22-0.24 and 0.22-0.25 pfu).

3.3. Whole-rock geochemistry

Representative and fresh parts of the examined samples were selected for whole-rock geochemical analyses. The size of the samples was initially reduced in a jaw crusher, and then manually fine-powdered in an agate mortar. Major oxides were analyzed by 'lithium metaborate/tetraborate fusion ICP whole rock (Code 4B)', and minor and trace elements by 'trace element ICP/MS (Code 4B2)' techniques at Activation Laboratories of Ontario, Canada. The fused sample was diluted analyzed by Perkins Elmer Sciex ELAN 600, 6100 or 9000 ICP/MS. Three blanks and five controls (three before sample group and two after) are analyzed per group of samples. Duplicates are fused and analyzed every 15 samples. The instrument is recalibrated every 40 samples. Detection limits of major elements are 0.01%, whereas those of REE are 0.002-0.05 ppm. Detailed analytical conditions and detection limits shows in http://www.actlabs.com/.

3.3.1. Major and trace elements

The plots using major elements are applied for all examined samples. In addition, this study applied discrimination diagrams using trace elements for samples from Tenmondai Rock to discuss the tectonic setting of protoliths, which has not been reported in detail from this region yet (Figs. 9, 10, 11, 12).

The relationship between total alkali and SiO_2 (TAS) content can be utilized to classify igneous protolith (Fig. 9a). According to TAS plots, most of the metabasite samples (Ts11021001A, Ts11021003A, Ts11021007H, and Ts11021106A) are plotted in the field of sub-alkalic gabbro, whereas some metabasites (Ts11021006B and Ts11011002A) are alkalic. Nb/Y versus Zr/TiO_2 diagrams (Winchester and Floyd, 1977) indicate sub-alkalic signature of the samples from Tenmondai Rock, although they are plotted in the range of sub-alkaline basaltic (Ts11021001A and Ts11021006B), andesitic (Ts11021106A), and overlapping area between the fields of andesite and basalt (Ts11021003A and Ts11021007H) (Fig. 9b).

In the Harker diagram (Fig. 10, after Wilson, 1989), amphibolites show slightly higher SiO_2 content of 48.5-48.6 wt. % than that of mafic granulites (44.7-48.4 wt. %). Garnet-bearing mafic granulite (Ts11021106A), however, shows the highest SiO_2 content in the examined samples as 50.1 wt. % (Fig. 10).

In the primitive-mantle normalized trace element plot (Sun and McDonough, 1989), most of the metabasites are characterized by enrichment of large ion lithophile elements (LILEs) such as Rb, Ba, and K, though one sample (Ts11021001A) show negative anomaly of Rb. In addition, these samples indicate negative Nb and Ti anomalies which are common in arc-related magmas (Fig. 11a).

In the chondrite-normalized REE plot (McDonough and Sun, 1995), the metabasites are characterized by enrichment of light REE (LREE) and smooth heavy REE (HREE) patterns, suggesting crystallization differentiation. Most of them show no obvious Eu anomaly, however, two samples (Ts11021006B and Ts11021007H) indicate slightly positive Eu anomalies, possibly related to plagioclase accumulation and/or crustal contamination (Fig. 11b).

3.3.2. Petrogenetic implication

Plots of some samples are fallen in different fields in the different triangular diagrams (Figs. 12b, c, d). Although samples Ts11021001A and Ts11021003A are plotted in the field of island arc basalts in all triangular diagrams (Figs. 12b, c, d), sample Ts11021006B shows the features of oceanic-island alkali basalt (OIA) in TiO_2-MnO-P_2O_5 triangular diagram, E-type MORB (field 'B' in the figure) in Nb-Zr-Y triangular diagram (field 'B' in the figure), and calc-alkali basalt in Y-La-Nb triangular diagram (field '1A' in the figure). In addition, both samples Ts11021007H and Ts11021106A are fallen in the field '1B' (overlapping field of '1A [calc-alkali basalts]' and '1C [volcanic-arc tholeiites]') in Y-L-Nb diagram, however, they are plotted in MORB and OIA in TiO_2-MnO-P_2O_5 diagram, and fields 'D' (N-type MORB and volcanic-arc basalts) and 'C' (within-plate tholeiites and volcanic-arc basalts) in Nb-Zr-Y diagram, respectively. On the other hand, Th/Yb versus Nb/Yb binary plot (Fig. 12a, after Pearce, 2008) shows that these metabasites are plotted away from non-arc mantle array, suggesting subduction-zone flux or input of crustal component (Fig. 12a).

Chapter 4. Metamorphic pressure and temperature condition

4.1. Geothermobarometry

Several geothermobarometers were applied to garnet-bearing mafic granulites (Ts11021106A from Tenmondai Rock and Ts11011002A from Sudare Rock) to obtain peak metamorphic conditions of the study areas. The garnet-orthopyroxene geothermometer might be a useful tool to determine the metamorphic temperature of the sample because the core of garnet and orthopyroxene can be considered to have been in equilibrium during high-grade metamorphism. The estimated temperature range of the Tenmondai Rock sample is 792-826°C at 8 kbar based on the method of Aranovich and Berman (1997). The metamorphic pressure for the sample was calculated using the garnet-orthopyroxene-plagioclase-quartz geobarometer of Moecher et al. (1988) as 8.4-9.3 kbar at 800°C. On the other hand, the pressure calculated based on the method of Perkins and Newton (1981) is 6.5-7.5 kbar at 800°C, which is lower than the result of Moecher et al. (1988). This study regards the maximum pressure obtained by the calculation using the method of Moecher et al. (1988) and the minimum pressure obtained by the method of Perkins and Newton (1981) as upper and lower limits of estimated metamorphic pressure of the studied sample, respectively. Slightly higher *P-T* ranges are obtained from a granulite (sample Ts11011002A) from Sudare Rock as 860-891°C at 8 kbar based on the garnet-clinopyroxene geothermometer of Ellis and Green (1979), and 8.0-8.4 kbar and 8.5-9.2 kbar at 800°C based on the garnet-clinopyroxene-plagioclase-quartz geobarometers of Perkins and Newton (1981) and Moecher et al. (1988), respectively. These results are summarized in Table 10 and Fig. 13.

4.2. Mineral equilibrium modeling

The stability of mineral assemblages in a mafic granulite examined in this study was constrained using THERMOCALC 3.45 (Powell and Holland, 1988; Holland and Powell, 1998, 2011; data set tc-ds62, a file created February 2012). The pseudosection calculations were undertaken in the system Na_2O–CaO–K_2O–FeO–MgO–Al_2O_3–SiO_2–H_2O–TiO_2–Fe_2O_3 (NCKFMASHTO), because it is probably the most suitable approximation to model the metabasite. The phases considered in the modeling are tonalitic melt, clinoamphibole, augite, and sodic–calcic clinopyroxene (Green et al., 2016), orthopyroxene, garnet, and biotite (White et al., 2014), olivine and epidote (Holland and Powell, 2011), feldspars (Holland and Powell, 2003), spinel-magnetite (White et al., 2002), and ilmenite-hematite (White et al., 2000). Quartz, rutile, and H_2O are treated as pure phases.

The technique has been applied to sample Ts11021106A. Bulk rock compositions were determined by FUS-ICP-MS at Activation Laboratories, Ontario, Canada. The chemical composition (in wt. %) of the sample is $SiO_2 = 50.06$, $Al_2O_3 = 17.31$, FeO = 12.56, MnO = 0.209, MgO = 4.91, CaO = 7.40, $Na_2O = 0.97$, $K_2O = 1.68$, and $TiO_2 = 2.48$. All iron in this sample was recalculated as FeO. MnO is neglected in the modeling because the MnO content in the sample is very low (less than 1%). As P_2O_5 is neglected from the system, the CaO equivalent to apatite should be extracted from the calculation. The corrected CaO content of 6.52 wt. % was adopted for the pseudosection calculation. The temperature-molar H_2O contents (T-M[H_2O]) diagram was constructed to determine the H_2O content during high-grade metamorphism (Fig. 14). The T-M(H_2O) diagram of the sample was calculated at $P = 8$ kbar based on the results of geobarometry (Table 10 and Fig. 13), and shows the stability field of the peak mineral assemblage (Grt + Opx + Pl + Ilm + Qtz + melt ± Kfs) at M(H_2O) < 2.5 mol %. Modal isopleth for inferred melt phase was applied to constrain M(H_2O). In the thin section, evidence of melting event (such as the presence of melt inclusion, leucosome, and melt-consumed reaction texture) is limited, possibly suggesting that the modal abundance of melt phase during high-grade metamorphism was low in this sample. In this study, the mode of melt phase was assumed as <5.0 mol %, therefore maximum M(H_2O) has been regarded as 0.5 mol % (Fig. 14).

Figure 15 is a calculated *P-T* pseudosection for sample Ts11021106A which has been used to contain peak mineral assemblage of garnet + orthopyroxene + plagioclase + ilmenite + quartz ± K-feldspar ± inferred melt. The stability field plotted in the pseudosection indicates a wide *P-T* range of >750°C and >3.5 kbar to ~950°C and 10.5 kbar. The upper-pressure stability limit is constrained by orthopyroxene-out line, whereas the lower limit by garnet-out line. The peak *P-T* condition was further constrained using the grossular content [X_{grs} = Ca/(Fe + Mg + Ca)] isopleths for garnet and modal isopleths for melt, as about 850-900°C and about 7.5-8.5 kbar. Retrograde reaction textures such as symplectite of orthopyroxene + plagioclase ± ilmenite ± biotite around garnet (reaction [1]) suggest near-isothermal decompression after the peak metamorphic stage toward garnet-absent and biotite-present fields. The rock, therefore, experienced near-isothermal decompression along a clockwise *P-T* path from the peak *P-T* condition to the stability field of orthopyroxene + plagioclase + ilmenite + biotite + quartz ± K-feldspar during retrograde metamorphism.

Chapter 5. Zircon U-Pb geochronology and REE geochemistry

5.1. Analytical method for zircon U-Pb geochronology and REE geochemistry

Zircon U-Pb dating was performed by laser ablation-inductive coupled plasma-mass spectrometry (LA-ICP-MS). Detailed procedures for zircon separation and U-Pb analyses are summarized in Tsutsumi et al. (2012). Zircon grains were separated by heavy liquid (diiodo-methane) and magnetic separation from crushed rock samples, and then purified by handpicking under a binocular microscope. Zircon grains from the studied samples and standard materials were mounted in epoxy resin disc and polished until the surface was flattened with the center of the grains exposed. The FC1 zircon (^{206}Pb/^{238}U=0.1859; Paces and Miller, 1993) and NIST SRM 610 standard glass were used as standard materials. Back-scattered electron and cathodoluminescence (CL) images were obtained using scanning electron microprobe - cathodoluminescence (SEM-CL) equipment, JSM-6610 (JEOL) and a CL detector (SANYU electron), installed at National Museum of Nature and Science, Japan. U-Th-Pb isotopic analyses were carried out using LA-ICP-MS (Agilent 7700x with ESI NWR213 laser ablation system) installed at the National Museum of Nature and Science, Japan. A Nd-YAG laser with a 213 nm wavelength and 5 ns pulse was used for the analysis. A 25-micron spot size and 4–5 J/cm^2 laser power was adopted in this study. He gas was used as the carrier gas instead of Ar gas to enhance a higher transport efficiency of ablated materials (e.g., Eggins et al., 1998). Common Pb corrections for the concordia diagrams and for each age were made using ^{208}Pb (Williams, 1998), on the basis of the model for common Pb compositions proposed by Stacey and Kramers (1975). The upper and lower intercepts in the concordia diagram were calculated using the Isoplot4.15/Ex software (Ludwig, 2008).

REE contents in zircon were analyzed using the same instrument (LA - ICP - MS Agilent 7700x with ESI NWR213 laser ablation system) installed at the National Museum of Nature and Science, Japan. An Ar-F excimer laser with a 213 - nm wavelength and 5 - ns pulse were used for the analysis. The REE analyses have been done on spots adjacent to those of U-Th-Pb isotopic analyses. 25-µm spot size was adopted in this study. A NIST SRM610 glass was used as a standard. Stoichiometric major elements are generally used for calibration of trace elements in each phase. In this study, stoichiometric Si was used as the internal standardization element. All REE values were normalized by C1 chondrite values in McDonough and Sun (1995).

5.2. Results

The results of zircon U-Pb analyses of the metabasite samples are given in Tables 11 and 12. CL images of representative zircons are shown in Figures 16 and 17 together with analyzed spots and their spot numbers. The Tera-Wasserburg (T-W) concordia diagrams and probability density plots with histograms of ages are shown in Figures 18a, b, c, and d. In the following text and figures, ages older or younger than 1300 Ma are discussed based on $^{207}Pb/^{206}Pb$ or $^{206}Pb/^{238}U$ ages, respectively. The error levels are 1-sigma.

5.2.1. Tenmondai Rock (Ts11021106A)

Zircon grains from sample Ts11021106A are translucent and colorless or light brownish and show subidioblastic and rounded in habit. The grains show ellipsoidal to elongate features with a size range of 50-200 µm and an aspect ratio of 4:1 to 1:1. In CL images, most of the grains show oscillatory-zoned, irregular concentric-zoned, or structureless cores mantled by structureless rim (Fig. 16). Cores of some grains have been metamictized. Most of the rims can be subdivided into inner and outer rims. 70 spots were analyzed from 63 zircon grains in the sample (Table 11). Most of the analyzed spots are discordant suggesting significant lead loss (Fig. 18a, Table 11), with 28 spots showing <10% discordance. The results show that ages with <10% discordance vary from 809±9 Ma to 481±6 Ma ($^{206}Pb/^{238}U$ age) (Figs. 18a, b). Their Th and U contents and Th/U ratio show wide ranges of 1-918 ppm, 74-1118 ppm, and 0.01-0.84, respectively (Table 11). Analyzed spots with low discordance (<10%) can be obviously subdivided into two groups based on age and Th/U ratio; older (808±9 to 614±8 Ma) and high-Th/U ratio (0.07-0.84) group, and younger (582±12 to 481±6 Ma) and low-Th/U ratio (0.01-0.04) group. All zircon core data are classified as the older group with a weighted mean age of 743±27 Ma (MSWD = 13), suggesting Neoproterozoic magmatism (e.g., Williams and Claesson, 1987; Kinny et al., 1990; Maas et al., 1992). A few inner and outer rims also show high Th/U ratio (>0.1) and older (>600 Ma) ages (inner rim: spot 61 [764±9 Ma], spot 116 [785±9 Ma]/ outer rim: spot 22 [614±8 Ma], spot 106 [627±11 Ma]). On the other hand, most rims can be classified as the younger group, suggesting their overgrowth during Neoproterozoic (weighted mean age = 529±15 Ma; MSWD = 15) high-grade metamorphism.

REE analyses for metamorphic rims have been performed and 10 spots have been analyzed. The chondrite-normalized REE patterns (using data of McDonough and Sun, 1995) are shown in Figure 19a. In this figure, the angle of M-HREE slopes varies from positive steep to flat or negative with Lu_N/Gd_N values as 0.64-66.2. The plot of Lu_N/Gd_N versus U-Pb ages shows that Lu_N/Gd_N tends to increase as the U-Pb ages become younger, and three spots younger than ca. 520 Ma show particularly high Lu_N/Gd_N values (>10) (Fig. 20a). In addition, although most of the spots show almost no Eu anomaly, and their Eu/Eu* ($Eu^*=[Sm_N \times Gd_N]$^[1/2]) values are around 1.0, two spots with ages younger than 520 Ma (518±7 and 513±7 Ma) and high Lu_N/Gd_N values show negative Eu anomaly (Fig. 20b). These results may suggest that major change of metamorphic conditions and the mineral equilibrium could have occurred at ca 520 Ma.

5.2.2. Sudare Rock (Ts11011002A)

Zircon grains from sample Ts11011002A are translucent and colorless or light brownish, and are subidioblastic to xenoblastic and rounded in habit. The grains show rounded to ellipsoidal features with a size range of 50-100 µm and an aspect ratio of 2:1 to 1:1. In CL images, most of the grains are very dark and homogeneous without bright part, although some grains have structureless or concentric-zoned bright core (Fig. 17). 134 spots were analyzed from 119 grains in the sample (Table 12). Most of the analyzed spots are discordant suggesting significant lead loss (Fig. 18c, Table 12), with 69 spots showing <10% discordance. These concordant ages vary from 783±32 Ma to 514±6 Ma ($^{206}Pb/^{238}U$ age) (Figs. 18c, d). Their Th and U contents and Th/U ratio show wide ranges of 6-186 ppm, 22-1808 ppm, and 0.005-0.29, respectively (Table 12). Three bright cores (spot 60, 95 and 106) show middle Neoproterozoic ages (783±32 Ma to 690±21 Ma) with large error and low U and Th contents (22-52 ppm and 6-10 ppm, respectively) (Figs. 17, 18c, Table 12). Their Th/U ratios higher than 0.1 might suggest their magmatic origin. Thus, the bright CL cores of zircon grains could be the traces of middle Neoproterozoic magmatism. Other dark CL and structureless grains show younger late Neoproterozoic ages (630±7 Ma to 514±6 Ma) with lower errors. Their U and Th contents (331-1808 ppm and 8-186 ppm, respectively) are higher than those of cores (22-52 ppm and 6-10 ppm, respectively) (Figs. 17, 18c, Table 12). These grains are considered to be late Neoproterozoic metamorphic overgrowth because of their structureless CL features and their distributions around the lower-intercept of the discordia in the T-W concordia diagram (Fig. 18d). On the other hand, most of their Th/U ratios range from 0.08 to 0.17, mostly higher than 0.1 (Table 12).

The geochemical REE analyses for zircon grains, mainly for metamorphic zircons, have been performed and 44 spots have been analyzed. The normalized REE patterns are shown in Figure 19b. This figure shows that the angle of M-HREE slopes varies from positive steep to flat with Lu_N/Gd_N values as 3.35-58.3. In addition, Eu shows slightly positive and negative anomalies with Eu/Eu* value as 0.35-2.27 (Fig. 19b). The plot of Lu_N/Gd_N versus U-Pb ages indicate that the HREE patterns of zircons change drastically at ca. 560 Ma; the Lu_N/Gd_N values are nearly constant about 10 from ca. 630 Ma to 560 Ma, however, the values scatter as 4.41-58.3 from ca. 560 Ma to 510 Ma (Fig. 20a). On the other hand, the diagram of Eu/Eu* values versus U-Pb ages shows no trend depending on U-Pb ages (Fig. 20b). These results suggest that metamorphic mineral equilibrium, particularly the contribution minerals which dominantly controls HREE behavior, might change drastically at ca. 560 Ma.

Chapter 6. Discussion

6.1. Petrology and geochemistry of metabasites from Tenmondai Rock

The geochemical data of the mafic rocks indicate features and process of formation of protolith magma. The Nb/Y versus Zr/TiO_2 diagram indicates their protoliths as sub-alkaline basalt to andesite. The negative Nb and Ti anomalies in Figure 11a support their subduction-related volcanic arc origin. Th/Yb versus Nb/Yb diagram indicates that the protolith of the samples has been affected by subduction zone flux or crustal contamination (Fig. 9a). On the other hand, the triangular diagrams applied in this study indicate that the geochemical data of some samples are plotted in the fields of other tectonic settings, such as N- and E-type MORB, oceanic island tholeiites, oceanic island alkali basalts, and overlapped area of them (Figs. 12b-d). These results can be explained by contamination of oceanic crust and/or material of oceanic island subducted or incorporated in the accretionary complex. This argument, however, is not consistent with the results of a previous study suggesting that the northeastern LHC might have been 'juvenile' volcanic arc, based on Lu/Hf isotopic data of zircons in orthogneisses from the northern part of the LHC (Tsunogae et al., 2015). In this study, the protolith of examined metabasites from Tenmondai Rock is interpreted as volcanic arc basaltic rocks because of the result of Nb/Y versus Zr/TiO_2 diagram and the data of some samples (Ts11021001A and Ts11021003A) indicating volcanic-arc affinity in the triangular diagrams (Figs. 12a-d).

Previous studies suggest that the LHC is the collage of Neoarchean (ca. 2.5 Ga) microcontinent, Paleoproterozoic arc magmatic suites (ca. 1.8 Ga), and Neoproterozoic (ca. 1.0 Ga) juvenile volcanic arc. It was formed through multiple collisions between these crustal blocks during late Neoproterozoic-Cambrian Gondwana assembly (e.g., Tsunogae et al., 2015, 2016; Kazami et al., 2016; Takahashi et al., 2018; Takamura et al., 2018). Geochemical and geochronological data reported in this study indicate that the protolith of metabasites from Tenmondai Rock was part of Neoproterozoic volcanic arc, particularly a part of 'northern LH-Vijayan Complex' of Takahashi et al. (2018). In addition, the protolith of sample Ts11011002A from Sudare Rock could be a crustal fragment of Neoproterozoic volcanic arc materials incorporated in the suture zone.

6.2. *P-T* conditions

Applications of mineral equilibrium modeling in the system NCKFMASHTO to the peak mineral assemblage of mafic granulite (Ts11021106A; Grt + Opx + Pl + Ilm + Qtz + melt ± Kfs) yielded the peak *P-T* conditions of 850-900°C and ca. 7.5-8.5 kbar, suggesting granulite-facies high-grade metamorphism (Fig. 15). This temperature is slightly higher than the results of garnet-orthopyroxene geothermometry (792-826°C at 8 kbar; Table 10 and Fig. 13). This might have been caused by elemental diffusion between garnet and orthopyroxene during high-temperature metamorphism. The mineral assemblage (Grt + Pl + Qtz + Ap + Rt ± melt) occurring as inclusions in garnet can be interpreted as the prograde mineral assemblage, however, the stability field of them is not found in the *P-T* pseudosection. One possibility of this might be due to the change of rock composition by melt extraction. Some kyanite-bearing pelitic gneisses and leucocratic rocks have been reported, suggesting that the rocks experienced kyanite-stable *P-T* condition during prograde metamorphism (e.g., Hiroi et al. 1983b). The samples examined in this study, however, show less evidence to constrain the prograde *P-T* condition. The existence of orthopyroxene + plagioclase ± biotite ± Fe-Ti oxides symplectite suggests the rock experienced near-isothermal decompression during retrograde metamorphism toward the stability *P-T* field of retrograde orthopyroxene + plagioclace + ilmenite + biotite + quartz ± K-feldspar mineral assemblage along the clockwise *P-T* path (Figs. 15, 22).

Hiroi et al. (1983a) reported metamorphic *P-T* condition of Tenmondai Rock as 7.2-7.5 kbar at 750°C based on geothermobarometry. This means that the results of this study show higher peak metamorphic conditions than those proposed in the previous study. In recent studies, granulite-facies high-temperature condition (>800~920°C: Nakamura et al., 2013; Iwamura et al., 2013) have been also proposed from Akarui Point, an exposure located on the 'transitional zone' of the LHC. This might suggest that metamorphic grade of 'transitional zone' between amphibolite- to granulite-facies in the Prince Olav Coast could be higher than the results of the previous model (e.g., Hiroi et al., 1991).

Applications of garnet-clinopyroxene geothermometry (Ellis and Green, 1979) and garnet-clinopyroxene-plagioclase-quartz geobarometry (Perkins and Newton, 1981; Moecher et al., 1988) to sample Ts11011002A have yielded the peak metamorphic *P-T* condition of Sudare Rock as 8-10 kbar and 850-900 °C (Fig. 13). Thus, the metabasite from Sudare Rock might have experienced granulite-facies high-grade metamorphism. The temperature obtained in this study is higher than the result of garnet-hornblende geothermometry (740-760 °C at 7 kbar) performed by Tsunogae et al. (2015). In addition, the existence of symplectite, formed by consumption of garnet in reaction (2), suggests near-isothermal decompression after peak metamorphism along a clockwise *P-T* path (Fig. 22).

Previous studies reported ultrahigh-temperature metamorphism (UHT; >1000°C) from some exposures in the southwestern LHC such as Rundvågshetta, Skallevikshalsen, and Skallen, adjacent exposures of Sudare Rock (Osanai et al., 2004; Yoshimura et al., 2008; Kawasaki et al., 2011). On the other hand, Tsunogae et al. (2014) inferred that these UHT metamorphisms were only local phenomena, and peak

P-T conditions of adjacent orthogneisses in Rundvågshetta and adjacent Vesleknausen as 800-850°C. Similar peak *P-T* conditions have been also reported from the southwestern LHC, for example, Austhovde (800-850°C and 8-9 kbar; Takahashi and Tsunogae, 2017) and Skallevikshalsen (770-960°C and 6-12 kbar; Yoshimura et al., 2004), and are consistent with the result from Sudare Rock in this study.

Recent studies including this study reported similar granulite-facies peak metamorphic *P-T* conditions as 800-900°C and 7-10 kbar from wide range of the LHC, including Prince Olav Coast (e.g., Yoshimura et al., 2004; Satish-Kumar et al., 2006; Nakamura et al., 2013; Tsunogae et al., 2014, 2016; Takahashi and Tsunogae, 2017). Previous studies inferred transition of metamorphic grade from amphibolite facies in Prince Olav Coast to granulite facies Lützow-Holm Bay area (e.g., Hiroi et al., 1991). The results of recent studies, however, suggest that the thermal gradient of the LHC might be smaller than the previous model. In addition, most of the *P-T-t* paths of the LHC obtained in previous studies are characterized by near-isothermal decompression along clockwise path (e.g., Fraser et al., 2000; Yoshimura et al., 2004, Kawakami and Hokada, 2010; Kawasaki et al., 2011; Iwamura et al., 2013; Takahashi and Tsunogae, 2017). It seems to suggest that the process of decompression and cooling caused by crustal exhumation could be similar through the LHC. However, Baba et al. (2019) reported garnet corona of late metamorphic stage around kyanite in pelitic rock from Tenmondai Rock and proposed near-isobaric cooling after granulite-facies peak metamorphism based on geothermobarometry using garnet corona, adjacent biotite and plagioclase (750-800°C and 8-9 kbar). The *P-T* path inferred by them is significantly different from those of other studies including this study suggesting near-isothermal decompression. These differences might suggest more than two stages of *P-T* path and near-isothermal decompression path and near-isobaric cooling path could reflect different stages. Further detail petrological and geochronological investigation is required to reveal the *P-T-t* evolution through the LHC.

6.3. Zircon U-Pb geochronology

The morphology, core-rim texture from CL images, and high Th/U ratio of zircon cores in sample Ts11021106A from Tenmondai Rock suggest that the older cores of zircon indicate the age of magmatic crystallization. The $^{206}Pb/^{238}U$ age of zircon cores varies from 808 Ma to 698 Ma with weighted mean age as 743±27 Ma, which might indicate middle Neoproterozoic emplacement of protolith magma (Figs. 16, 18a, b, Table 11). High MSWD value, however, is possibly suggesting contamination of xenocryst of zircon or scattering by Pb-loss during high-grade metamorphism.

As mentioned above, geochemical data of garnet-bearing mafic granulite in this study indicate that the protolith of this rock is volcanic arc affinity. Thus, the protolith of the mafic rocks in Tenmondai Rock was formed by middle Neoproterozoic volcanic arc magmatism. Such a Neoproterozoic magmatic event has also been reported from the Prince Olav Coast by previous studies. For example, Tsunogae t al. (2015) proposed early Neoproterozoic (ca. 1.0 Ga) juvenile volcanic arc magmatism in the northeastern LHC, based on geochemical, zircon U-Pb geochronological, and zircon Lu-Hf isotopic data. Kazami et al. (2016) obtained geochemical and zircon geochronological data from Akarui Point, suggesting volcanic arc magmatism during early to middle Neoproterozoic. Some recent studies have proposed that the LHC is a collage of Neoarchean (ca. 2.5 Ga) microcontinent defined as 'Shirase microcontinent', early Neoproterozoic volcanic arc, and suture zone between them including fragments of Paleoproterozoic (ca. 1.8 Ga) and minor Neoarchean and Neoproterozoic arc-magmatic materials (e.g., Tsunogae et al., 2015, 2016; Takahashi et al., 2018; Takamura et al., 2018). The data suggesting Neoproterozoic arc magmatism at Tenmondai Rock inferred in this study is comparable with previous results. Therefore, protoliths of the metabasites from Tenmondai Rock can be regarded as a part of the middle Neoproterozoic volcanic arc.

Only a few magmatic cores of zircon could be analyzed from sample Ts11011002A (Figs. 17, 18c, d, Table 12). The age of these cores varies from 783±32 Ma to 690±21 Ma which suggests middle Neoproterozoic magmatism. In contrast, previous studies reported the protolith ages of charnockite in Sudare Rock as Neoarchean (ca. 2.5 Ga: Dunkley et al., 2014; Tsunogae et al., 2016). Takahashi et al. (2018) inferred that fragments of Neoproterozoic volcanic arc could be distributed in the suture zone at the central LHC. Thus, Sudare Rock might be also one of the fragments of volcanic arc materials integrated during the final collisional event. Another possibility is that these cores were originally older and affected by middle Neoproterozoic magmatism.

The structureless zircon rims with low Th/U ratios from sample Ts11021106A can be regarded as metamorphic zircon which overgrew around magmatic cores during high-grade metamorphism of Tenmondai Rock (Figs. 16, 18a, b). The ages of metamorphic zircon rims with <10% discordance show late Neoproterozoic to Cambrian ages (582±12-481±6 Ma). Their weighted mean age is 529±15 Ma with high MSWD (= 15) possibly suggesting multiple overgrowths. In addition, the outer rim of two older zircons (614±8 and 627±11 Ma) with high Th/U ratio suggest earlier metamorphic events under the absence of Th-rich minerals such as monazite.

The dark CL and structureless zircon grains in Ts11011002A from Sudare Rock are interpreted as metamorphic overgrowth. The age of metamorphic zircons with <10% discordance varies from 630±7 Ma to 514±6 Ma and their weighted mean age is 548 ±6 Ma with high MSWD (= 17) (Figs. 17, 18c, d). These ages suggest similar late Neoproterozoic to Cambrian multiple overgrowths with the results of Tenmondai Rock in this study.

6.4. Zircon REE geochemistry

The REE analyses were mainly carried out for rims and/or structureless parts of zircon showing low Th/U ratios. Particularly, normalized HREE patterns and Eu anomaly have been focused in this study because they can be used as indicators of the modal volume of garnet and feldspar in the sample (e.g., Rubatto, 2002, 2017; Rubatto et al., 2013).

Figure 20a shows Lu_N/Gd_N values versus U-Pb age of zircon in the examined samples, meaning enrichment or depletion of HREE in zircon. The data of sample Ts11021106A indicate that three spots younger than ca. 520 Ma show particularly high Lu_N/Gd_N values (>10). On the other hand, the data of sample Ts11011002A indicate that Lu_N/Gd_N values of zircons younger than ca. 560 Ma are scattered as 4.41-58.3 from about 10 (Fig. 20a). The increased HREE content in zircons can be explained by the breakdown of garnet and the liberation of HREE (e.g., Imayama et al., 2012; Rubatto et al., 2013). Thus, the age of garnet consumption might be different between the two areas; ca. 520-510 Ma at Tenmondai Rock, and ca. 560-550 Ma at Sudare Rock, respectively. In addition, the Eu/Eu* ($Eu^*=[Sm_N \times Gd_N]^\wedge[1/2]$) values of zircons in Ts11021106A, representing the degree of Eu anomaly, decrease from about 1 to 0.2 at the ages younger than ca. 520 Ma (Fig. 20b). These might suggest the modal abundance of feldspar increased from ca. 520 Ma because the negative Eu anomaly can be made by coexisting of zircons with feldspar, an effective host mineral of Eu (e.g., Rubatto et al., 2002). The Eu/Eu* values of zircons in sample Ts11011002A, however, show no trend depending on U-Pb ages (Fig. 20b).

This synchronous consumption of garnet and abundance of feldspar observed for zircons in the sample from Tenmondai Rock (Ts11021106A) based on REE versus U-Pb ages of zircon could be fulfilled by formation of symplectite during near-isothermal decompression (Fig. 6b, 21). If zircon grew during the breakdown of garnet, released HREE might be trapped in growing zircons. In addition, the synchronous formation of symplectitic plagioclase and its consumption of Eu would form zircon rims with negative Eu anomaly (Fig. 21). As the symplectite formation has been correlated to the timing of near-isothermal decompression caused by rapid crustal exhumation, the results of this study might indicate that the exhumation of Tenmondai Rock could have occurred at ca. 520-510 Ma.

Change of Lu_N/Gd_N values in the sample from Sudare Rock (Ts11011002A) could have been caused by a similar symplectite-forming reaction during near-isothermal decompression (Figs. 7a, d, e-i, 21). Therefore, the exhumation of Sudare Rock at ca. 560-550 Ma could be earlier than Tenmondai Rock. However, no obvious negative Eu anomaly of zircon, caused by increasing plagioclase associated with symplectite formation, was detected from this sample. One possibility to explain this is that the modal abundance of plagioclase might be limited because of the low modal abundance of quartz, therefore the consumption of garnet and quartz by the progress of reaction (2) stopped soon during isothermal decompression. Other factors such as heterogeneity of REE in the rocks can be also considered as a reason.

6.5. Tectonic implications

6.5.1. Timing of exhumation

Although similar near-isothermal decompression paths caused by rapid exhumation have been proposed throughout the LHC (Fraser et al., 2000; Yoshimura et al., 2008; Kawasaki et al., 2011; Takahashi and Tsunogae, 2017), the evaluation of REE geochemistry of zircons with U-Pb ages suggests the different timing of exhumation. Tenmondai Rock stayed under garnet-bearing *P-T* conditions for at least 60 m. y. from ca. 580 Ma to ca. 520 Ma, and exhumed at ca. 520-510 Ma. Sudare Rock could have been exhumed earlier at ca. 560-550 Ma (Figs. 20a, b, 21). These results may suggest that the timings of post-peak exhumation were different depending on regions (Fig. 23).

Fraser et al. (2000) analyzed zircon U-Pb ages and K/Ar and ^{40}Ar/^{39}Ar ages of hornblende and biotite in leucosome occuring in the neck of metabasite boudin from Rundvågshetta. They calculated thermal models and suggested near-isothermal decompression at granulite-facies high-grade metamorphism from ca. 520 Ma to ca. 513 Ma, which is similar age range with the timig of exhumation of Temondai Rock.

6.5.2. Comparison with other Gondwana fragments

The *P-T-t* path with geochronological restriction can also be a key to compare different metamorphic terranes. The LHC has particularly been correlated with Sri Lankan terranes such as the Highland Complex based on petrological, geochemical and geochronological similarities (e.g., Yoshida et al., 1992; Shiraishi et al., 1994; Takamura et al., 2015, 2018, Kazami et al., 2016; Takahashi et al., 2018). This study compared the REE geochemistry with U-Pb geochronological data from the LHC with those from the Highland Complex.

Figures 20a and b show Lu_N/Gd_N and Eu/Eu* values of metamorphic zircons with their U-Pb ages in garnet-bearing charnockite (sample HC10) and metamorphosed mafic sill (sample HC11), respectively (Santosh et al., 2014). These two samples contain symplectitic texture composed of orthopyroxene and plagioclase suggesting the progress of reaction (2). The figures suggest that high Lu_N/Gd_N groups, particularly for sample HC10, occur at ca. 560-520 Ma (Fig. 20a), which possibly indicates the age of near-isothermal decompression caused by rapid exhumation. In contrast, the Eu/Eu* values do not show any obvious anomalies from 560 to 520 Ma (Fig. 20b). These REE geochemical and U-Pb geochronological features are similar to those of sample Ts11011002A from Sudare Rock (Figs. 20a, b). If the ages of ca. 560-520 Ma are interpreted as the age of near-isothermal decompression, the timing of exhumation was very similar between the central LHC and the Highland Complex, which can be new evidence on the similarity of the two regions. On the other hand, these ages are obviously older than the proposed decompression age of Sri Lanka by previous studies (e.g., Takamura et al., 2015; He et al., 2018). Particularly, He et al. (2018) inferred 'long-lived metamorphism' for longer than 100 m.y. (ca. 660-520 Ma) and they argued that decompression and associated accelerated cooling took place at ca. 480-470 Ma after high-grade metamorphism. The timing of exhumation might be different depending on localities such as Tenmondai Rock and Sudare Rock in this study. Thus, systematic investigations into various regions and lithologies are necessary to unravel the *P-T-t* evolution throughout the terrane.

6.5.3. Implications for the mechanism of exhumation on Gondwana collisional orogen

Several models explaining the mechanism of exhumation on collisional orogens have been proposed. For example, the 'channel flow model', a numerical model showing large ductile extrusion of high-temperature metamorphic rocks to focused erosional front, has been well discussed by many authors (e.g., Beaumont et al., 2001, 2004; Jamieson e al., 2004). Some predictions for the thermal and kinetic behavior of metamorphic rocks have been proposed and the channel flow model requires clockwise *P-T* path and/or isothermal decompression (e.g., Kohn, 2008, 2014). On the other hand, the ‘critical taper model’ (e.g., Henry et al., 1997; Bolinger et al., 2006) proposed deformation through thrusting without lower crustal flow, and predicted isobaric cooling and/or ‘hairpin’ P-T paths (e.g., Kohn, 2008, 2014). The P-T-t paths proposed by this and previous studies in the LHC are consistent with predicted P-T-t paths by channel flow model. In addition, Hiroi et al. (2014) reported ‘felsite inclusions’ with quench textures in garnet of the granulites from central Highland Complex, Sri Lanka, suggesting very fast cooling caused by rapid exhumation which has been considered to be caused by channel flow. Similar felsite inclusions were also reported from the LHC (e.g., Shiraishi et al., 2008; Kawakami et al., 2016; Hiroi et al., 2019). Although these features potentially suggest that channel flow corresponds to be the dominant mechanism of rapid exhumation observed in this study, unsolved problems still remain such as the discordant duration time of high-grade metamorphism between the model and obtained features. Thus, more systematic and wide applications of petrochronological analyses should be done, and they should be collaborated with structural and numerical studies to reveal the process of large metamorphic events.

Chapter 7. Conclusions

This study proposed the following conclusions from the above results;

(1) Geochemistry and zircon U-Pb geochronology of metabasites from Tenmondai Rock in the LHC indicate that the protoliths of them were middle Neoproterozoic (ca. 808 Ma to 698 Ma) arc magmatic rocks. These features are consistent with those of meta-igneous rocks from the northeastern LHC. Thus, the metabasites could be a part of the Neoproterozoic juvenile volcanic arc. The protolith of a metabasite from Sudare Rock could also be a fragment of the Neoproterozoic volcanic arc.

(2) Several geothermobarometers and mineral equilibrium modeling have been applied to two garnet-bearing mafic granulites from Tenmondai Rock and Sudare Rock. The results indicate granulite-facies peak metamorphic conditions and following subsequent near-isothermal decompression.

(3) This study evaluated REE contents of metamorphic zircons with their U-Pb ages. Lu_N/Gd_N and Eu/Eu* values of zircon from Tenmondai Rock sample increased and decreased at ca. 520 Ma, respectively. These features suggest near-isothermal decompression accompanied by the breakdown of garnet and formation of orthopyroxene + plagioclase symplectite caused by rapid exhumation. On the other hand, the sample from Sudare Rock only indicates increasing Lu_N/Gd_N values at ca. 560-550 Ma. These results suggest that the timing of the exhumation of northern LHC and the central LHC might have been different.

(4) Based on U-Pb and REE patterns of zircons from central Highland Complex, Sri

Lanka, and Sudare Rock, the exhumation of the two regions could have occurred at ca. 560 Ma to 520 Ma. The similarity of the timing of exhumation between the central LHC and the Highland Complex could be useful for further correlation of the regions.

(5) The *P-T-t* paths with near-isothermal decompression proposed in this and previous studies from Gondwana collisional orogens could be explained by the channel flow model.

Acknowledgments

I would like to express my gratitude to my supervisor, Prof. T. Tsunogae at the Faculty of Life and Environmental Sciences, the University of Tsukuba for his constant guidance, all sorts of facilitating, sharing his knowledge, critical reading and comments for improving this thesis. This work would never be accomplished without his gracious help. I am also thankful to Prof. Y. Arakawa, Dr. M. Kurosawa, and Dr. K. Ikehata at the University of Tsukuba and Dr. Y. Tsutsumi at the National Museum of Nature and Science for their helpful discussions and encouragements.

I am deeply indebted to Dr. Y. Tsutsumi at the National Museum of Nature and Science for his kind assistance and guidance of zircon analyses. All JARE-52 members are acknowledged for their geological fieldwork in Antarctica. I would like to thank all members of the metamorphic petrology laboratory for their support and help. Thanks are extended to all teachers, staff, and students at Earth Evolution Sciences, Graduate School of Life and Environmental Sciences, the University of Tsukuba for their advice and encouragement.

This study was supported by JSPS KAKENHI Grant Number JP18J10332.

References

Asami, M., Suzuki, K., Adachi, M., 1997. Th, U and Pb analytical data and CHIME dating of monazites from metamorphic rocks of the Rayner, Lützow-Holm, Yamato-Belgica and Sør Rondane Complexes, East Antarctica. Proc. NIPR Symp. Antarct. Geosci. 10, 130–152.

Aranovich, L.Y., Berman, R.G., 1997. A new garnet-orthopyroxene thermometer based on reversed Al2O3 solubility in FeO-Al2O3-SiO2 orthopyroxene. Amer. Mineral. 82 (3-4), 345–353.

Baba, S., Hokada, T., Kamei, A., Kitano, I., Motoyoshi, Y., Nantasin, P., Setiawan, N.I., Dashbaatar, D., 2019. New insights into the metamorphic evolution of the Lützow-Holm Complex along the Prince Plav Coast, East Antarctica. Abstract Volume, IAGR Conference series No. 25, pp. 1–2.

Beaumont, C., Jamieson, R.A., Nguyen, M.H., Lee, B., 2001. Himalayan tectonics explained by extrusion of a low-viscosity crustal channel coupled to focused surface denudation. Nature 414, 738–742.

Beaumont, C., Jamieson, R.A., Nguyen, M.H., Medvedev, S., 2004. Crustal channel flows: 1. Numerical models with applications to the tectonics of the Himalayan-Tibetan Orogen. J. Geophys. Res. 109, B06406.

Bollinger, L., Henry, P., Avouac, J.P., 2006. Mountain building in the Nepal Himalaya: Thermal and kinematic model. Earth Planet. Sci. Lett. 244, 58–71.

Buick, I.S., Clark, C., Rubatto, D., Hermann, J., Pandit, M., Hand, M., 2010. Constraints on the proterozoic evolution of the Aravalli-Delhi Orogenic belt (NW India) from monazite geochronology and mineral trace element geochemistry. Lithos 120, 511–528.

Cabanis, B., Lecolle, M., 1989. Le diagramme La/100-Y/15-Nb/8: un outil pour la discrimination des series volcaniques et la mise en evidence des processus demelange et/ou de contamination crustale. Comptes Rendus de l'Académie des Sciences Serie 2 (309), 2023–2029.

Collins, A.S., Pisarevsky, S.A., 2005. Amalgamating eastern Gondwana: the evolution of the Circum-Indian Orogens. Earth Sci. Rev. 71, 229–270.

Collins, A.S., Clark, C., Sajeev, K., Santosh, M., Kelsey, D.E., Hand, M., 2007a. Passage through India: the Mozambique Ocean suture, high pressure granulites and the Palghat-Cauvery Shear System. Terra Nova 19, 141–147.

Collins, A.S., Santosh, M., Braun, I., Clark, C., 2007b. Age and sedimentary provenance of the Southern Granulites, South India: U–Th–Pb SHRIMP secondary ion mass spectrometry. Precambrian Res. 155, 125–138.

Collins, A.S., Clark, C., Plavsa, D., 2014. Peninsular India in Gondwana: the tectonothermal evolution of the Southern Granulite Terrain and its Gondwanan counterparts. Gondwana Res. 25, 190–203.

Dharmapriya, P.L., Malaviarachchi, S.P.K., Kriegsman, L.M., Galli, A., Sajeev, K., Zhang, C., 2017. New constraints on the P-T path of HT/UHT metapelites from the Highland Complex of Sri Lanka. Geosci. Front. 8, 1405–1430.

Dunkley, D.J., 2007. Isotopic zonation in zircon as a recorder of progressive metamorphism. Goldschmidt Conference Abstracts, Geochimica et Cosmochimica Acta, vol. A224.

Dunkley, D.J., Shiraishi, K., Motoyoshi, Y., Tsunogae, T., Miyamoto, T., Hiroi, Y., Carson, C.J., 2014. Deconstructing the Lützow-Holm Complex with zircon geochronology. Abstract of 7th international SHRIMP workshop program, 116–121.

Eggins, S.M., Kinsley, L.P.J., Shelley, J.M.G., 1998. Deposition and element fractionation processes of occurring during atmospheric pressure sampling for analysis by ICP-MS. Appl. Surf. Sci. 129, 278–286.

Ellis, D.J., Green, D.D. 1979. An experimental study of the effect of Ca upon garnet-clinopyroxene Fe-Mg exchange equilibria. Contrib. Mineral. Petrol. 71, 13–22.

Ferry, J.M., Spear, F.S., 1981. Experimental calibration of the partitioning of Fe and Mg between biotite and garnet. Contrib. Mineral. Petrol. 66, 113–117.

Fraser, G., McDougall, L., Ellis, D.J., Williams, I.S., 2000. Timing and rate of Isothermal decompression in Pan-African granulites from Rundvågshetta, East Antarctica. J. Metamorph. Geol. 18, 441–454.

Goldman, D.S., Albee, A.L., 1977. Correlations of Mg/Fe partitioning between garnet and biotite with $^{18}O/^{16}O$ partitioning between quartz and magnetite. Am. J. Sci. 277, 413–420.

Green, E.C.R., White, R.W., Diener, J.F.A., Powell, R., Holland, T.J.B., Palin, R.M., 2016. Activity-composition relations for the calculation of partial melting equilibria in metabasic rocks. L. Metamorph. Geol. 34, 845–869.

Harley, S.L., 1989. The origin of granulites: a metamorphic perspective. Geol. Mag. 126, 215–247.

He, X.F., Hand, M., Santosh, M., Kelsey, D. E.,Morrissey, L. J., Tsunogae, T., 2018. Long - lived metamorphic P-T-t evolution of the Highland Complex, Sri Lanka: Insights from mafic granulites. Precambrian Res. 316, 227–243.

Henry, P., LePichon, X., Goffé, B., 1997. Kinematic, thermal and petrological model of the Himalayas: Constraints related to metamorphism within the underthrust Indian crust and topographic evolution. Tectonophysics 273, 31–56.

Hiroi, Y., Shiraishi, K., Nakai, Y., Kano, T., Yoshikura, S., 1983a. Geology and petrology of Prince Olav Coast, East Antarctica. In: Oliver, R.L., James, P.R., Jago, J.B. (Eds.), Antarctic Earth Science. Australian Academy of Science, Canberra, pp. 32–35.

Hiroi, Y., Shiraishi, K., Yanai, K., Kizaki, K., 1983b. ALUMINUM SILICATES IN THE

PRINCE OLAV AND SÔYA COAST, EAST ANTARCTICA. Mem. Natl. Inst. Polar Res. Spec. Issue 28, 115–131.

Hiroi, Y., Shiraishi, K., Motoyoshi, Y., 1991. Late Proterozoic paired metamorphic complexes in East Antarctica, with special reference to the tectonic significance of ultramafic rocks. In: Thomson, M.R.A., Crame, J.A., Thomson, J.W. (Eds.), Geological Evolution of Antarctica. Cambridge University Press, Cambridge, pp. 83–87.

Hiroi, Y., Yanagi, A., Kato, M., Kobayashi, T., Prame, B., Hokada, T., Satish–Kumar, M., Ishikawa, M., Adachi, T., Osanai, Y., Motoyoshi, Y., Shiraishi, K., 2014. Supercooled melt inclusions in lower–crustal granulites as a consequence of rapid exhumation by channel flow. Gondwana Res. 25, 226–234.

Hiroi. Y., Hokada, T., Kato, M., Yanagi, A., Adachi, T., Osanai, Y., Motoyoshi, Y., Shiraishi, K., 2019. Felsite-nanogranite inclusions and three Al_2SiO_5 polymorphs in the same garnet in ulyrahigh-temperature granulites from Rundvågshetta, Lützow-Holm Complex, East Antarctica. J. Mineral. Petrol. Sci. 114, 60–78.

Hokada, T., Motoyoshi, Y., 2006. Electron microprobe technique for U–Th–Pb and REE chemistry of monazite, and its implications for pre-, peak- and post-metamorphic events of the Lützow-Holm Complex and the Napier Complex, East Antarctica. Polar Geosci. 19, 118–151.

Holland, T.J.B., Powell, R., 1998. An enlarged and update internally consistent thermodynamic dataset with uncertainties and correlations: the system K2O–Na2O–CaO–MgO–MnO–FeO–Fe2O3–Al2O3–TiO2–SiO2–C–H2–O2. J. Metamorph. Geol. 8, 89–124.

Holland, T.J.B., Powell, R., 2003. Activity–composition relations for phases in petrological calculations: an asymmetric multicomponent formulation. Contrib. Mineral. Petrol. 145, 492–501.

Holland, T.J.B., Powell, R., 2011. An improved and extended internally consistent thermodynamic dataset for phases of petrological interest, involving a new equation of state for solids. J. Metamorph. Geol. 29, 333–383.

Imayama, T., Takeshita, T., Yi, K., Cho, D.L., Kitajima, K., Tsutsumi, Y., Kayama, M., Nishido, H., Okumura, T., Yagi, K., Itaya, T., Sano, Y., 2012. Two-stage partial melting and contrasting cooling history within the Higher Himalayan Crystalline Sequence in the fareastern Nepal Himalaya. Lithos 134, 1–22.

Iwamura, S., Tsunogae, T., Kato, M., Koizumi, T., Dunkley, D.J., 2013. Petrology and phase equilibrium modeling of spinel-sapphirine-bearing mafic granulite from Akarui Point, Lützow-Holm Complex, East Antarctica: Implications for the P-T path. J. Mineral. Petrol. Sci. 108, 345–350.

Jacobs, J., Thomas, R.J., 2004. Himalayan-type indenter-escape tectonics model for the southern part of the late Neoproterozoic-early Paleozoic East African-Antarctic orogeny. Geology 32, 721–724.

Jamieson, R.A., Beaumont, C., Nguyen, M.H., Lee, B., 2002. Interaction of metamorphism, deformation and exhumation in large convergent orogens. J. Metamorph. Geol. 20, 9–24.

Jamieson, R.A., Beaumont, C., Medvedev, S., Nguyen, M.H., 2004. Crustal channel flows: 2. Numerical models with implications for metamorphism in the Himalayan-Tibetan orogeny. J. Geophys. Res. 109, B0646.

Kadowaki, H., Tsunogae, T., He, X.F., Santosh, M., Takamura, Y., Shaji, E., Tsutsumi, Y., 2019. Pressure - temperature - time evolution of ultrahigh - temperature granulites from the Trivandrum Block, southern India: Implications for long - lived high - grade metamorphism. Geol. Jour. 2019, 1–19.

Kawakami, T., Hokada, T., 2010. Linking *P-T* path with development of discontinuous phosphorus zoning in garnet during high-temperature metamorphism – an example from the Lützow-Holm Complex, East Antarctica. J. Mineral. Petrol. Sci. 108, 345–350.

Kawakami, T., Grew, E.S., Motoyoshi, Y., Shearer, C.K., Ikeda, T., 2008. Kornerupine sensu stricto associated with mafic and ultramafic rocks in the Lützow-Holm Complex at Akarui Point, East Antarctica: what is the source of boron? Geol. Soc. Lond. Spec. Publ. 308, 351–375.

Kawakami, T., Hokada, T., Sakata, S., Hirata, T., 2016. Possible polymetamorphism and brine infiltration recorded in the garnet-sillimanite gneiss, Skallevikshalsen, Lützow-Holm Complex, East Antarctica. J. Mineral. Petrol. Sci. 111, 129–143.

Kawano, Y., Nishi, N., Kagami, H., 2006. Rb-Sr and Sm-Nd mineral isochron ages of a pegmatitic gneiss from Oku-iwa Rock, Lützow-Holm Complex, East Antarctica. Polar Geosci. 19, 109–117.

Kawasaki, T., Nakano, N., Osanai, Y., 2011. Osumilite and a spinel + quartz associationin garnet-sillimanite gneiss from Rundvågshetta, Lützow-Holm Complex, East Antarctica. Gondwana Res. 19, 430–445.

Kazami, S., Tsunogae, T., Santosh, M., Tsutsumi, Y., Takamura, Y., 2016. Petrology, geochemistry and zircon U–Pb geochronology of a layered igneous complex from Akarui Point in the Lützow-Holm Complex, East Antarctica: implications for Antarctica-Sri Lanka correlation. J. Asian Earth Sci. 130, 206–222.

Kinny, P.D., Wijbrans, J.R., Froude, D.O., Williams, I.S., Compston, W., 1990. Age constraints on the geological evolution of the Narryer Gneiss Complex, Western Australia. Aust. J. Earth Sci. 37, 51–69.

Kitano, I., Osanai, Y., Nakano, N., Adachi, T., Fitzsimons, I.C.W., 2018. Detrital zircon and igneous protolith ages of high-grade metamorphic rocks in the Highland and Wanni Complexes, Sri Lanka: Their geochronological correlation with southern India and East Antarctica. J. Asian Earth Sci. 156, 122–144.

Kohn, M.J., 2008. P-T-t data from central Nepal support critical taper and repudiate large-scale channel flow of the Greater Himalayan Sequence. Geol. Soc. Am. Bull. 120, 259–73.

Kohn, M.J., 2014. Himalayan Metamorphism and Its Tectonic Implications. Amu. Rev. Earth Planet. Sci. 42, 381–419.

Kriegsman, L.M., Schumacher, J.C., 1999. Petrology of sapphirine-bearing and associated granulites from central Sri Lanka. J. Petrol. 40, 1211–1239.

Leake, B.E., Woolley, A.R., Arps, C.E.S., Birch, W.D., Gilbert, M.C., Grice, J.D., Hawthorne, F.C., Kato, A., Kisch, H.J., Krivovichev, V.G., Linthout, K., Laird, J., Mandarino, J.A., Maresch, W.V., Nickel, E.H., Rock, N.M.S., Schumacher, J.C., Smith, D.C., Stephenson, N.C.N., Ungaretti, L., Whittaker, E.J.W., Youzhi, G., 1997. Nomenclature of amphiboles: report of the subcommittee on amphiboles of the International Mineralogical Association, commission on new minerals and mineral names. Amer. Mineral. 82, 1019–1037.

Ludwig, K.R., 2008. User's Manual for Isoplot 3.70. Berkeley Geochronology Center Special Publication, No. 4, p. 70.

Maas, R., Kinny, P.D., Williams, I.S., Froude, D.O., Compston, W., 1992. The Earth's oldest known crust: a geochronological and geochemical study of 3900–4200 Ma old detrital zircons from Mt. Narryer and Jack Hills, Western Australia. Geochim. Cosmochim. Acta 56, 1281–1300.

McDonough, W.F., Sun, S.S., 1995. The composition of the Earth. Chem. Geol. 120, 223–253.

Meert, J., 2003. A synopsis of events related to the assembly of eastern Gondwana. Tectonophysics 362, 1–40.

Meert, J.G., Lieberman, B.S., 2008. The Neoproterozoic assembly of Gondwana and its relationship to the Ediacaran-Cambrian radiation. Gondwana Res. 14, 5–21.

Meschede, M., 1986. A method of discriminating between different types of mid-ocean ridge basalts and continental tholeiites with the Nb-Zr-Y diagram. Chem. Geol. 56, 207–218.

Moecher D.P., Essene, E.J., Anovitz, L.M., 1988. Calculation and application of clinopyroxene-garnet-plagioclase-quartz geobarometers. Contrib. Mineral. Petrol. 100, 92–106.

Mullen, E.D., 1983. $MnO/TiO_2/P_2O_5$ a minor element discriminations for basaltic rocks of oceanic environments and its implications for petrogenesis. Earth Planet. Sci. Lett. 62, 53–62.

Nakamura, A., Kitamura, M., Kawakami, T., 2013. Microstructural records of multiple retrograde local H_2O supplement in the pelitic gneiss, Lützow-Holm Complex at Akarui Point, East Antarctica. Mineral. Petrol. 108 (2), 177–186.

Nakajima, T., Shibata, K., shiraishi, K., Motoyoshi, Y., Hiroi, Y., 1988. Rb-Sr WHOLE-ROCK AGES OF METAMORPHIC ROCKS FROM EASTERN QUEEN MAUD LAND, EAST ANTARCTICA (2): TENMONDAI ROCK AND RUNDVÅGSHETTA. Proc. NIPR Symp. Antarct. Geosci. 2, 172.

Newton, R.C., Haselton, H.J., 1981. Thermodynamics of the garnet-plagioclase-Al_2SiO_5-quartz geobarometer; *in* Newton R.C., Navrotsky, A. and Wood, B.J. (eds.) Thermodynamics of Mineral and Melts. Springer-Verlag, New York, 125–145.

Nogi, Y., Jokat, W., Kitada, K., Steinhage, D., 2013. Geological structures inferred from airborne geophysical surveys around Lützow-Holm Bay, East Antarctica. Precambrian Res. 234, 279–287.

Osanai, Y., Toyoshima, T., Owada, M., Tsunogae, T., Hokada, T., Crowe, W.A., Ikeda, T.,Kawakami, T., Kawano, Y., Kawasaki, T., Ishikawa, M., Motoyoshi, Y., Shiraishi, K., 2004. Explanatory text of geological map of Skallen, Antarctica (revised edition).

Antarctic Geological Map Series, Sheet 39 Skallen (revised edition), National Institute of Polar Research, Japan.

Osanai, Y., Sajeev, K., Owada, M., Kehelpannala, K.V.W., Prame, W.K.B., Nakano, N., Jayatileke, S., 2006. Metamorphic evolution of ultrahigh-temperature and high pressure granulites from Highland Complex. Sri Lanka. J. Asian Earth Sci. 28, 20–37.

Osanai, Y., Sajeev, K., Nakano, N., Kitano, I., Kehelpannala, W. K., Adachi, T., Malaviarachchi, S. P., 2016a. UHT granulites of the Highland Complex, Sri Lanka I: Geological and petrological background. J. Mineral. Petrol. Sci. 111, 145–156.

Osanai, Y., Sajeev, K., Nakano, N., Kitano, I., Kehelpannala, W. K., Adachi, T., Malaviarachchi, S. P., 2016b. UHT granulites of the Highland Complex, Sri Lanka II: Geochronological constraints and implications for Gondwana correlation. J. Mineral. Petrol. Sci. 111, 157–169.

Paces, J.B., Miller, J.D., 1993. Precise U–Pb ages of Duluth Complex and related mafic intrusions, northeastern Minnesota: geochronological insights to physical, petrogenetic, paleomagnetic and tectonomagmatic processes associated with the 1.1 Ga midcontinent rift system. J. Geophys. Res. 98, 13997–14013.

Peace, J.A., 2008. Geochemical fingerprinting of oceanic basalts with applications to ophiolite classification and the search for Archean oceanic crust. Lithos 100, 14–48.

Perkins, D., Newton, R.C., 1981. Charnockite geobarometers based on coexistence garnet-pyroxene-plagioclase-quartz. Nature 292, 144–146.

Powell, R., Holland, T.J.B., 1988. An internally consistent thermodynamic dataset with uncertainties and correlations: 3. application, methods, worked examples and a computer program. J. Metamorph. Geol. 6, 173–204.

Rubatto, D., 2002. Zircon trace element geochemistry: distribution coefficients and the link between U-Pb ages and metamorphism. Chem Geol 184,123–138.

Rubatto, D., 2017. Zircon: the metamorphic mineral. Rev. Min. Geochem. 83.

Rubatto, D., Chakraborty, S., Dasgupta, S., 2013. Timescales of crustal melting in the Higher Himalayan Crystallines (Sikkim, Eastern Himalaya) inferred from trace element-constrained monazite and zircon chronology. Contrib. Mineral Petrol. 165, 349–372.

Sajeev, K., Osanai, Y., 2004a. Ultrahigh-temperature metamorphism (1150°C, 12 kbar) and multistage evolution of Mg-, Al-rich granulites from the Central Highland Complex Sri Lanka. J. Petrol. 45, 1821–1844.

Sajeev, K., Osanai, Y., 2004b. 'Osumilite' and 'spinel + quartz' from Highland Complex, Sri Lanka: a case of cooling and decompression after ultrahigh-temperature metamorphism. J. Min. Petrol. Sci. 99, 320–327.

Sajeev, K., Osanai, Y., Connolly, J.A.D., Suzuki, S., Ishioka, J., Kagami, H., Rino, S., 2007. Extreme crustal metamorphism during a neoproterozoic event in Sri Lanka: a study of dry mafic granulites. J. Geol. 115, 563–582.

Santosh, M., Maruyama, S., Sato, K., 2009. Anatomy of a Cambrian suture in Gondwana: pacific-type orogeny in southern India? Gondwana Res. 16, 321–341.

Santosh, M., Tsunogae, T., Malaviarachchi, S.P.K., Zhang, Z., Ding, H., Tang, L., Dharmapriya, P.L., 2014. Neoproterozoic crustal evolution in Sri Lanka: insights from petrologic, geochemical and zircon U–Pb and Lu–Hf isotopic data and implications for Gondwana assembly. Precambrian Res. 255, 1–29.

Santosh, M., Yang, Q.Y., Shaji, E., Tsunogae, T., Ram Mohan, M., Satyanarayanan, M., 2015. An exotic Mesoarchean microcontinent: the Coorg Block, southern India. Gondwana Res. 27, 165–195.

Santosh, M., Yang, Q. Y., Shaji, E., Mohan, M. R., Tsunogae, T., Satyanarayanan, M., 2016. Oldest rocks from Peninsular India: evidence for Hadean to Neoarchean crustal evolution. Gondwana Res. 29, 105–135.

Santosh, M., Hu, C.N., He, X.F., Li, S.S., Tsunogae, T., SHaji, E., Indu, G., 2017. Neoproterozoic arc magmatism in the southern Madurai Block, India: Subduction, relamination, continental outbuilding, and the growth of Gondwana. Gondwana Res. 45, 1–42.

Satish-Kumar, M., Hermann, J., Tsunogae, T., Osanai, Y., 2006. Carbonation of Cl-rich scapolite boudins in Skallen, East Antarctica: evidence for changing fluid condition in the continental crust. J. Metamorph. Geol. 24, 241–261.

Shiraishi, K., Hiroi, Y., Moriwaki, K., 1985. Geological Map of Tenmondai Rock (Antarctic geological map series, sheet 19). National Institute of Polar Research, Tokyo, Japan.

Shiraishi, K., Hiroi, Y., Motoyoshi, Y., 1989. 1:250,000 Geological Map of Lützow-Holm Bay. National Institute of Polar Research, Tokyo, Japan.

Shiraishi, K., Ellis, D.J., Hiroi, Y., Fanning, C.M., Motoyoshi, Y., Nakai, Y., 1994. Cambrian orogenic belt in east Antarctica and Sri Lanka: implications for Gondwana assembly. J. Geol. 102, 47–65.

Shiraishi, K., Hokada, T., Fanning, C.M., Misawa, K., Motoyoshi, Y., 2003. Timing of thermal events in eastern Dronning Maud Land, East Antarctica. Polar Geosci. 16, 76–99.

Shiraishi, K., Dunkley, D.J., Hokada, T., Fanning, C.M., Kagami, H., Hamamoto, T., 2008. Geochronological constraints on the Late Proterozoic to Cambrian crustal evolution of eastern Dronning Maud Land, East Antarctica: a synthesis of SHRIMP U-Pb age and Nd model age data. Geolog. Soc. Lond. Spec. Publ., 21–67.

Stacey, J.S., Kramers, J.D., 1975. Approximation of terrestrial lead isotope evolution by a two-stage model. Earth Planet. Sci. Lett. 26, 207–221.

Sun, S.S., McDonough, W.F., 1989. Chemical and isotopic systematics of oceanic basalts: Implications for mantle composition and processes. Geol. Soc. Spec. Publ.

42, 313–345.

Takahashi, K., Tsunogae, T., 2017. Carbonic fluid inclusions in a garnet–pyroxene granulite from Austhovde in the Lützow–Holm Complex, East Antarctica: Implications for a decompressional *P–T* path. J. Minral. Petrol. Sci. 112, 132–137.

Takahashi, K., Tsunogae, T., Santosh, M., Takamura, Y., Tsutsumi, Y., 2018. Paleoproterozoic (ca. 1.8 Ga) arc magmatism in the Lützow-Holm Complex, East Antarctica: implications for crustal growth and terrane assembly in erstwhile Gondwana fragments. J. Asian Earth Sci. 157, 245–268.

Takamura, Y., Tsunogae, T., Santosh, M., Malaviarachchi, S.P.K., Tsutsumi, Y., 2015. Petrology and zircon U–Pb geochronology of metagabbro from the Highland Complex, Sri Lanka: Implications for the correlation of Gondwana suture zones. J. Asian Earth Sci. 113, 826–841.

Takamura, Y., Tsunogae, T., Santosh, M., Tsutsumi, Y., 2018. Detrital zircon geochronology of the Lützow-Holm Complex, East Antarctica: Implications for Antarctica-Sri Lanka correlation. Geosci. Front. 9, 355–375.

Thompson, A.B., 1976. Mineral reactions in pelitic rocks: II. Calculations of some P-T-X (Fe-Mg) phase relations. Am. J. Sci. 276, 425–454.

Tsunogae, T., Dunkley, D.J., Horie, K., Endo, T., Miyamoto, T., Kato, M., 2014. Petrology and SHRIMP zircon geochronology of granulites from Vesleknausen, Lützow-Holm Complex, East Antarctica: Neoarchean magmatism and Neoproterozoic high-grade metamorphism. Geosci. Front. 5, 167–182.

Tsunogae, T., Yang, Q.Y., Santosh, M., 2015. Early Neoproterozoic arc magmatism in the Lützow-Holm Complex, East Antarctica: petrology, geochemistry, zircon U–Pb geochronology and Lu–Hf isotopes and tectonic implications. Precambrian Res. 266, 467–489.

Tsunogae, T., Yang, Q. Y., Santosh, M., 2016. Neoarchean–Early Paleoproterozoic and

Early Neoproterozoic arc magmatism in the Lützow–Holm complex, East Antarctica: insights from petrology, geochemistry, zircon U–Pb geochronology and Lu–Hf isotopes. Lithos. 263, 239–256.

Tsutsumi, Y., Horie, K., Sano, T., Miyawaki, R., Momma, K., Matsubara, S., Shigeoka, M., Yokoyama, K., 2012. LA-ICP-MS and SHRIMP ages of zircons in chevkinite and monazite tuffs from the Boso Peninsula, Central Japan. Bull. Natl. Mus. Nat. Sci. Ser. C. Geol. Paleontol. 38, 15–32.

White, R.W., Powell, R., Holland, T.J.B., Worley, B.A., 2000. The effect of TiO2 and Fe2O3 on metapelitic assemblages at greenschist and amphibolite facies conditions: mineral equilibria calculations in the system K2O–FeO–MgO–Al2O3–SiO2–H2O–TiO2–Fe2O3. J. Metamorph. Geol. 18, 497–511.

White, R.W., Powell, R., Clarke, G.L., 2002. The interpretation of reaction textures in Fe–rich metapelitic granulites of the Musgrave Block, central Australia: constraints from mineral equilibria calculations in the system K2O–FeO–MgO–Al2O3–SiO2–H2O–TiO2–Fe2O3. J. Metamorph. Geol. 20, 41–55.

White, R.W., Powell, R., Holland, T.J.B., Johnson, T.E., Green, E.C.R., 2014. New mineral activity–composition relations for thermodynamic calculations in metapelitic systems. J. Metamorph. Geol. 32, 261–286.

Whitehouse, M.J., Platt, J.P., 2003. Dating high-grade metamorphism – constraints from rare-earth elements in zircon and garnet. Contrib. Mineral. Petrol. 145, 61–74.

Whitney, D.L., Evans, B., 2010 Abbreviations for names of rock-forming minerals. Amer. Mineral. 95, 185–187.

Williams, I.S., Claesson, S., 1987. Isotopic evidence for the Precambrian provenance and Caledonian metamorphism of high grade paragneisses from the Seve Nappes, Scandinavian Caledonides: II. Ion microprobe zircon U–Th–Pb. Contrib. Mineral. Petrol. 97, 205–217.

Williams, I.S., 1998. U–Th–Pb geochronology by ion microprobe. In: McKibben, M. A., Shanks, W.C. (Eds.), Applications of microanalytical techniques to understanding mineralizing processes, vol. 7, pp. 1–35, Rev. Econ. Geol.

Wilson, M., 1989. Igneous Petrogenesis: a Global Tectonic Approach. Unqin Hyman, London, 466.

Winchester, J.A., Floyd, P.A., 1977. Geochemical discrimination of different magma series and their differentiation products using immobile elements. Chem. Geol. 20. 325–343.

Yoshida, M., Funaki, M., Vitanage, P.W., 1992. Proterozoic to Mesozoic East Gondwana: The juxtaposition of India, Sri Lanka, and Antarctica. Tectonics 11, 381–391.

Yoshimura, Y., Motoyoshi, Y., Miyamoto, T., Grew, E.S., Carson, C.J., Dunkley, D.J., 2004. High-grade metamorphic rocks from Skallevikshalsen in the Lützow-Holm Complex, East Antarctica: metamorphic conditions and possibility of partial melting. Polar Geosci. 17, 57–87.

Yoshimura, Y., Motoyoshi, M., Miyamoto, T., 2008. Sapphirine + quartz association in garnet: Implication for ultrahigh-temperature metamorphism in Rundvågshetta, Lützow-Holm Complex, East Antarctica. Geol. Soc. London, Spec. Publ. 308, 377–390.

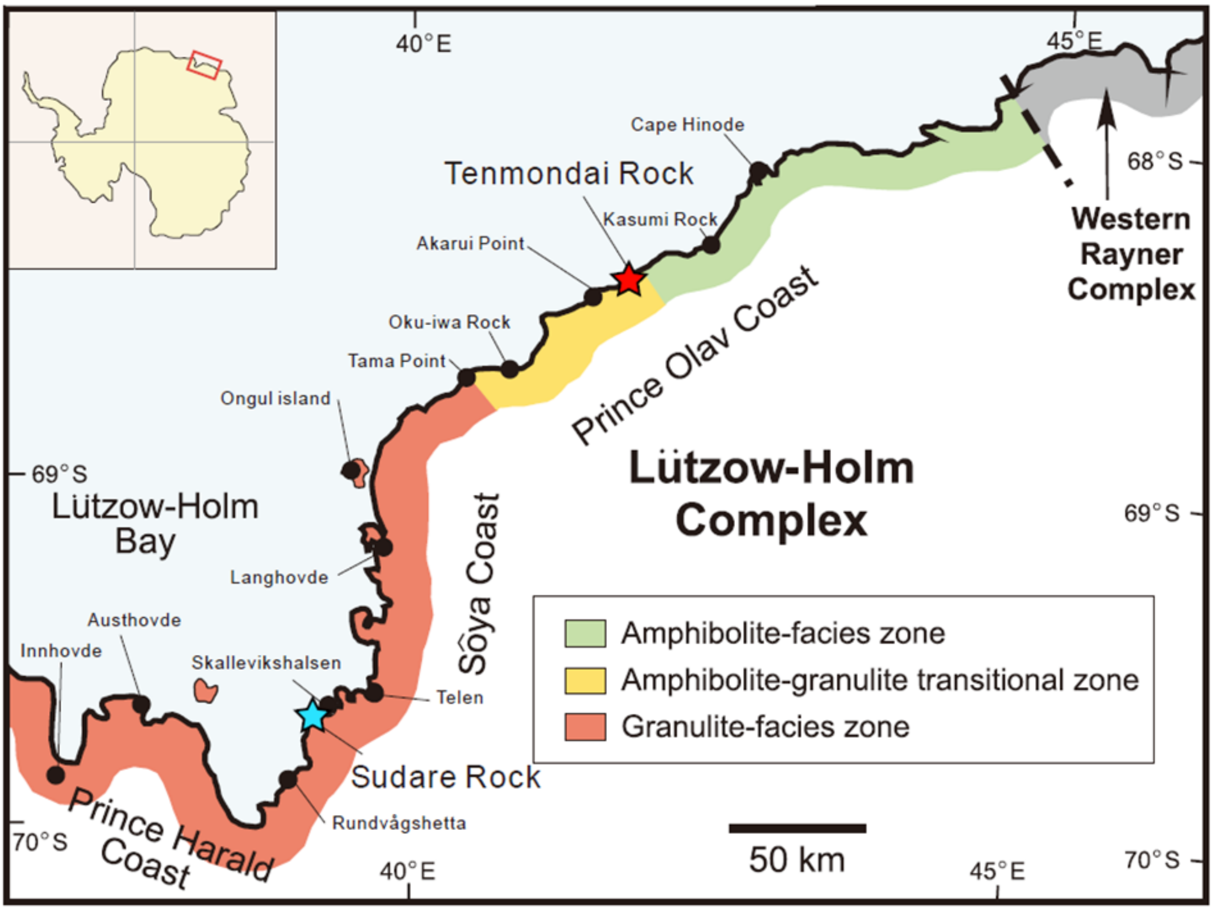

Figure 1. Generalized geological framework of the Lützow-Holm Complex, East Antarctica (after Hiroi et al., 1991). Star notation shows the location of Tenmondai Rock and Sudare Rock.

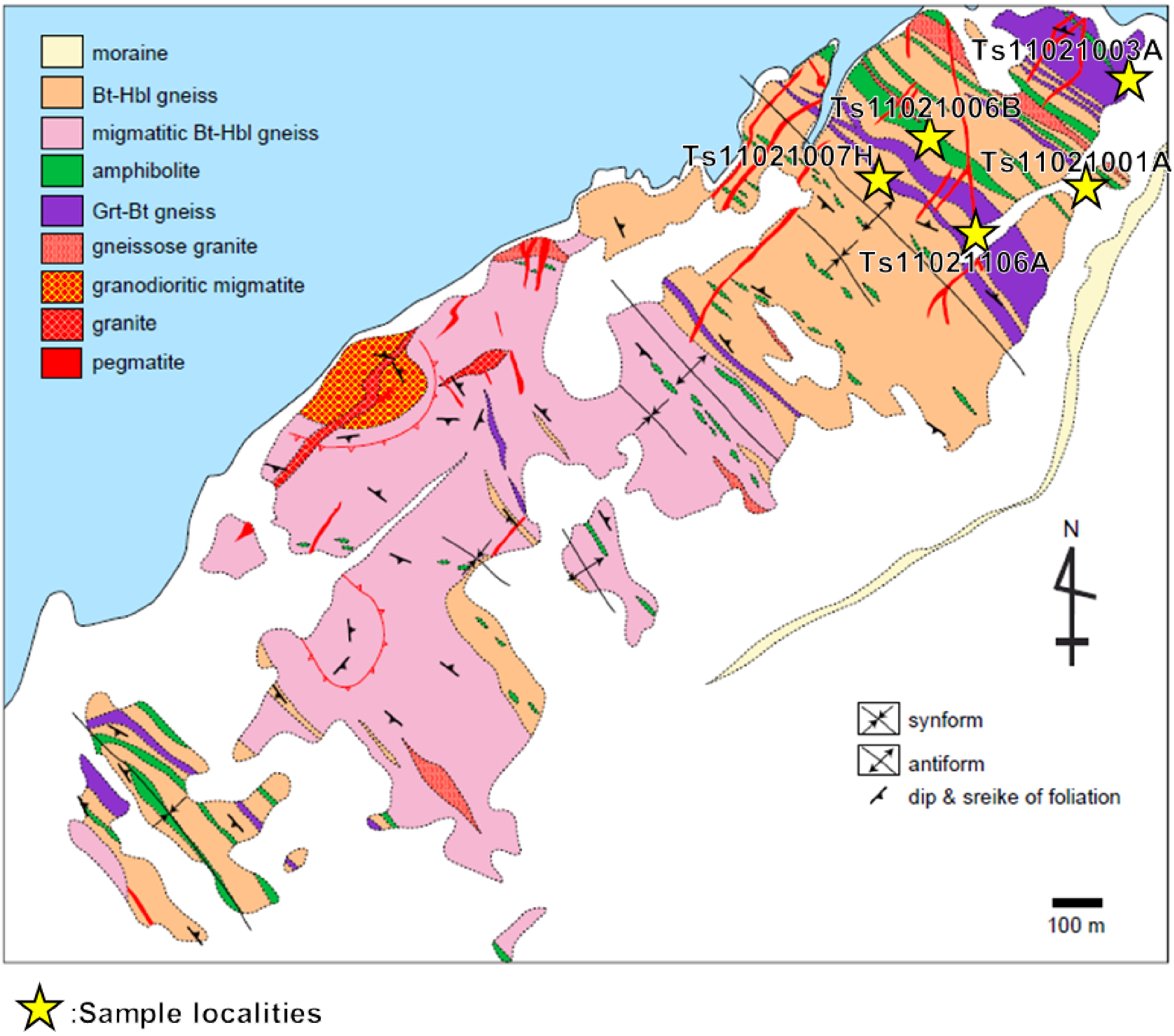

Figure 2. Geological map of Tenmondai Rock, the Lützow-Holm Complex (after Shiraishi et al., 1985), with sample localities shown by star notations.

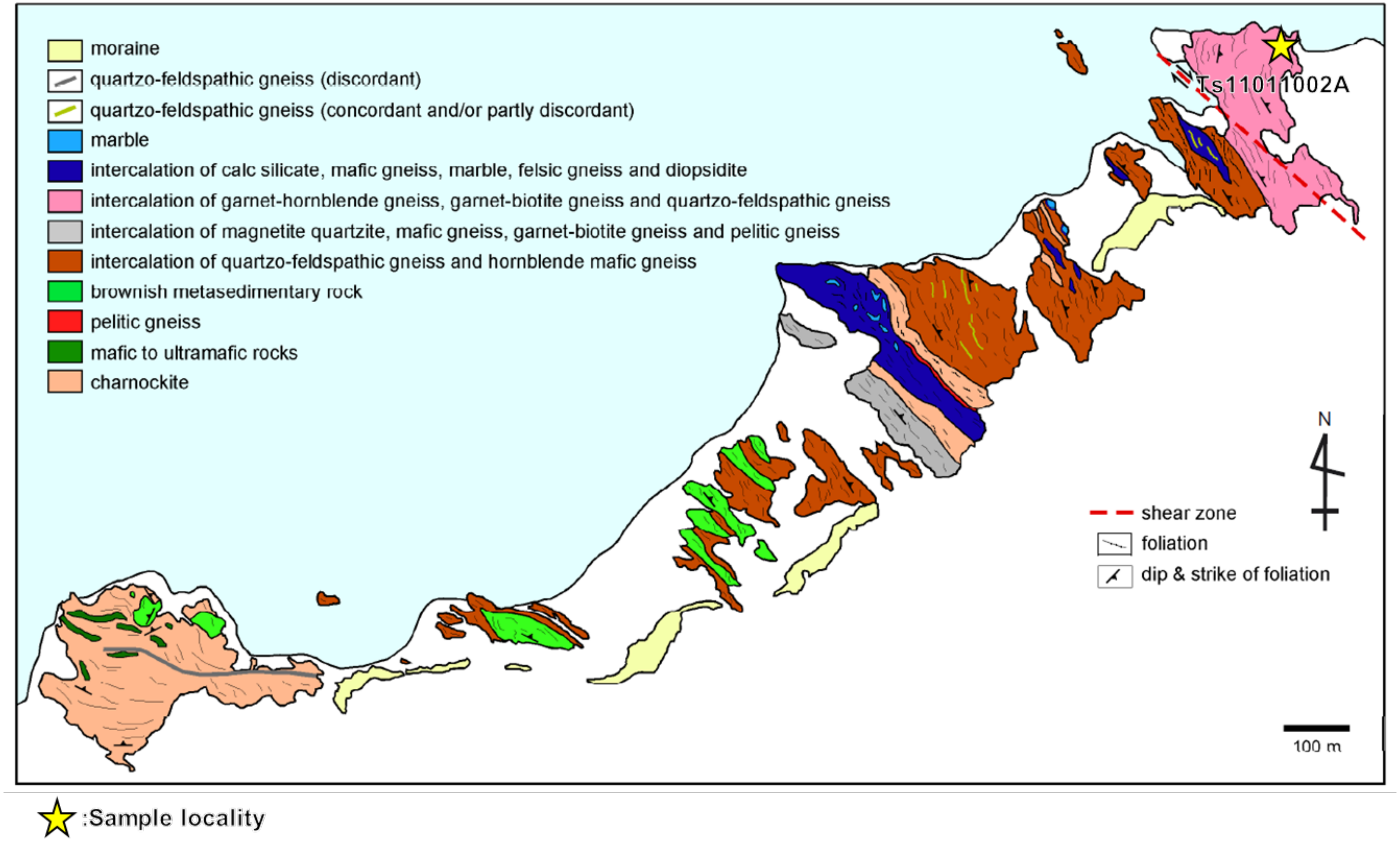

Figure 3. Geological map of Sudare Rock, the Lützow-Holm Complex (unpublished), with sample locality shown by a star notation.

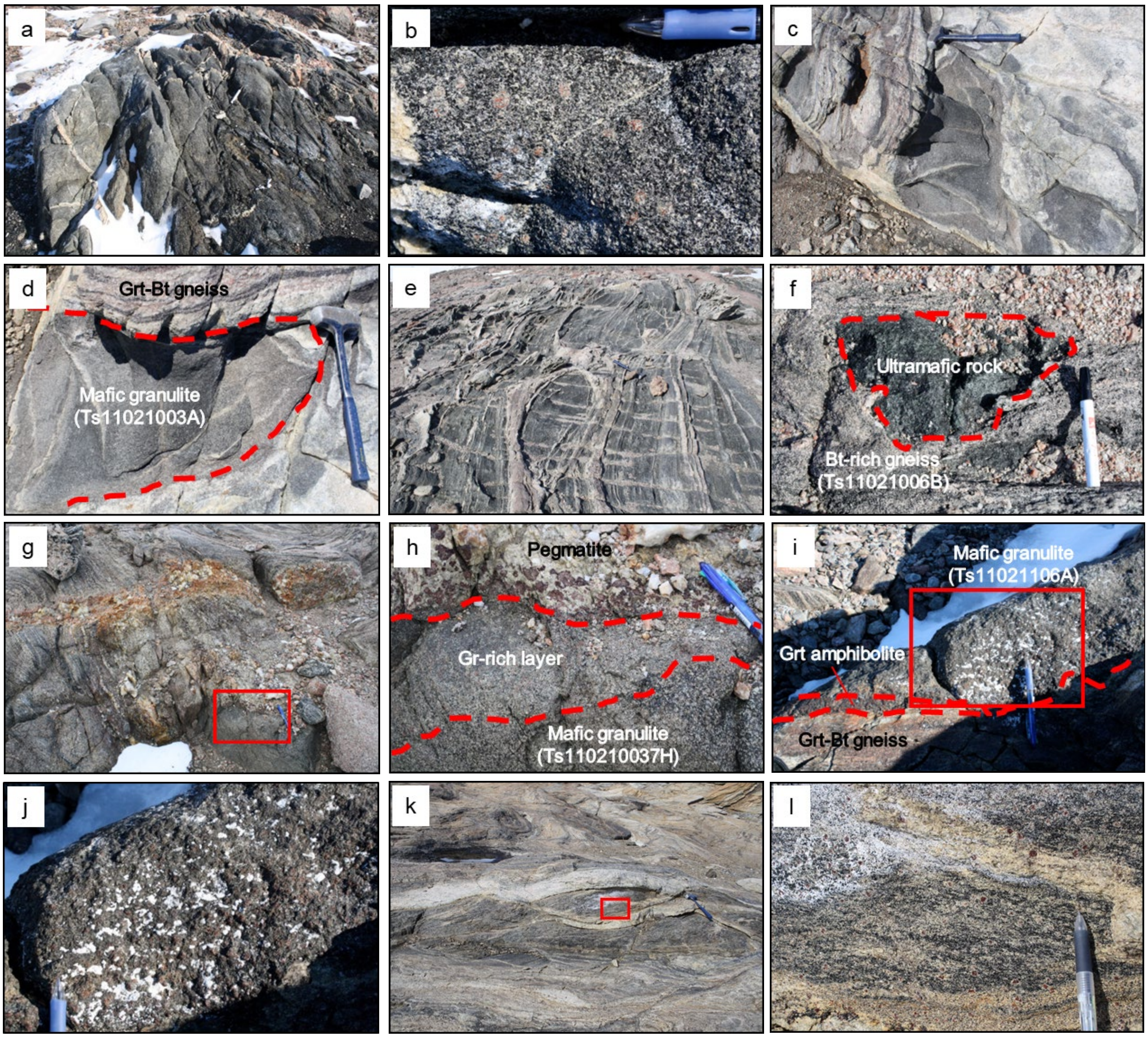

Figure 4. Field photographs of the metabasite samples from Tenmondai Rock (a-j) and Sudare Rock (k and l). (a) Exposure of garnet-bearing amphibolite (sample Ts11021001A). (b) Close-up view of sample Ts11021001A (c) and (d) Mafic granulite (sample Ts11021003A). (e) Felsic gneiss with mafic and ultramafic boudins. (f) Bt-rich gneiss (sample Ts11021006B) with ultramafic boudin. (g) Foliated pelitic gneiss which contains mafic lense/boudins and intruded by pegmatite. The red rectangle shows an area of Fig. 3g. (h) Mafic granulite (sample Ts11021007H) associated with pegmatite and garnet-rich layer between them. (i) Exposure of boudin of mafic granulite (sample Ts11021106A) in garnet-biotite gneiss. Mafic boudin is surrounded by garnet-bearing amphibolite. (j) Close-up view of sample Ts11021106A. (k) Mafic boudin in foliated garnet-biotite and quartzofeldspathic gneisses in Sudare Rock. (l) Close-up view of sample Ts11011002A.

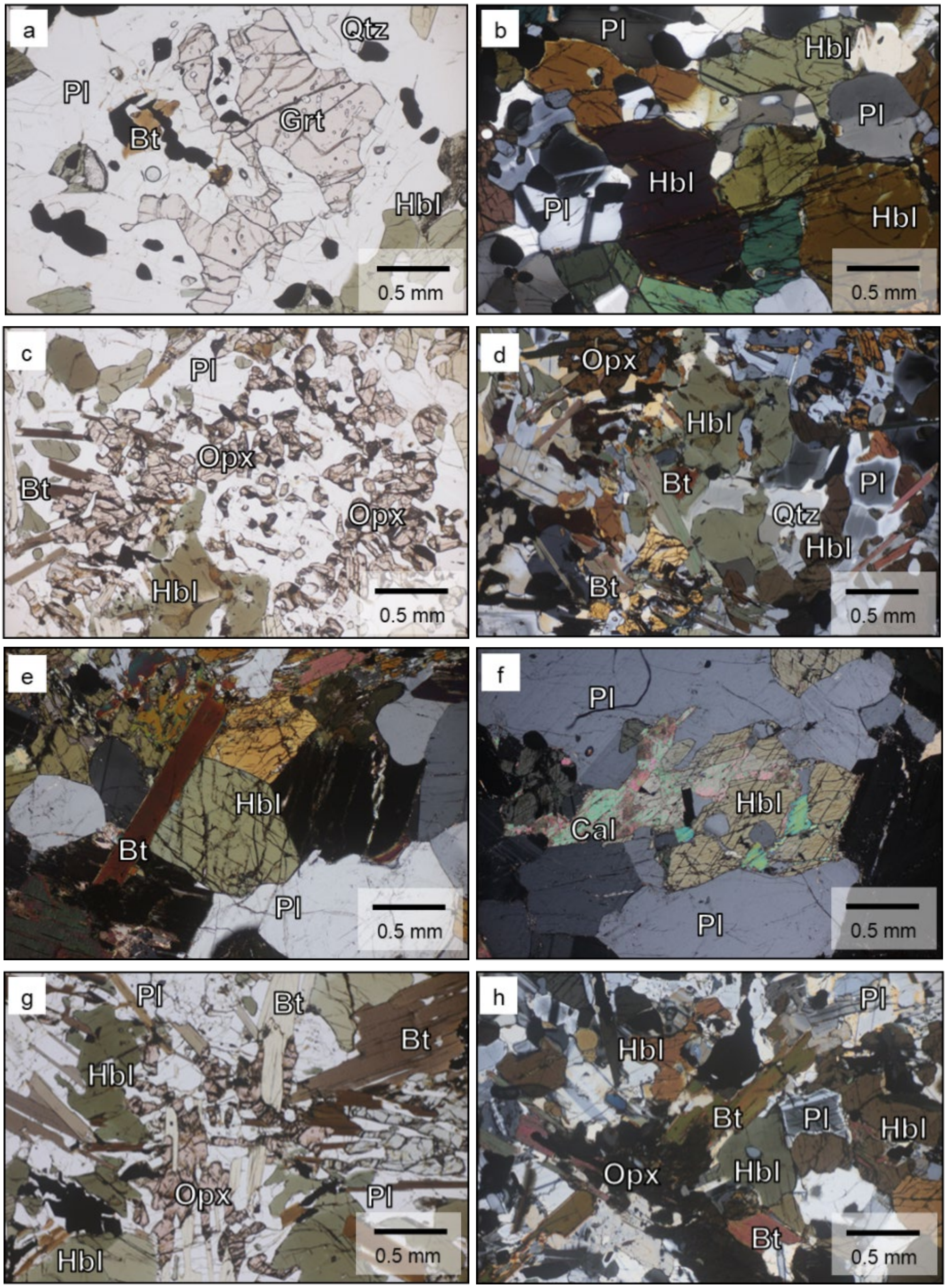

Figure 5. Photomicrographs of thin sections of metabasites from Tenmondai Rock. (a), (b) Ts11021001A. (c), (d) Ts11021003A. (e), (f) Ts11021006B. (g), (h) Ts11021007H.

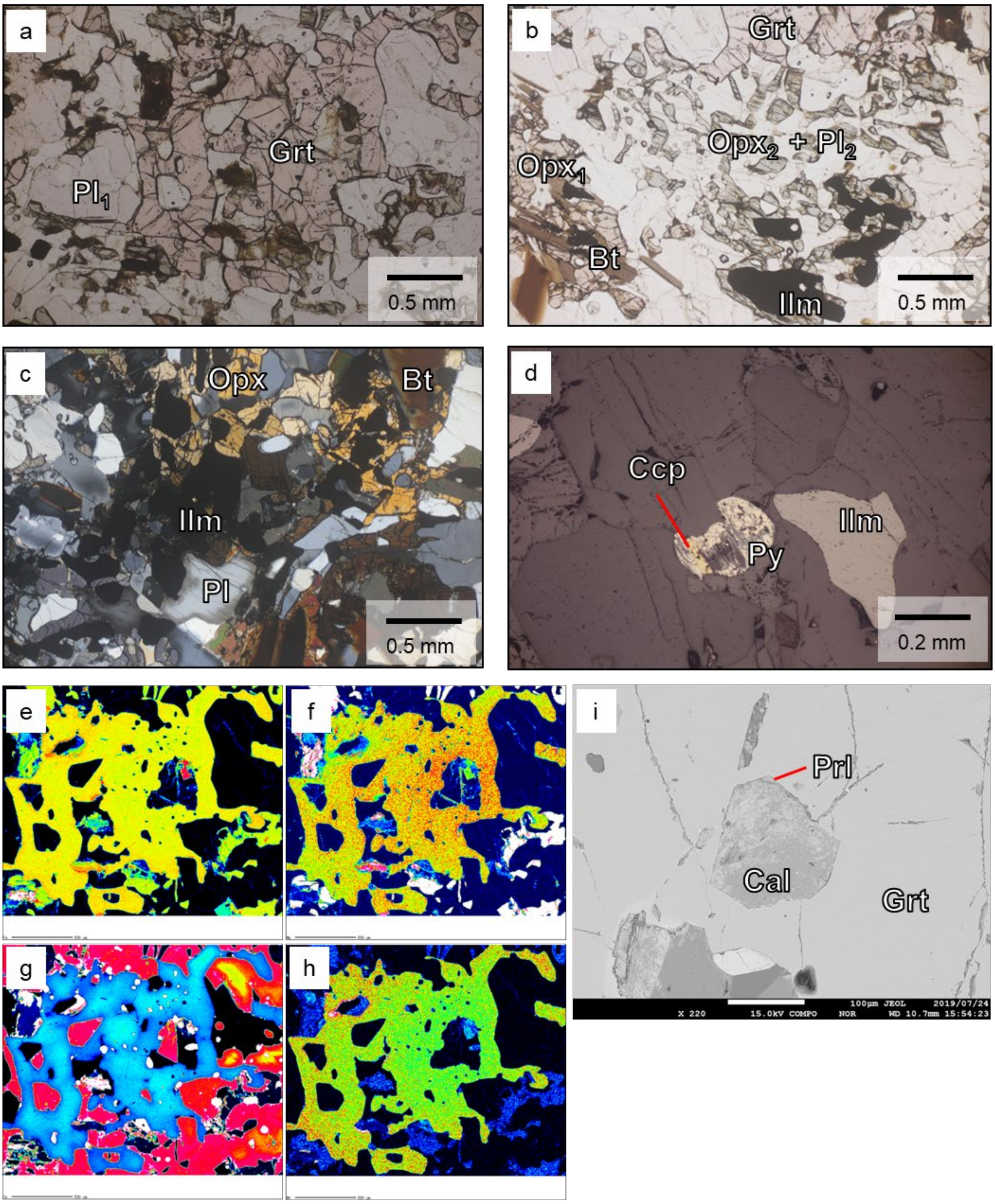

Figure 6. (a-d) Photomicrographs of thin sections of a mafic granulite from Tenmondai Rock (sample Ts11021106A). (e-h) X-ray elemental map of garnet in sample Ts11021106A, in terms of Fe (e), Mg (f), Ca (g) and Mn (h), respectively. (i) BSE image of polycrystalline inclusion showing obvious negative crustal shape in garnet of sample Ts11021106A.

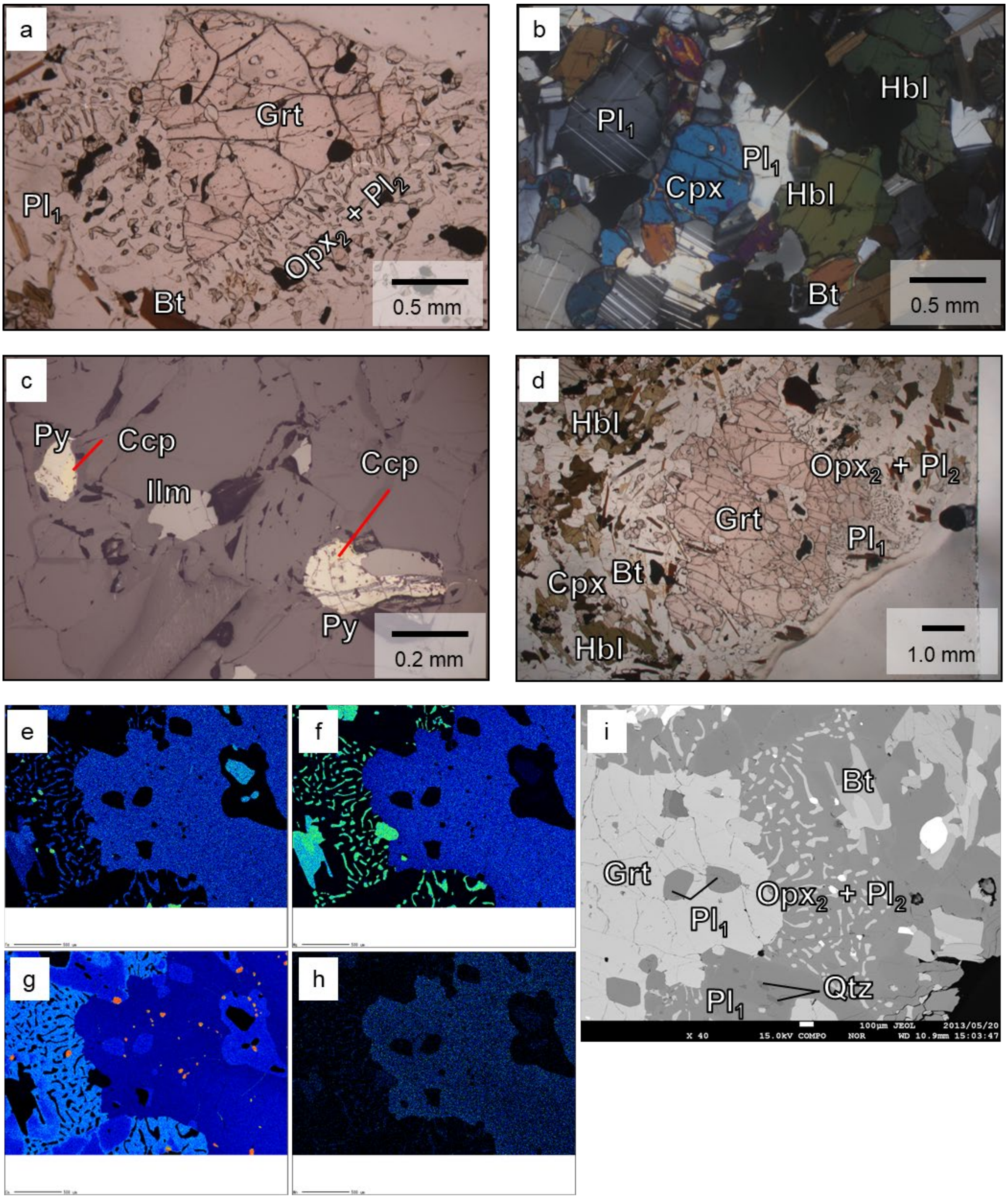

Figure 7. (a-d) Photomicrographs of thin sections of a mafic granulite from Sudare Rock (sample Ts11011002A). (e-h) X-ray elemental map of garnet in sample Ts11011002A, in terms of Fe (e), Mg (f), Ca (g) and Mn (h), respectively. (i) BSE image of garnet and surrounding orthopyroxene + plagioclase symplectite in sample Ts11011002A.

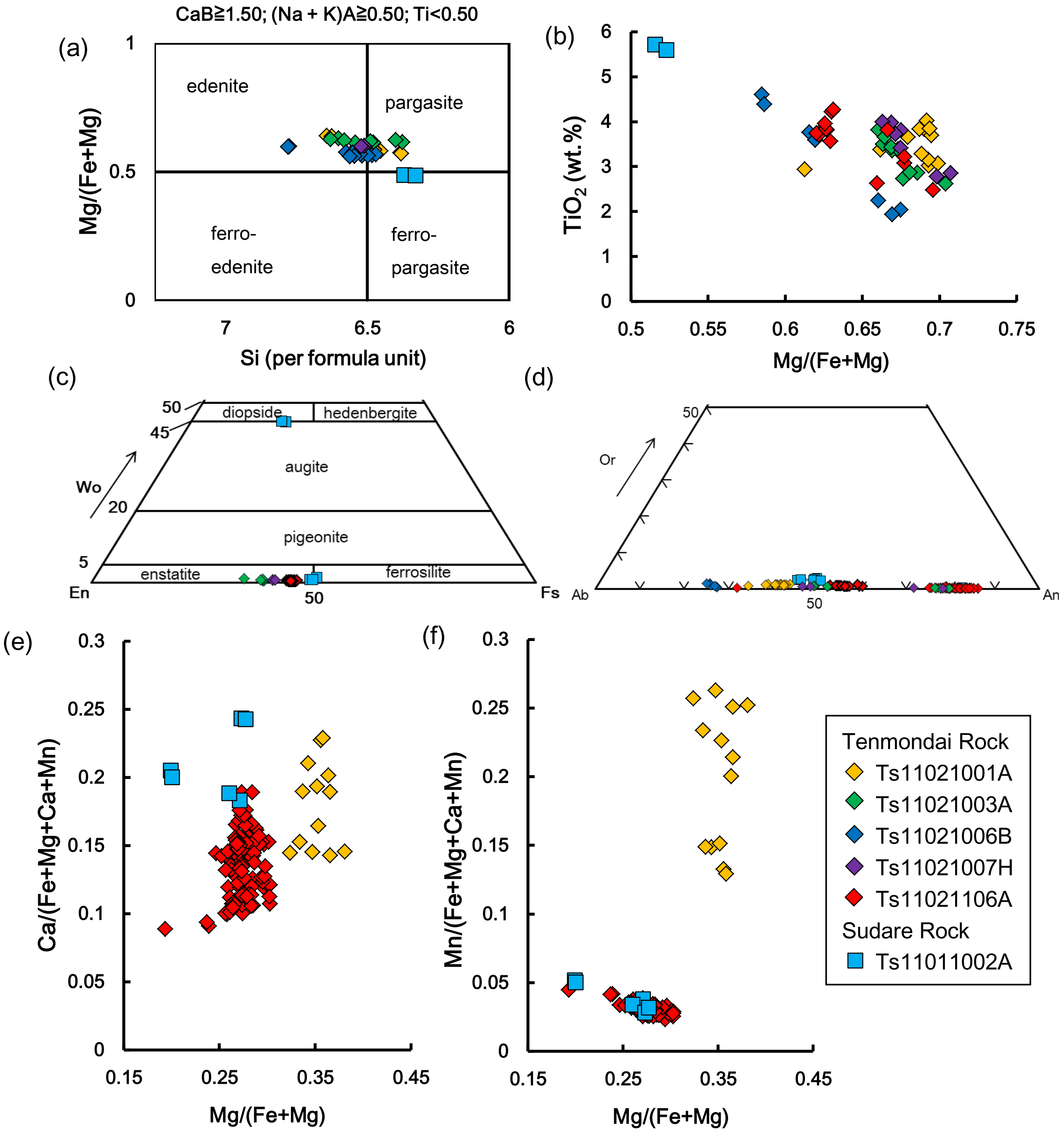

Figure 8. Compositional diagrams showing the chemistry of representative minerals. (a) Si versus X_{Mg} diagram showing the composition of calcic amphibolite. Classification of amphibolite is after Leake et al. (1997) (b) X_{Mg} versus TiO_2 diagram showing biotite chemistry. (c) Triangular diagram showing pyroxene chemistry. (d) Triangular diagram showing feldspar chemistry. (e) Ca/(Fe + Mg + Ca + Mn) versus X_{Mg} diagram showing garnet chemistry. (f) Mn/(Fe + Mg + Ca + Mn) versus X_{Mg} diagram showing garnet chemistry.

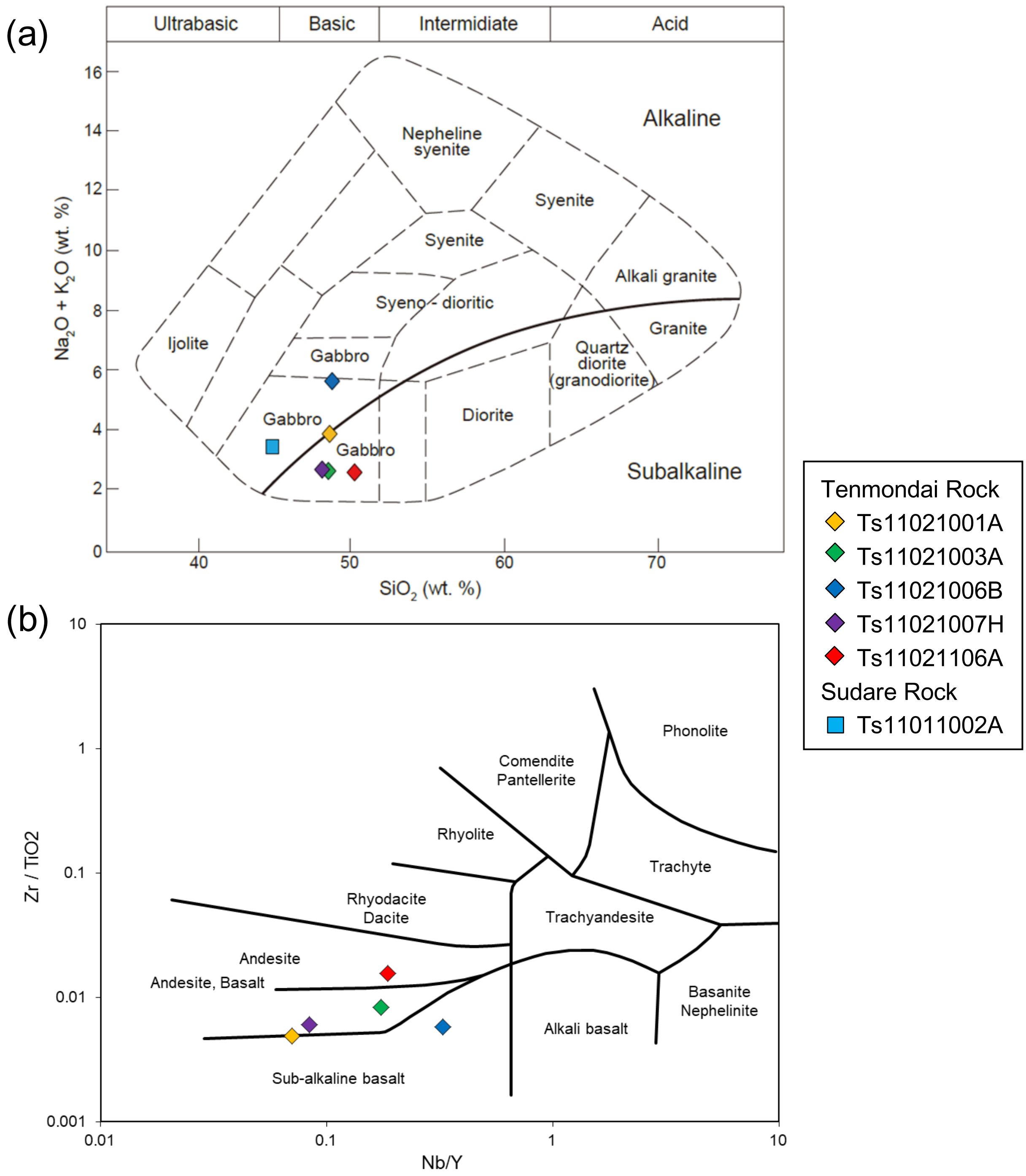

Figure 9. (a) Total alkali versus SiO_2 (TAS) diagram (after Wilson, 1989) and (b) Nb/Y versus Zr/TiO_2 diagram (after Winchester and Floyd, 1977), showing the classification of metabasites discussed in this study.

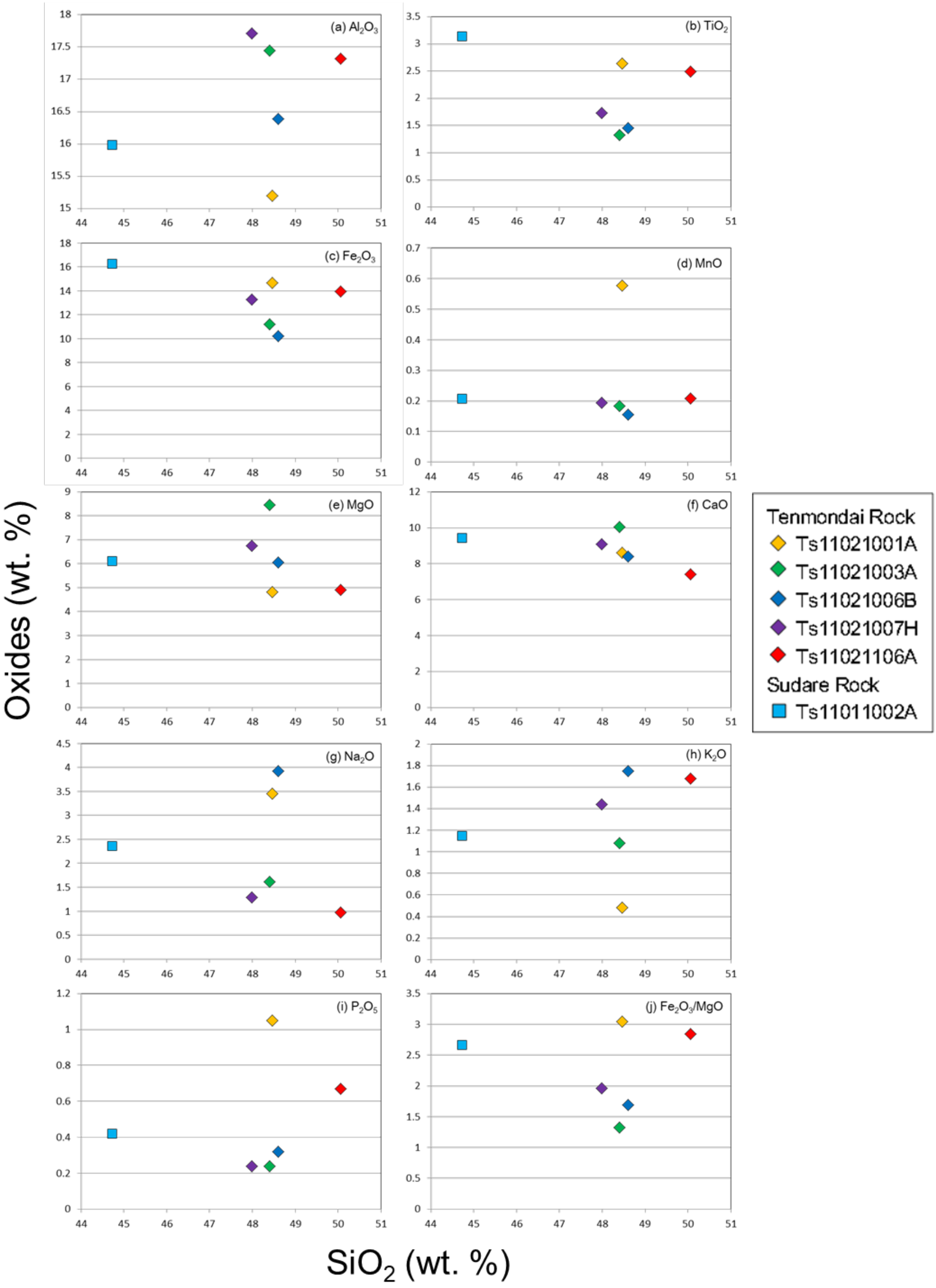

Figure 10. Major element variation diagrams (Harker diagram after Wilson, 1989) for metabasites from Tenmondai Rock and Sudare rock, the LHC.

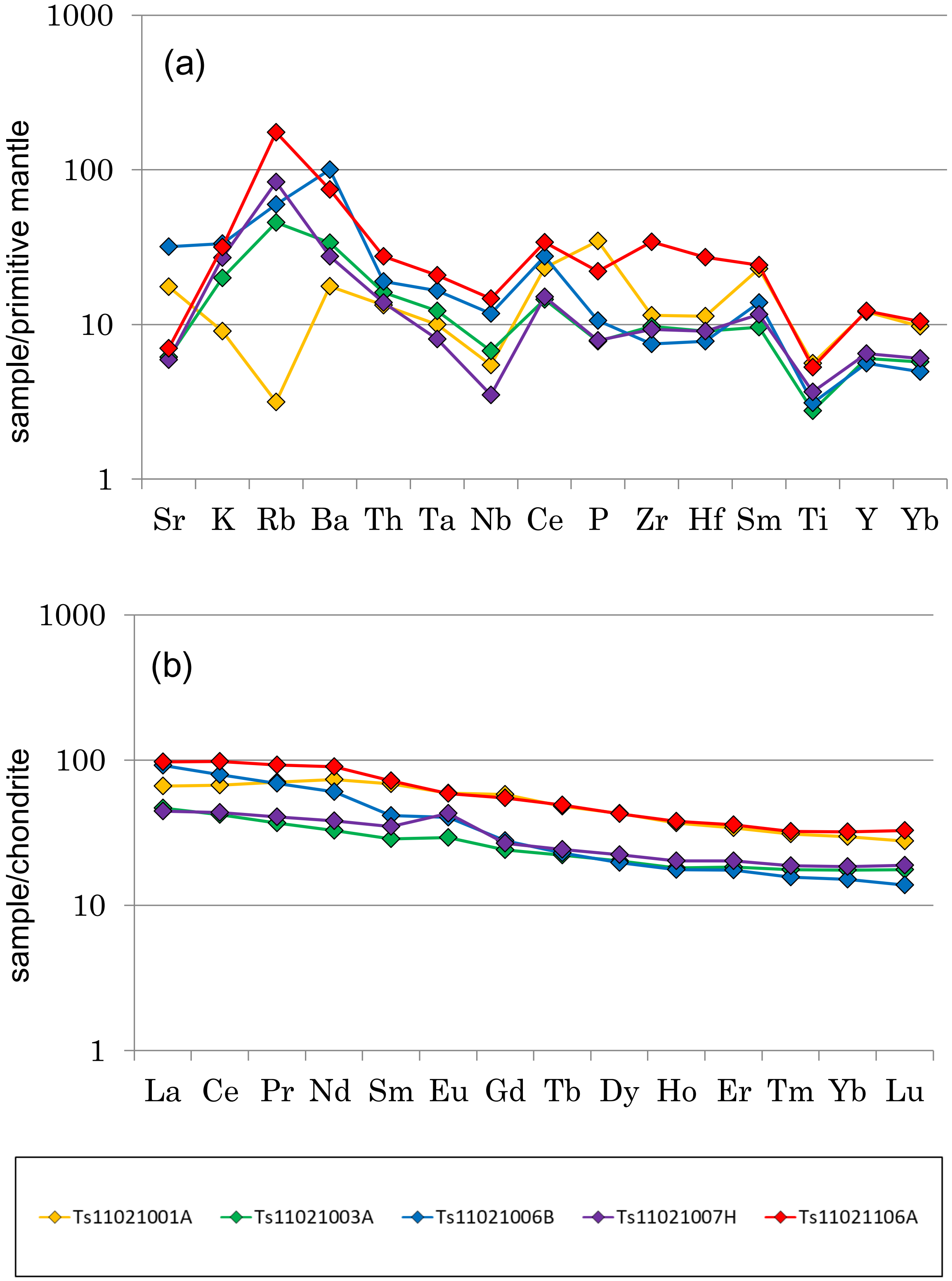

Figure 11. (a) Primitive mantle-normalized multi-element variation diagram for metabasites from Tenmondai Rock. Normalizing values are from Sun and McDonough (1989). (b) Chondrite-normalized REE spider plot for metabasites from Tenmondai Rock. Normalizing values are from McDonough and Sun (1995).

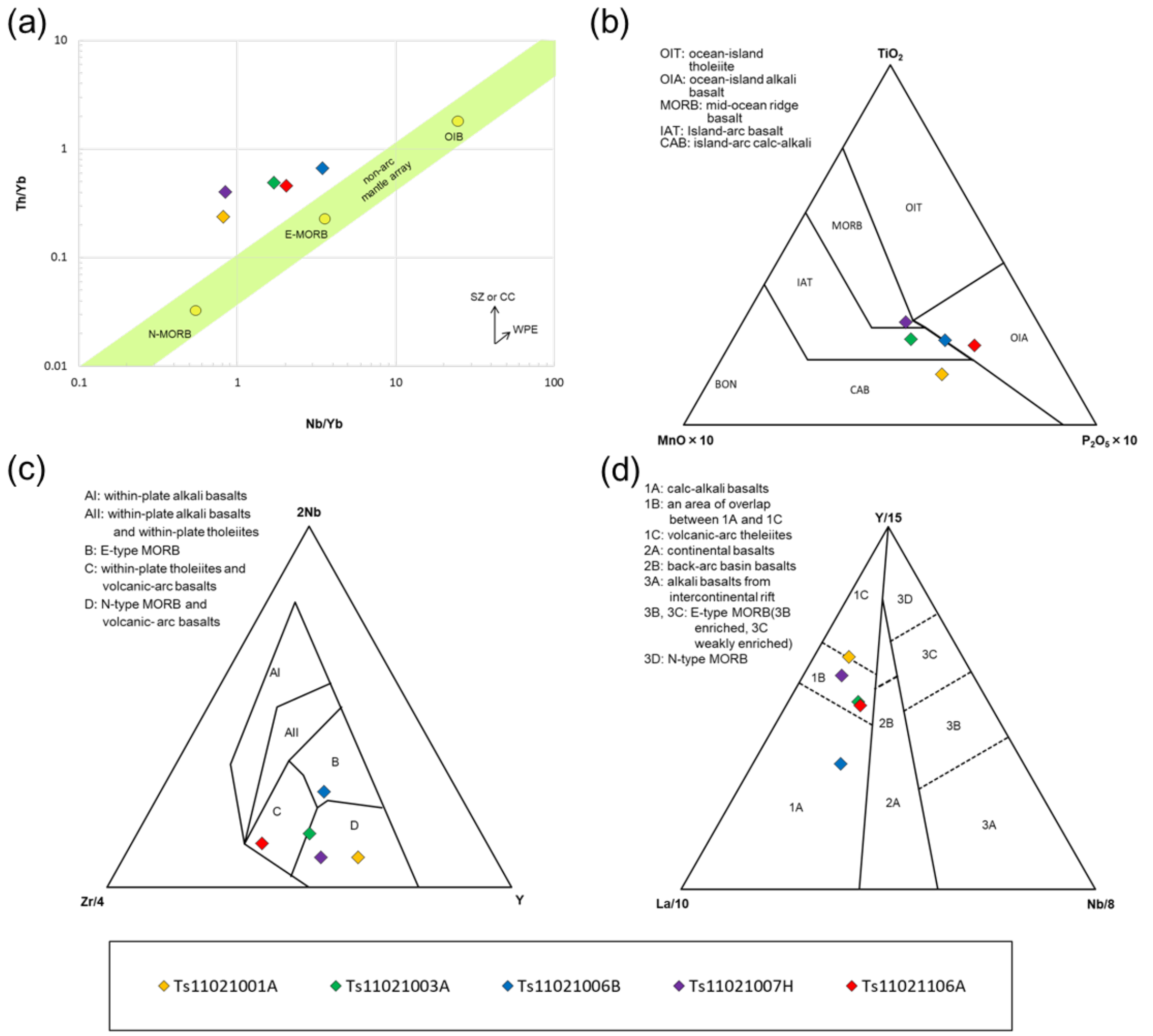

Figure 12. Discrimination diagrams showing the petrogenetic character of mafic rocks from Tenmondai Rock. (a) Th/Yb versus Nb/Yb plot (after Pearce, 2008). SZ: subduction-zone flux, CC: crustal contamination vector, WPE: within-plate enrichment. (b) TiO_2-MnO-P_2O_5 triangular diagram (after Mullen, 1983). CAB: island arc calc-alkaline basalts, IAT: island arc tholeiites, MORB: mid ocean ridge (and marginal basin) basalts, OIT: ocean island tholeiites, OIA: ocean island alkalic basalts, BON: boninites. (c) Nb-Zr-Y triangular diagram (after Meschede, 1986). AⅠ: within-plate alkali basalts, AⅡ: within-plate tholeiites and within-plate alkali basalts, B: P-type MORB, C: within-plate tholeiites and volcanic arc basalts, D: volcanic arc basalts and N-type MORB. (d) Y-La-Nb triangular diagram (after Cabanis and Lecolle, 1989). 1A: calc-alkali basalts, 1C: volcanic arc tholeiites, 1B: an area of overlap between 1A and 1C, 2A: continental basalts, 2B: back-arc basin basalts, 3A: alkali basalts from intercontinental rift, 3B: enriched E-MORB, 3C: weakly enriched E-MORB, 3D: N-MORB.

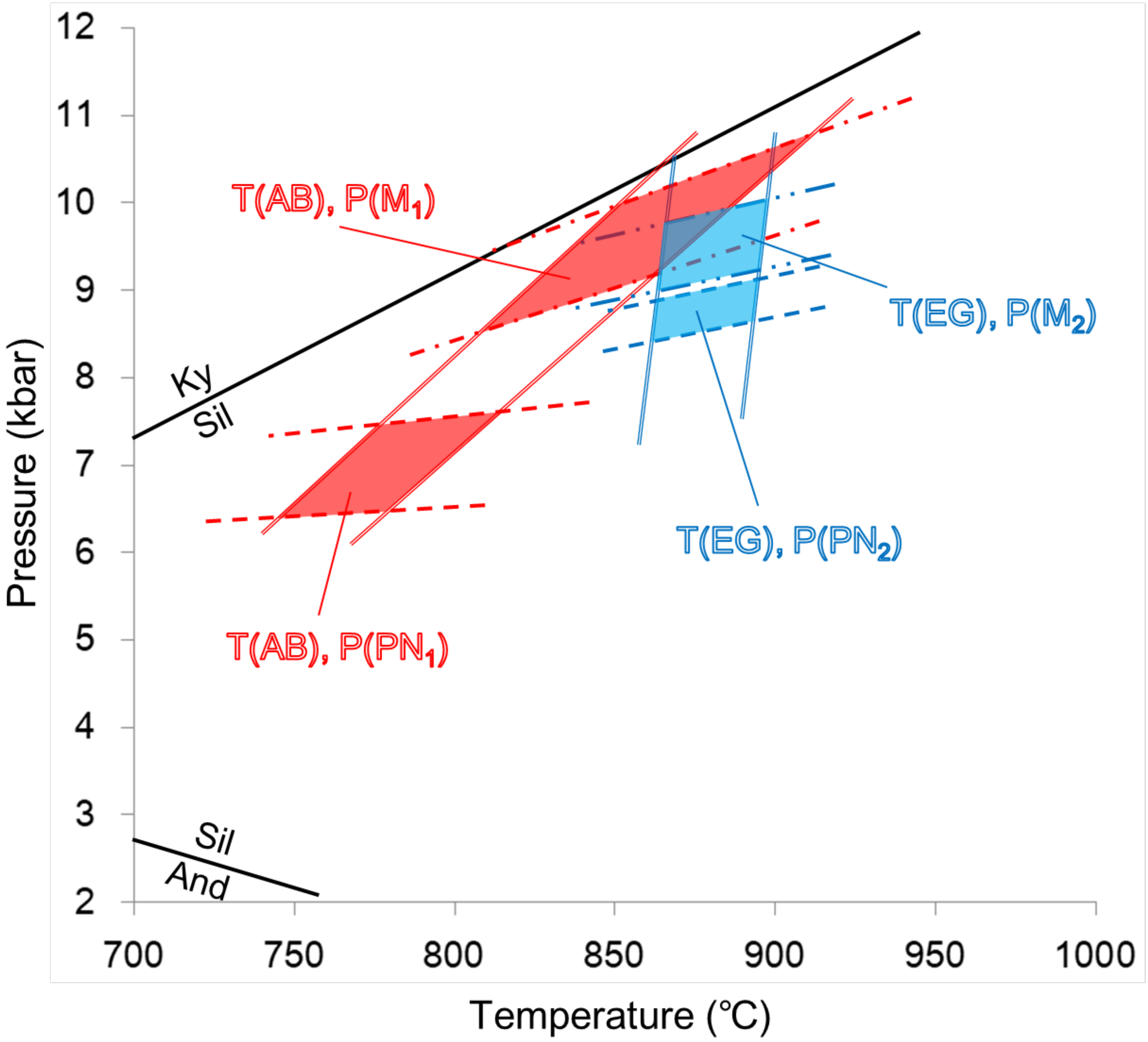

Figure 13. Summary of the results of geothermobarometry applied to samples Ts11021106A (red) and Ts11011002A (blue). T(AB): Garnet-orthopyroxene geothermometer on the method of Aranovich and Berman (1997). T(EG): Garnet-clinopyroxene geothermometer on the method of Ellis and Green (1979). P(M_1): Garnet-orthopyroxene-plagioclase-quartz geobarometer on the method of Moecher et al. (1988). P(M_2): Garnet-clinopyroxene (diopside)-plagioclase-quartz geobarometer on the method of Moecher et al. (1988). P(PN_1): Garnet-orthopyroxene-plagioclase-quartz geobarometer on the method of Parkins and Newton (1981). P(PN_2): Garnet-clinopyroxene-plagioclase-quartz geobarometer on the method of Parkins and Newton (1981).

Bulk rock composition [mol.%]

H_2O	SiO_2	Al_2O_3	CaO	MgO	FeO	K_2O	Na_2O	TiO_2	O
0.00	56.29	11.47	7.85	8.23	11.81	1.21	1.06	2.10	0.00
5.00	53.48	10.90	7.46	7.81	11.22	1.14	1.00	1.99	0.00

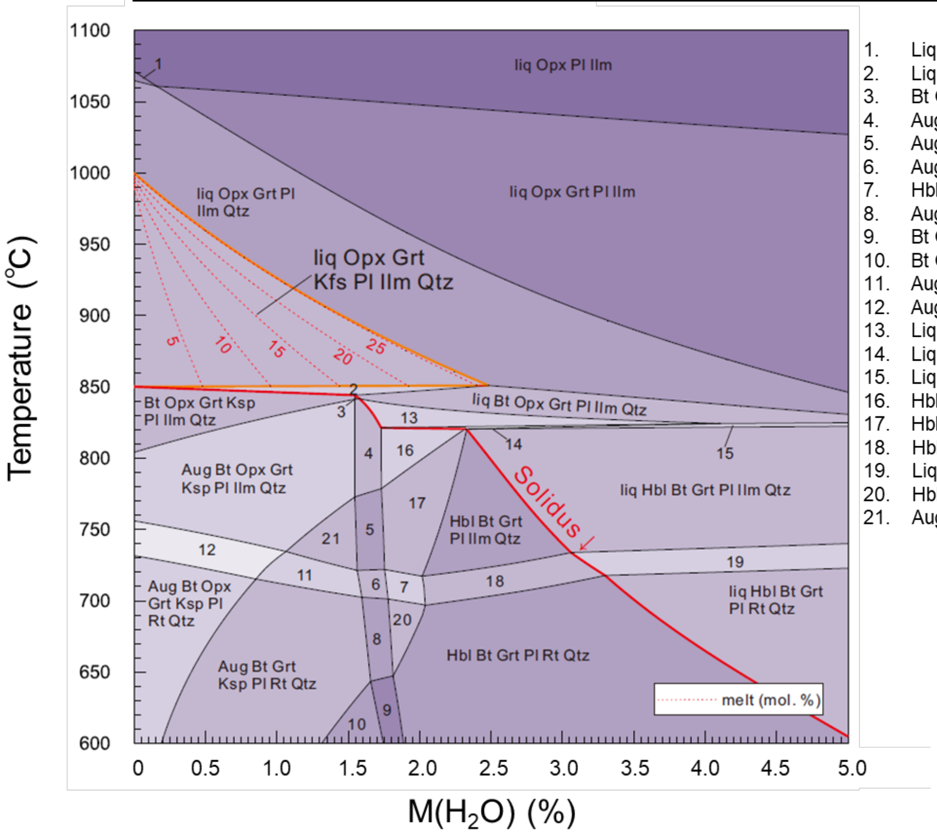

1. Liq Opx Pl Ilm Qtz
2. Liq Bt Opx Grt Kfs Pl Ilm Qtz
3. Bt Opx Grt Pl Ilm Qtz
4. Aug Bt Opx Grt Pl Ilm Qtz
5. Aug Bt Grt Pl Ilm Qtz
6. Aug Bt Grt Pl Ilm Rt Qtz
7. Hbl Aug Bt Grt Pl Ilm Rt Qtz
8. Aug Bt Grt Pl Rt Qtz
9. Bt Grt Pl Rt Qtz
10. Bt Grt Ksp Pl Rt Qtz
11. Aug Bt Grt Kfs Pl Ilm Rt Qtz
12. Aug Bt Opx Grt Kfs Pl Ilm Rt Qtz
13. Liq Aug Bt Opx Grt Pl Ilm Qtz
14. Liq Hbl Aug Bt Opx Grt Pl Ilm Qtz
15. Liq Hbl Bt Opx Grt Pl Ilm Qtz
16. Hbl Aug Bt Opx Grt Pl Ilm Qtz
17. Hbl Aug Bt Grt Pl Ilm Qtz
18. Hbl Bt Grt Pl Ilm Rt Qtz
19. Liq Hbl Bt Grt Pl Ilm Rt Qtz
20. Hbl Aug Bt Grt Pl Rt Qtz
21. Aug Bt Grt Kfs Pl Ilm Qtz

Figure 14. Temperature versus H_2O content (T-M[H_2O]) pseudosection calculated at 8 kbar. The field bordered orange line shows the stability field of peak mineral assemblage. Red dashed lines show modal isopleth of melt.

Bulk rock composition [mol.%]

H_2O	SiO_2	Al_2O_3	CaO	MgO	FeO	K_2O	Na_2O	TiO_2	O
0.50	56.01	11.41	7.81	8.18	11.75	1.20	1.05	2.09	0.00

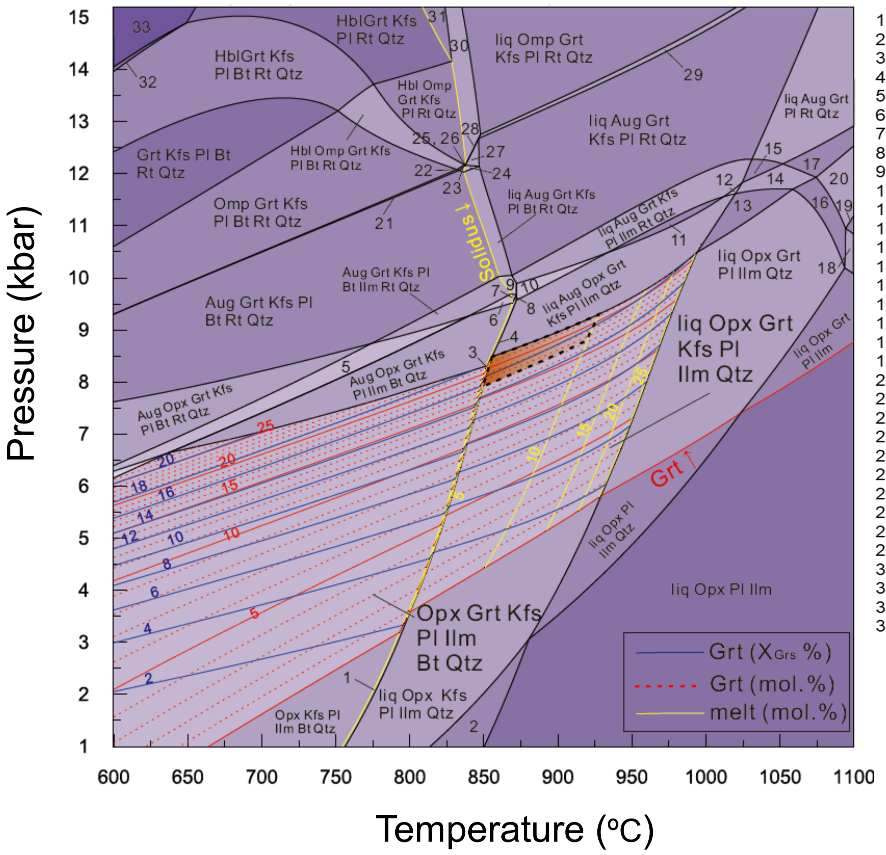

1. Liq Opx Kfs Pl Ilm Bt Qtz
2. Liq Opx Kfs Pl Ilm
3. Liq Opx Grt Kfs Pl Ilm Bt Qtz
4. Liq Aug Opx Grt Kfs Pl Ilm Bt Qtz
5. Aug Opx Grt Kfs Pl Ilm Bt Rt Qtz
6. Aug Grt Kfs Pl Ilm Bt Qtz
7. Liq Aug Grt Kfs Pl Ilm Bt Qtz
8. Liq Aug Opx Grt Kfs Pl Ilm Bt Rt Qtz
9. Liq Aug Grt Kfs Pl Ilm Bt Rt Qtz
10. Liq Aug Opx Grt Kfs Pl Ilm Rt Qtz
11. Liq Aug Grt Kfs Pl Ilm Qtz
12. Liq Aug Opx Grt Kfs Pl Ilm Rt Qtz
13. Liq Aug Opx Grt Pl Ilm Qtz
14. Liq Aug Opx Grt Pl Ilm Rt Qtz
15. Liq Aug Grt Pl Ilm Rt Qtz
16. Liq Opx Grt Pl Ilm Rt Qtz
17. Liq Aug Opx Grt Pl Rt Qtz
18. Liq Opx Grt Pl Ilm Rt
19. Liq Opx Grt Pl Rt
20. Liq Opx Grt Pl Rt Qtz
21. Aug Omp Grt Kfs Pl Bt Rt Qtz
22. Hbl Aug Omp Grt Kfs Pl Bt Rt Qtz
23. Hbl Aug Grt Kfs Pl Bt Rt Qtz
24. Liq Hbl Aug Grt Kfs Pl Bt Rt Qtz
25. Hbl Aug Omp Grt Kfs Pl Rt Qtz
26. Liq Hbl Aug Omp Grt Kfs Pl Bt Rt Qtz
27. Liq Hbl Aug Grt Kfs Pl Rt Qtz
28. Liq Hbl Aug Omp Grt Kfs Pl Rt Qtz
29. Liq Aug Omp Grt Kfs Pl Rt Qtz
30. Liq Hbl Omp Grt Kfs Pl Rt Qtz
31. Liq Hbl Grt Kfs Pl Rt Qtz
32. Hbl Grt Kfs Bt Rt Qtz
33. Hbl Grt Kfs Rt Qtz

Figure 15. Pressure versus temperature pseudosection. Orange shaded area is an estimated P-T range of peak metamorphism restricted by the stability field of peak mineral assemblage and modal isopleth of melt and composition isopleth of grossular in garnet.

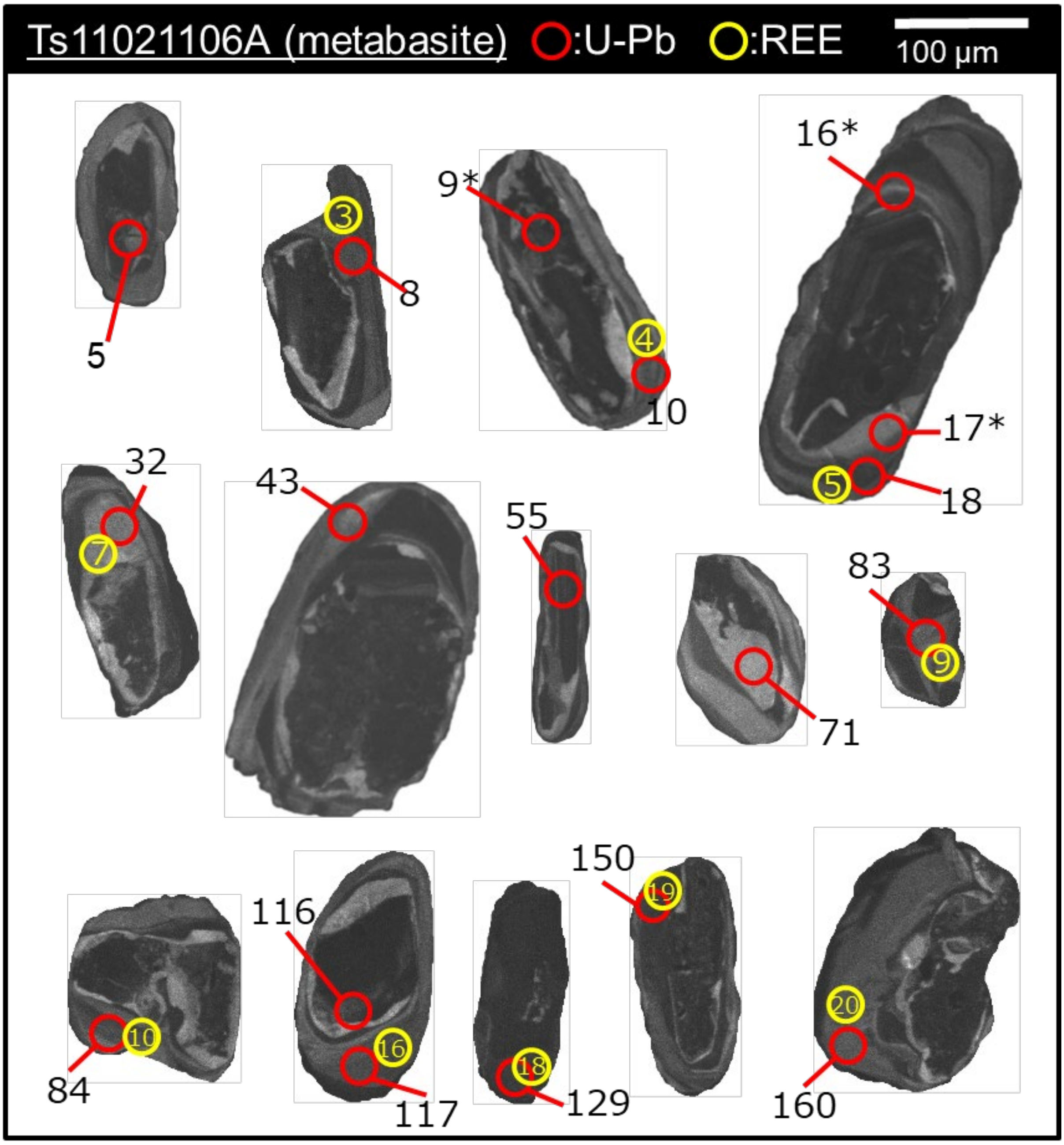

Figure 16. Cathodoluminescence (CL) images of representative zircon grains separated from sample Ts11021106A. Circles and numbers indicate the analyzed spot and its spot number, respectively. Numbers with asterisk show spot of discordant age data.

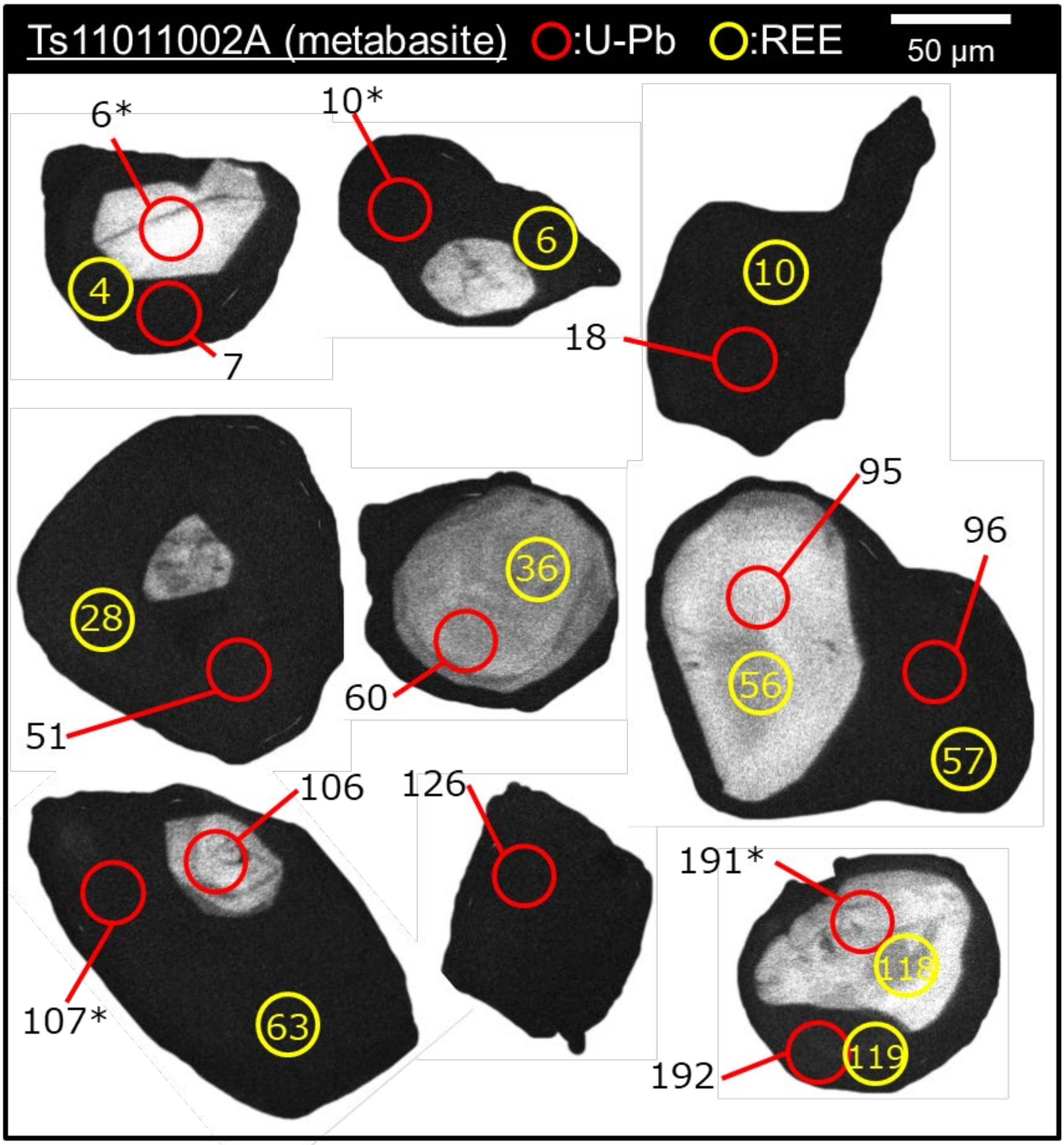

Figure 17. Cathodoluminescence (CL) images of representative zircon grains separated from sample Ts11011002A. Circles and numbers indicate the analyzed spot and its spot number, respectively. Numbers with asterisk show spot of discordant age data.

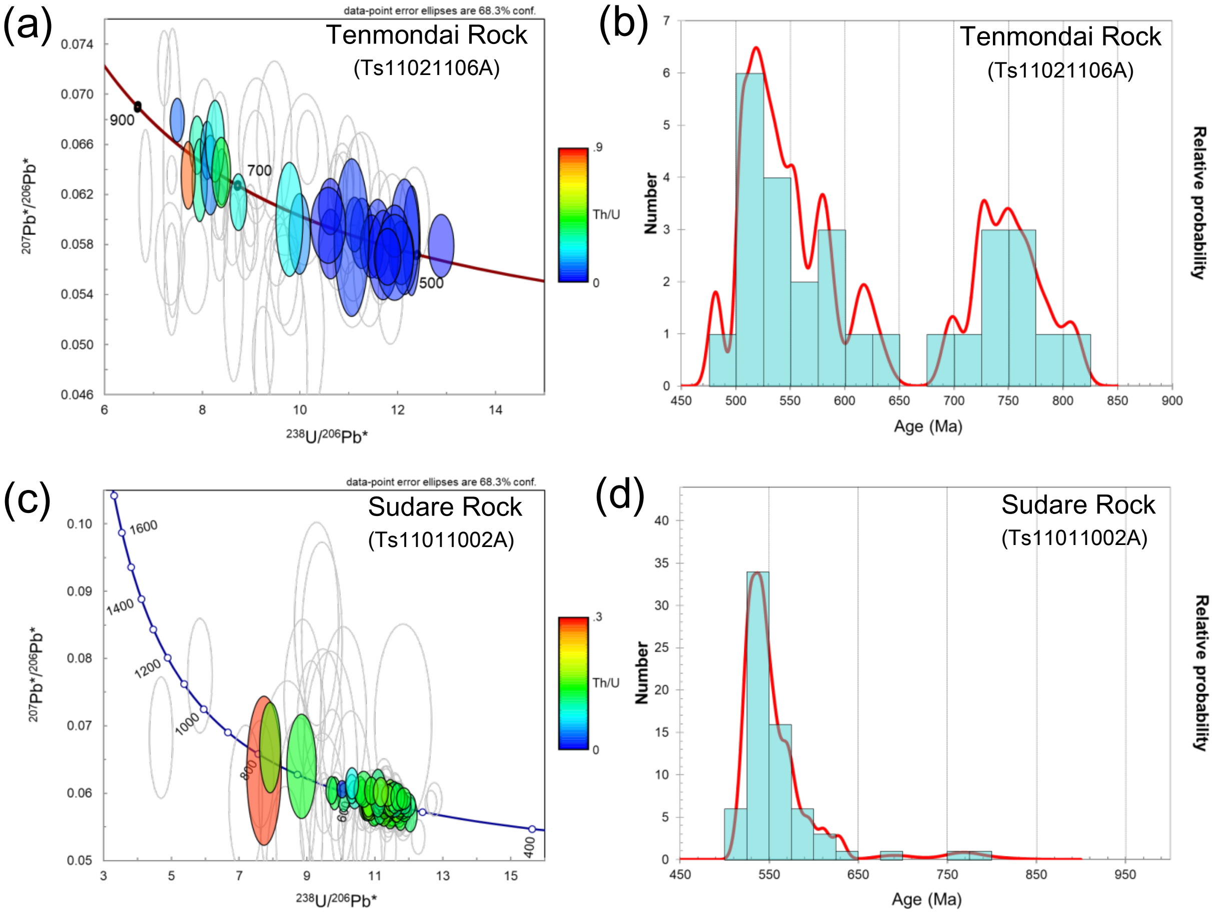

Figure 18. (a) Terra-Wasserburg concordia diagrams of sample Ts11021106A. Age ellipses are colored based on Th/U ratio. (b) Histograms with probability density plot of sample Ts11021106A. (c) Terra-Wasserburg concordia diagrams of sample Ts11011002A. Age ellipses are colored based on Th/U ratio. (d) Histograms with probability density plot of sample Ts11011002A.

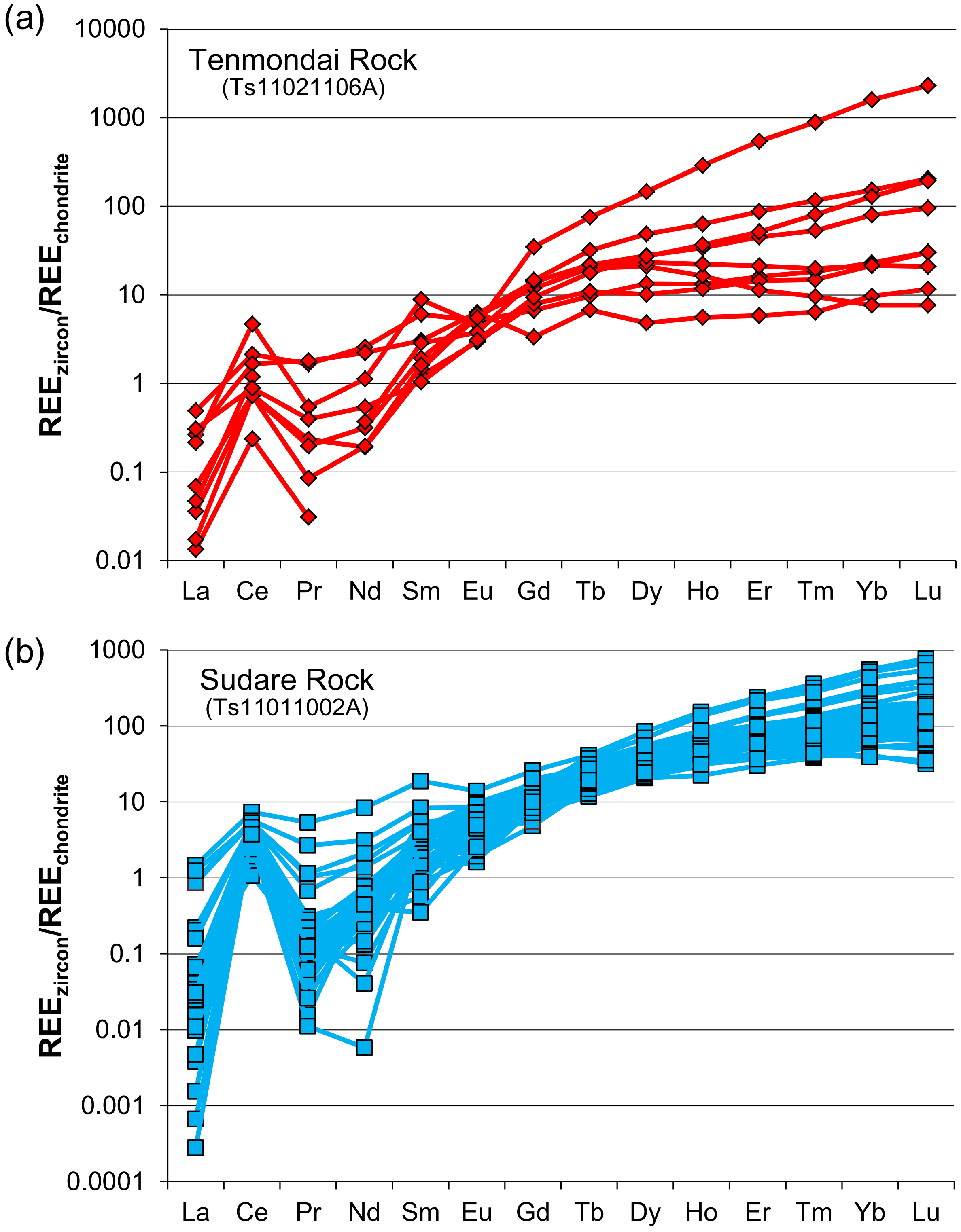

Figure 19. (a) Chondrite-normalized REE patterns for metamorphic zircon grains in sample Ts11021106A. (b) Chondrite-normalized REE patterns for metamorphic zircon grains in sample Ts11011002A. Normalized values are from McDonough and Sun (1995).

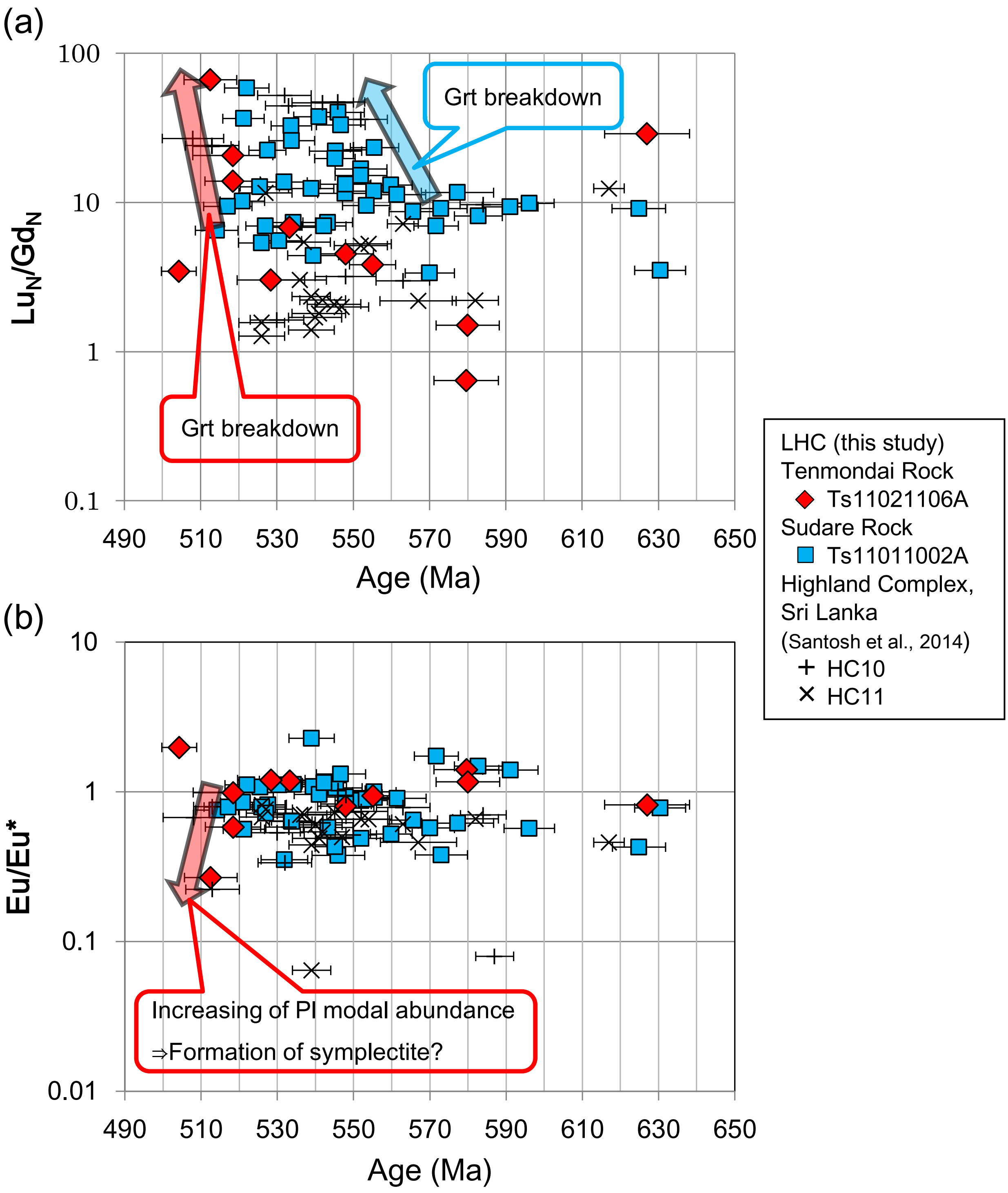

Figure 20. The plots of (a) normalized Lu/Gd and (b) Eu/Eu* (Eu*=[$\mathrm{Sm_N}$×$\mathrm{Gd_N}$]^[1/2]) values versus U-Pb age of examined metamorphic zircon. Red diamond: sample Ts11021106A (Tenmondai Rock, the LHC, this study). Blue rectangle: Sample Ts11011002A (Sudare Rock, the LHC, this study). Black cross: sample HC10 (the Highland Complex, Sri Lanka, Santosh et al., 2014). Black x mark: sample HC11 (the Highland Complex, Sri Lanka, Santosh et al., 2014).

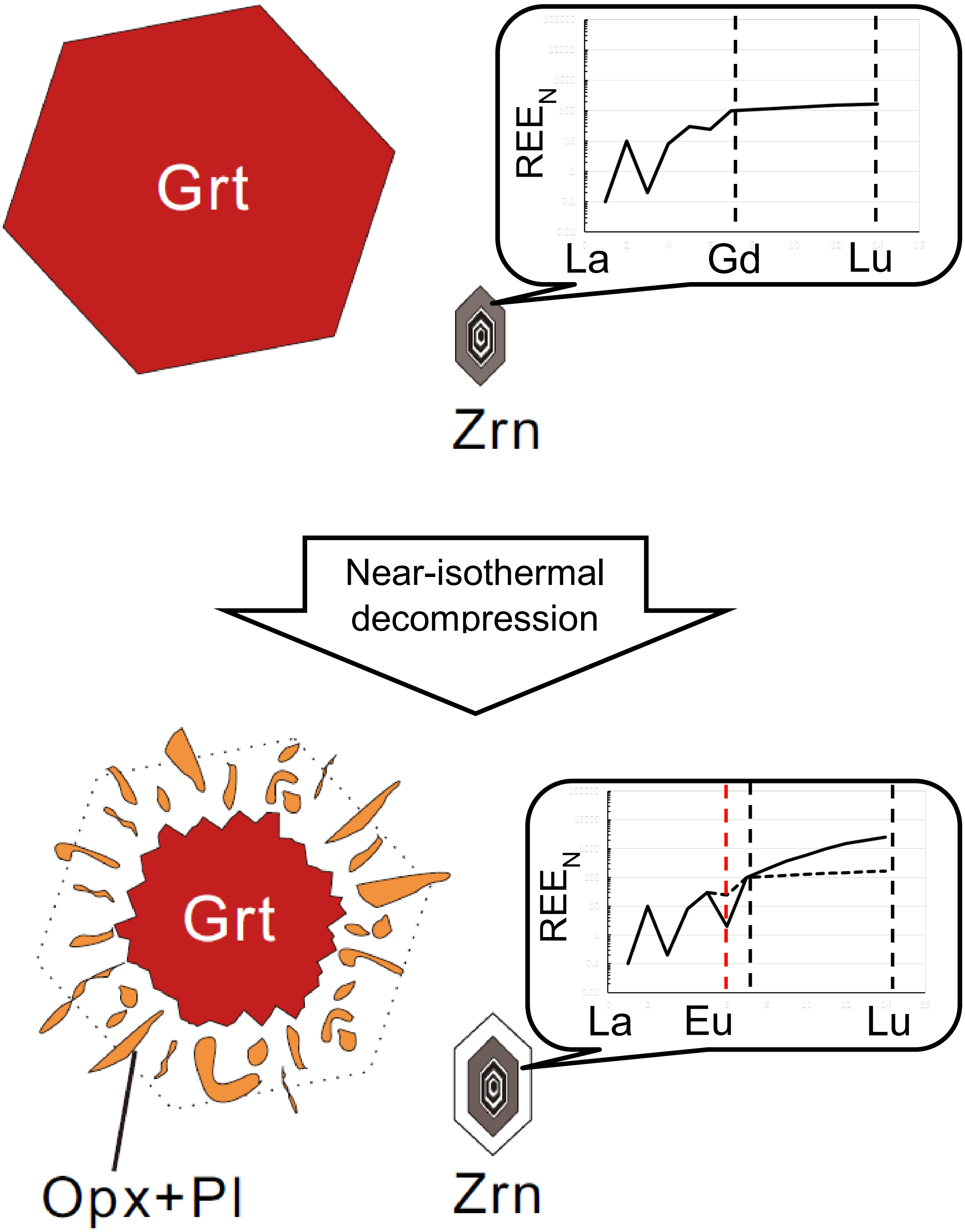

Figure 21. Schematic model showing the relationship between the formation of symplectite and change of REE patterns in metamorphic zircon.

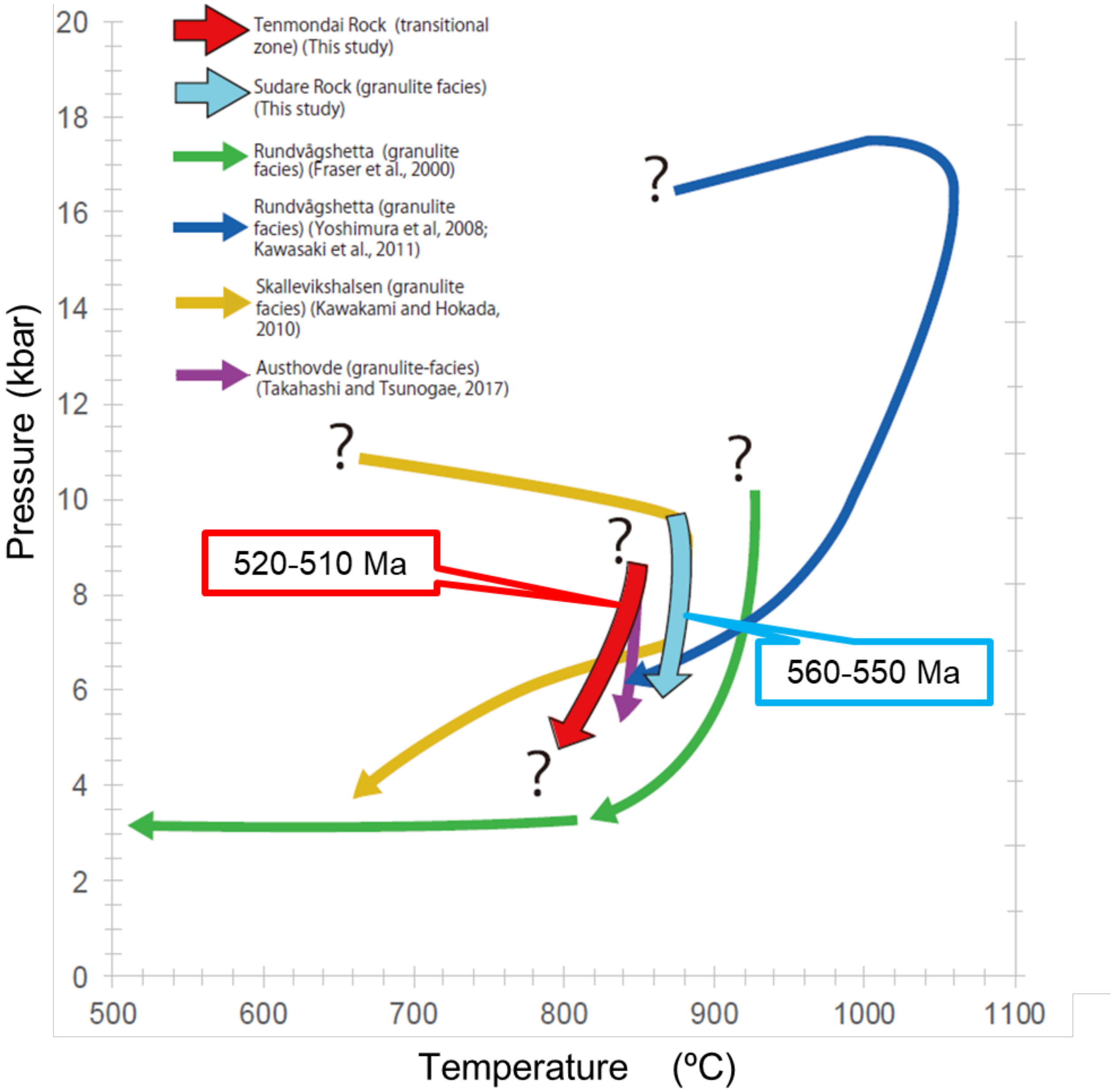

Figure 22. Summary of the *P*-*T*-*t* paths proposed from the LHC.

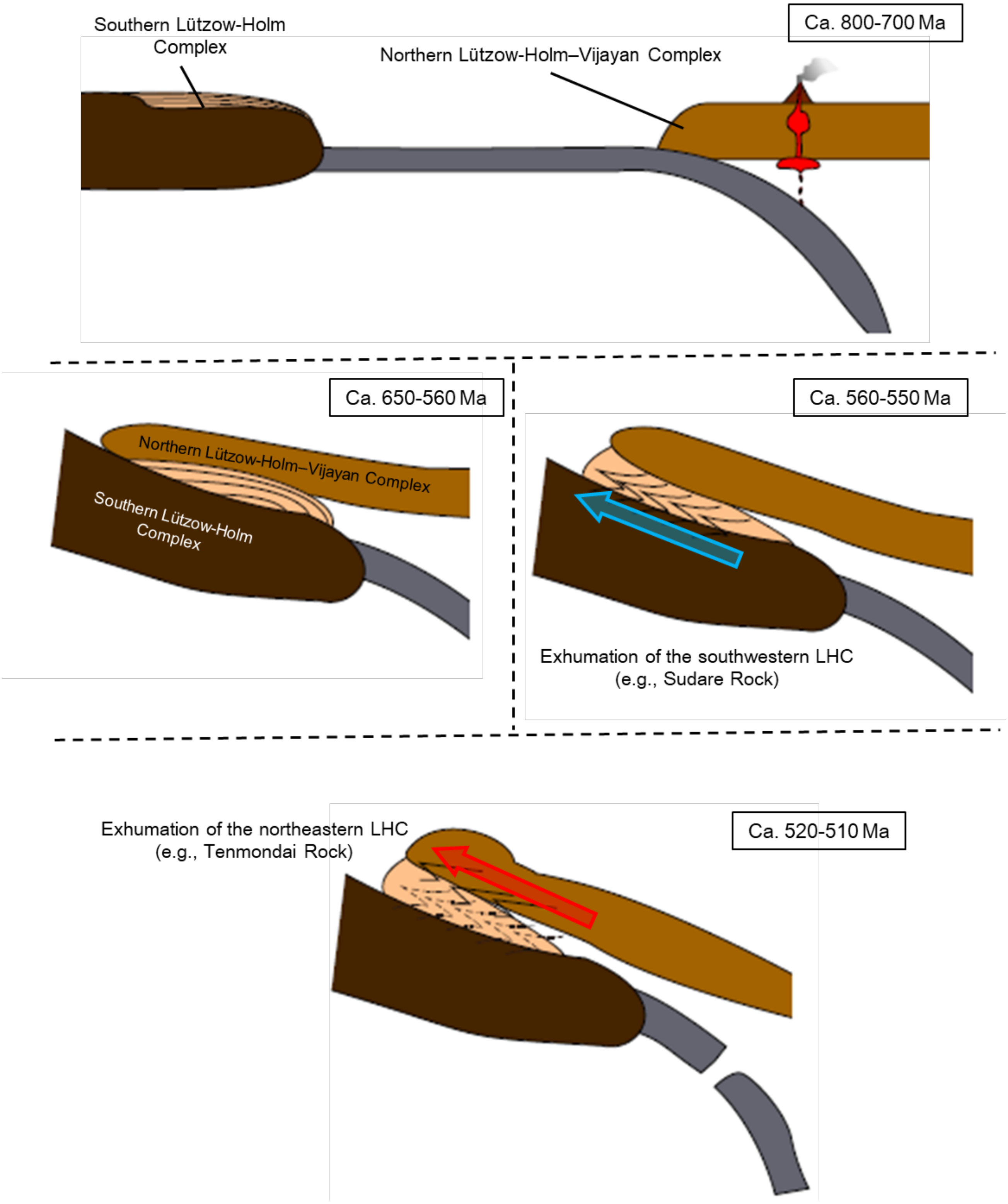

Figure 23. Schematic model showing the tectonic evolution of the LHC.

Table 1. Abbreviation of mineral name after Whitney and Evans (2010).

Mineral	abbreviations
Ap	apatite
And	andalusite
Bt	biotite
Cal	calcite
Ccp	chalcopyrite
Cpx	clinopyroxene
Fsp	feldspars
Grt	garnet
Hbl	hornblende
Ilm	ilmenite
Ky	kyanite
Mag	magnetite
Ms	Muscovite
Omp	omphasite
Opx	orthopyroxene
Pl	plagioclase
Prl	pyrophyllite
Py	pyrite
Qtz	quartz
Rt	rutile
Sil	sillimanite
Sph	sphene
Spl	spinel
Zrn	zircon

Table 2. Mineral assemblages of the samples from Tenmondai Rock and Sudare Rock.

Sample No.	Rock type	Ap	Bt	Ccp	Cpx	Grt	Hbl	Ilm	Kfs	Ky	Ms	Opx	Pl	Py	Qtz	Rt	Sil	Sph	Accessory mineral
Tenmondai Rock																			
Ts11021001A	Grt amphibolite		+			+	+++	++					+++	+	+				Ap, Zrn
Ts11021001C	amphibolite		++				+++	++					+++	+	+				Ap, Zrn
Ts11021001D	hornblende rock		++				+++	++					++						Ap, Zrn
Ts11021003A	mafic granulite		++				+++	++				+++	+++		++				Ap, Zrn
Ts11021003B	Bt-Hbl-Grt rock		+++			+++		+					++		++				Ap, Rt, Zrn
Ts11021003D	Grt-Bt gneiss		++			++		+	++				+++	+	+++	+			Ap, Zrn
Ts11021006A	ultramafic gnalulite	++	++		+++		+++	+					+						Zrn
Ts11021006B	Bt-rich gneiss		+	+			+++	+					+++	+					Ap, Cal, Zrn
Ts11021007A	pegatite								+++		+		++		+++				Zrn
Ts11021007B	Grt-Bt-Sil gneiss		++			+++		+	+				+++		+	+	++		Ap, Zrn
Ts11021007C	〃		+++			+++		+			+		+++		+++		++		Ap, Rt, Zrn
Ts11021007D	Sil-rock + Grt-Bt gneiss		++			++		+	++		+		+++	+	+++		++		Ap, Rt, Zrn
Ts11021007E	Bt-Grt rock	++	+++			++			+				++		+++				Zrn
Ts11021007F	Grt-bearing pegmatite		+			+++		+	+++		+		++	+	+++				Zrn
Ts11021007G	Grt amphibolite		+++			+++		+					+++		+++				Ap, Zrn
Ts11021007H	mafic granulite		++				+++	+				+++	+++		+				Ap, Zrn
Ts11021007I1	quartzofeldspathic gneiss		+++			++		+	+++		+		+		+++		++		Ap, Zrn
Ts11021007I2	〃		+++			++		+	+++		+		+		+++		++		Ap, Zrn
Ts11021007J	Sil quartzite		+			+		+							+++		+++		
Ts11021007K	Grt-Bt rock		++			+++		+	+++		+		+		+++	+		+	Ap, Zrn
Ts11021007L	Grt-Bt gneiss		+++			+++		+	+		+		+++	+	+++				Ap, Rt, Zrn
Ts11021007M	Grt-Bt rock		+++			+++		+			+		+++		+++				Ap, Zrn
Ts11021007N	amphibolite		++				++	+				++	+++	-	+				Zrn
Ts11021007Ō	Grt-Bt-Sil gneiss		++			++		+			+		+++		+++		++		Ap, Rt, Spl, Zrn
Ts11021007P1	Grt mafic granulite				++	+++	++	+				++	+++		++			++	Ap, Zrn
Ts11021007P2	Grt-Sil gneiss				++	+++	++	+				++	+++		++			++	Ap, Zrn
TS11021008A	Ky-bearing leucocratic rock		+	+		+		+	+++	+	+		+	+	+++	+	+		Zrn
TS11021008B	Grt-bearing leucocratic rock		+			++		+	+++	+	+	-	++	+	+++	+	++		Ap, Spl. Zrn
Ts11021106A	Grt mafic granulite		++	+		++		+				+++	+++	+	++				Ap, Rt, Zrn
TS11021106B	Grt mafic granulite		+++			+++		+			+		+++		+++				Ap, Rt, Zrn
TS11021106C	Grt-Sil-Bt gneiss		++			++		+			+		+++		+++		++		Rt, Zrn
TS11021106D	Bt-Grt gneiss	+	++			++		+	+++				+;		+++	+			Zrn
TS11021107A	Grt-Bt-Sil gneiss		++			+++		+	+++				++		+++		+++		Ap, Rt, Zrn
TS11021107B	Ky-bearing leucocratic rock		++			++		+	+++	+	+		+		+++		++		Ap, Cal, Rt, Zrn
TS11021107C	Grt-Bt gneiss		+++			++		+	++				+		+++				Ap, Zrn
TS11021108A	Ky-bearing leucocratic rock		+			+			+++	+	+		+		+++				Zrn
TS11021108B	layered Bt-Grt gneiss		+			+		+	+++	+	+		+		+++		++		Ap, Rt, Zrn
TS11021108C	layered Bt-Grt gneiss		++			++		+	+++		+		++		+++		+		Ap, Rt, Spl, Zrn
Sudare Rock																			
Ts11011002A	Grt mafic granulite		++	+	+++	+	+++	++				++	+++	+					Ap, Qtz, Zrn
TS11011002B	Grt-bearing quartzofeldspathic gneiss		++			+		+	+++				++	+	+++				Zrn
TS11011002C	Grt-Bt gneiss		++			++		+				++	+++	+	+++				Ap, Zrn

+++: abundant, ++: moderate, +: rare

Table 3. The list of the examined samples from the Lützow-Holm Complex

Sample No.	Locality	Lithology	Co-ordinates
Ts11021101A	Tenmondai Rock	Grt amphibolite	S68° 26’ 39.98”; E41° 43’ 26.075”
Ts11021103A	Tenmondai Rock	mafic granulite	S68° 26’ 31.96”; E41° 43’ 35.400”
Ts11021106B	Tenmondai Rock	Bt-rich gneiss	S68° 26’ 34.66”; E41° 42’ 54.899”
Ts11021007H	Tenmondai Rock	mafic granulite	S68° 26’ 38.04”; E41° 42’ 47.124”
Ts11021106A	Tenmondai Rock	Grt mafic granulite	S68° 26’ 41.64”; E41° 43’ 4.368”
Ts11011002A	Sudare Rock	Grt mafic granulite	S69° 42’ 39.96”; E39° 12’ 41.58”

Table 4. Representative electron microprobe analyses of garnet.

Mineral name	Garnet (O = 12)					
Skmple No.	Ts11021001A		Ts11021106A		Ts11011002A	
Remarks	core	rim	core	rim	core	rim
SiO_2	38.45	38.36	38.21	38.32	38.70	38.23
Al_2O_3	21.13	20.87	21.31	21.33	21.37	21.63
TiO_2	0.03	0.00	0.07	0.00	0.04	0.00
Cr_2O_3	0.03	0.00	0.03	0.00	0.00	0.00
FeO^*	20.80	20.25	26.82	29.38	24.94	27.48
MnO	5.95	11.61	1.24	1.54	1.28	2.33
MgO	5.81	4.98	5.49	5.87	5.18	3.80
CaO	8.07	5.16	6.75	3.82	8.79	7.30
Na_2O	0.07	0.02	0.00	0.00	0.00	0.02
K_2O	0.04	0.00	0.02	0.00	0.00	0.00
Total	100.36	101.24	99.93	100.26	100.31	100.78
Si	2.991	3.002	2.995	3.004	3.010	2.996
Al	1.937	1.924	1.968	1.971	1.959	1.997
Ti	0.002	0.000	0.004	0.000	0.002	0.000
Cr	0.002	0.000	0.002	0.000	0.000	0.000
Fe	1.353	1.325	1.757	1.926	1.621	1.800
Mn	0.392	0.769	0.082	0.102	0.084	0.154
Mg	0.673	0.580	0.641	0.685	0.600	0.443
Ca	0.672	0.433	0.566	0.321	0.732	0.612
Na	0.010	0.004	0.000	0.000	0.000	0.003
K	0.004	0.000	0.002	0.000	0.000	0.000
Total	8.036	8.037	8.017	8.010	8.008	8.005
Mg/(Fe+Mg)	0.33	0.30	0.27	0.27	0.27	0.20
Alm (mol. %)	43.79	42.64	56.97	63.10	53.37	59.81
Pyp (mol. %)	21.78	18.68	21.39	22.81	19.75	14.72
Grs (mol. %)	21.75	13.92	18.90	10.69	24.11	20.35
Sps (mol. %)	12.69	24.75	2.74	3.41	2.78	5.12

Total Fe as FeO.

Table 5. Representative electron microprobe analyses of pyroxenes.

Mineral name	Orthopyroxene (O = 6)						Clinopyroxene (O = 6)
Skmple No.	Ts11021003A	Ts11021007H	Ts11021106A		Ts11011002A		Ts11011002A
Remarks			matrix (Opx_1)	symplectite (Opx_2)	matrix (Opx_1)	symplectite (Opx_2)	
SiO_2	52.30	50.39	50.43	51.16	50.39	51.02	51.58
Al_2O_3	1.50	1.75	1.78	2.43	1.17	1.13	2.34
TiO_2	0.06	0.04	0.02	0.07	0.04	0.06	0.27
Cr_2O_3	0.00	0.00	0.01	0.08	0.00	0.00	0.06
FeO^*	23.52	23.73	27.78	26.48	31.06	30.16	13.17
MnO	0.75	0.96	0.62	0.28	0.71	0.82	0.27
MgO	21.05	19.48	19.22	19.25	16.19	16.81	11.35
CaO	0.32	0.40	0.20	0.20	0.71	0.48	20.96
Na_2O	0.05	0.03	0.03	0.00	0.02	0.00	0.39
K_2O	0.00	0.01	0.00	0.00	0.00	0.01	0.00
Total	99.54	96.77	100.08	99.95	100.29	100.49	100.39
Si	1.969	1.962	1.931	1.942	1.956	1.966	1.949
Al	0.066	0.080	0.080	0.109	0.054	0.051	0.104
Ti	0.002	0.001	0.001	0.002	0.001	0.002	0.008
Cr	0.000	0.000	0.000	0.002	0.000	0.000	0.002
Fe	0.740	0.772	0.889	0.840	1.008	0.972	0.416
Mn	0.024	0.032	0.020	0.009	0.023	0.027	0.009
Mg	1.180	1.130	1.096	1.088	0.936	0.965	0.639
Ca	0.013	0.017	0.008	0.008	0.030	0.020	0.848
Na	0.004	0.002	0.002	0.000	0.001	0.000	0.028
K	0.000	0.000	0.000	0.000	0.000	0.000	0.000
Total	3.998	3.996	4.029	4.001	4.009	4.003	4.003
Mg/(Fe+Mg)	0.61	0.594	0.58	0.56	0.48	0.50	0.61

Total Fe as FeO.

Table 6. Representative electron microprobe analyses of plagioclase.

Mineral name	Plagioclase (O = 8)										
Skmple No.	Ts11021001A	Ts11021003A		Ts11021006B	Ts11021007H		Ts11021106A			Ts11011002A	
Remarks		core	rim		core	rim	core (Pl_1)	rim (Pl_2)	symplectite (Pl_2)	matrix (Pl_1)	symplectite (Pl_2)
SiO_2	57.52	55.28	48.58	61.25	55.03	49.29	53.45	48.25	47.14	56.35	47.36
Al_2O_3	27.06	28.47	33.08	24.29	27.59	31.57	29.40	33.14	33.66	28.23	34.07
TiO_2	0.02	0.00	0.00	0.00	0.00	0.00	0.00	0.00	0.01	0.00	0.01
Cr_2O_3	0.00	0.02	0.00	0.00	0.00	0.03	0.00	0.00	0.00	0.00	0.02
FeO^*	0.14	0.12	0.12	0.15	0.16	0.20	0.09	0.21	0.24	0.11	0.28
MnO	0.00	0.00	0.01	0.02	0.00	0.00	0.00	0.04	0.03	0.00	0.00
MgO	0.02	0.01	0.02	0.00	0.00	0.00	0.00	0.01	0.01	0.00	0.00
CaO	8.84	10.69	16.14	5.67	9.81	14.48	12.46	16.57	17.28	9.92	16.42
Na_2O	6.50	6.04	2.55	9.08	6.21	3.15	4.53	2.10	1.77	5.34	1.91
K_2O	0.21	0.14	0.03	0.25	0.11	0.06	0.10	0.04	0.04	0.39	0.07
Total	100.31	100.76	100.53	100.73	98.91	98.77	100.03	100.35	100.17	100.34	100.15
Si	2.572	2.479	2.213	2.713	2.508	2.277	2.419	2.205	2.164	2.522	2.169
Al	1.426	1.504	1.776	1.268	1.481	1.718	1.568	1.784	1.821	1.489	1.838
Ti	0.001	0.000	0.000	0.000	0.000	0.000	0.000	0.000	0.000	0.000	0.000
Cr	0.000	0.001	0.000	0.000	0.000	0.001	0.000	0.000	0.000	0.000	0.001
Fe	0.005	0.004	0.005	0.006	0.006	0.008	0.003	0.008	0.009	0.004	0.011
Mn	0.000	0.000	0.000	0.001	0.000	0.000	0.000	0.002	0.001	0.000	0.000
Mg	0.001	0.001	0.001	0.000	0.000	0.000	0.000	0.001	0.001	0.000	0.000
Ca	0.423	0.513	0.788	0.269	0.479	0.717	0.604	0.811	0.849	0.476	0.805
Na	0.563	0.525	0.225	0.779	0.548	0.282	0.397	0.186	0.157	0.463	0.169
K	0.012	0.008	0.002	0.014	0.006	0.004	0.006	0.002	0.002	0.022	0.004
Total	5.003	5.035	5.010	5.050	5.028	5.007	4.998	4.997	5.005	4.976	4.997
An (mol. %)	42.42	49.08	77.66	25.33	46.33	71.53	59.98	81.19	84.19	49.51	82.28

Total Fe as FeO

Table 7. Representative electron microprobe analyses of calcic amphibole.

Mineral name	Calcic amphibole (O = 23)							
Skmple No.	Ts11021001A	Ts11021003A		Ts11021006B		Ts11021007H		Ts11011002A
Remarks		core	rim	core	rim	core	rim	
SiO_2	43.35	41.40	44.35	42.21	45.05	42.59	43.39	41.53
Al_2O_3	10.78	10.93	10.82	10.28	8.68	11.50	11.03	11.60
TiO_2	1.67	2.09	1.83	2.15	1.44	1.39	1.19	2.42
Cr_2O_3	0.07	0.10	0.09	0.05	0.00	0.03	0.00	0.01
FeO^*	14.93	13.07	13.24	15.05	14.67	13.81	13.85	17.88
MnO	1.11	0.20	0.10	0.24	0.33	0.28	0.34	0.19
MgO	11.73	12.12	12.65	11.09	12.30	11.68	12.10	9.46
CaO	10.60	11.38	11.20	11.25	11.56	10.84	10.78	11.14
Na_2O	1.69	1.34	1.16	1.86	1.39	1.37	1.06	1.40
K_2O	0.84	1.16	1.04	1.45	1.08	1.08	0.95	1.91
Total	96.76	93.79	96.50	95.64	96.50	94.57	94.69	97.54
Si	6.526	6.400	6.602	6.470	6.776	6.512	6.604	6.329
Al	1.913	1.992	1.898	1.856	1.539	2.071	1.977	2.084
Ti	0.189	0.243	0.205	0.248	0.163	0.160	0.136	0.277
Cr	0.008	0.012	0.011	0.006	0.000	0.004	0.000	0.001
Fe	1.879	1.689	1.648	1.929	1.844	1.766	1.763	2.278
Mn	0.141	0.026	0.013	0.031	0.041	0.036	0.044	0.024
Mg	2.630	2.791	2.804	2.532	2.756	2.660	2.743	2.147
Ca	1.708	1.884	1.786	1.847	1.862	1.775	1.756	1.819
Na	0.493	0.401	0.335	0.552	0.406	0.405	0.313	0.415
K	0.162	0.228	0.198	0.284	0.206	0.210	0.184	0.371
Total	15.649	15.666	15.500	15.755	15.593	15.599	15.520	15.745
Mg/(Fe+Mg)	0.58	0.62	0.63	0.57	0.60	0.60	0.61	0.49

Total Fe as FeO.

Table 8. Representative electron microprobe analyses of biotite.

Mineral name	Biotite (O = 22)										
Skmple No.	Ts11021001A		Ts11021003A		Ts11021006B		Ts11021007H		Ts11021106A		Ts11011002A
Remarks	core	rim	core	rim	core	rim	core	rim	core	rim	
SiO_2	36.22	37.24	37.17	37.72	36.64	37.40	36.81	37.86	35.98	36.31	36.20
Al_2O_3	14.75	15.57	14.32	14.91	13.81	14.37	14.10	14.46	14.43	14.66	13.72
TiO_2	2.94	4.02	3.66	2.73	4.39	3.76	3.99	2.78	3.74	4.26	5.59
Cr_2O_3	0.00	0.00	0.14	0.13	0.03	0.00	0.00	0.04	0.01	0.09	0.04
FeO^*	16.08	11.74	13.71	13.48	16.40	15.36	13.41	12.39	15.22	15.20	18.84
MnO	0.45	0.45	0.04	0.07	0.10	0.08	0.07	0.07	0.03	0.07	0.06
MgO	14.27	14.78	15.25	15.81	13.05	13.81	14.81	16.08	13.96	14.60	11.61
CaO	0.22	0.03	0.00	0.01	0.06	0.01	0.02	0.00	0.00	0.02	0.00
Na_2O	0.11	0.08	0.18	0.21	0.22	0.22	0.18	0.14	0.16	0.17	0.05
K_2O	8.13	9.61	9.67	9.52	9.44	9.38	9.31	9.50	8.60	9.51	9.92
Total	93.17	93.51	94.14	94.59	94.13	94.39	92.69	93.32	92.13	94.90	96.02
Si	5.551	5.577	5.604	5.635	5.603	5.652	5.623	5.701	5.563	5.478	5.508
Al	2.664	2.748	2.544	2.625	2.489	2.558	2.537	2.566	2.629	2.607	2.460
Ti	0.339	0.453	0.414	0.307	0.504	0.427	0.458	0.315	0.435	0.484	0.639
Cr	0.000	0.000	0.016	0.015	0.004	0.000	0.000	0.005	0.001	0.011	0.005
Fe	2.060	1.469	1.729	1.683	2.096	1.941	1.713	1.559	1.967	1.918	2.396
Mn	0.059	0.057	0.005	0.009	0.012	0.010	0.009	0.008	0.004	0.009	0.007
Mg	3.257	3.298	3.425	3.518	2.972	3.109	3.369	3.606	3.215	3.282	2.631
Ca	0.036	0.005	0.000	0.002	0.010	0.002	0.003	0.000	0.000	0.003	0.000
Na	0.032	0.022	0.054	0.061	0.066	0.064	0.052	0.041	0.049	0.050	0.014
K	1.589	1.835	1.860	1.813	1.841	1.808	1.813	1.825	1.696	1.830	1.924
Total	15.587	15.464	15.651	15.668	15.597	15.571	15.577	15.626	15.559	15.669	15.584
Mg/(Fe+Mg)	0.61	0.69	0.66	0.68	0.59	0.62	0.66	0.70	0.62	0.63	0.52

Total Fe as FeO.

Table 9. Whole-rock geochemistry of the samples.

Sample No.	Ts11021001A	Ts11021003A	Ts11021006B	Ts11021007H	Ts11021106A	Ts11011002A
SiO_2 (%)	48.46	48.4	48.6	47.99	50.06	44.72
Al_2O_3	15.19	17.44	16.38	17.7	17.31	15.98
Fe_2O_3(T)	14.68	11.22	10.23	13.25	13.94	16.29
MnO	0.577	0.184	0.155	0.194	0.209	0.209
MgO	4.82	8.45	6.06	6.76	4.91	6.11
CaO	8.62	10.06	8.4	9.09	7.4	9.44
Na_2O	3.45	1.61	3.93	1.29	0.97	2.37
K_2O	0.48	1.08	1.75	1.44	1.68	1.15
TiO_2	2.631	1.318	1.444	1.725	2.48	3.14
P_2O_5	1.05	0.24	0.32	0.24	0.67	0.42
LOI	0.45	0.7	2.68	0.99	1.15	-0.2
Total	100.4	100.7	99.95	100.7	100.8	99.629
Sc (ppm)	38	31	22	30	21	---
V	206	211	147	224	137	---
Cr	70	250	180	60	140	---
Co	30	47	38	49	45	---
Ni	50	120	100	80	100	---
Zn	180	130	100	170	190	---
Rb	2	29	38	53	111	---
Sr	371	130	672	125	148	---
Y	55	27.4	25.6	29.5	55.7	---
Zr	128	109	84	104	384	---
Nb	3.9	4.8	8.4	2.5	10.5	---
Ba	123	236	700	193	521	---
La	15.7	11.1	21.8	10.6	23	---
Ce	41.2	25.8	48.9	26.7	60.2	---
Pr	6.54	3.43	6.41	3.79	8.63	---
Nd	33.7	15	27.6	17.5	41.1	---
Sm	10.2	4.25	6.17	5.15	10.7	---
Eu	3.33	1.65	2.27	2.42	3.31	---
Gd	11.6	4.81	5.54	5.33	10.9	---
Tb	1.74	0.8	0.83	0.88	1.78	---
Dy	10.6	4.98	4.86	5.49	10.5	---
Ho	2.02	0.99	0.96	1.11	2.07	---
Er	5.47	2.95	2.81	3.24	5.73	---
Tm	0.766	0.434	0.387	0.464	0.801	---
Yb	4.79	2.82	2.44	2.97	5.16	---
Lu	0.681	0.434	0.339	0.465	0.806	---
Hf	3.5	2.8	2.4	2.8	8.4	---
Ta	0.41	0.5	0.68	0.33	0.85	---
Th	1.13	1.37	1.61	1.18	2.34	---
U	0.69	1.77	0.93	1.46	2.8	---

Table 10. Summary of the results of geothermobarometry.

Geothermobarometers	References	Ts11021106A	Ts11011002A
Geothermometer (calculated at 8 kbar) [℃]			
Grt-Opx geothermometer (℃)	Aranovich and Berman (1997)	792-826	
Grt-Cpx (diopside) geothermometer (℃)	Ellis and Green (1979)		860-891
Geobarometer (calculated at 800℃) [kbar]			
Grt-Opx-Pl-Qtz geobarometer (kbar)	Parkins and Newton (1981)	6.50-7.52	
	Moecher et al. (1988)	8.44-9.25	
Grt-Cpx-Pl-Qtz geobarometer (kbar)	Perkins and Newton (1981)		7.99-8.39
	Moecher et al. (1988)		8.51-9.21

Table 11. Zircon U-Pb data of sample Ts11021106A from Tenmondai Rock.

Spot No.	^{206}Pb$_c$^{1} (%)	U (ppm)	Th (ppm)	Th/U	^{238}U/^{206}Pb*^{1}	^{207}Pb*/^{206}Pb*^{1}	^{238}U/^{206}Pb* age^1 (Ma)	^{207}Pb*/^{206}Pb* age^1 (Ma)	Disc. (%)^2
Ts11021106A									
5	0.25	221	63	0.29	7.90 ± 0.10	0.0660 ± 0.0015	768.8 ± 9.2	806 ± 48	4.6
8	0.78	168	3	0.02	11.27 ± 0.16	0.0589 ± 0.0018	548.0 ± 7.3	564 ± 67	2.9
9	0.72	419	132	0.32	8.39 ± 0.09	0.0606 ± 0.0015	726.2 ± 7.6	626 ± 51	-16.0
10	0.17	162	3	0.02	11.12 ± 0.13	0.0596 ± 0.0014	555.1 ± 6.1	591 ± 51	6.1
16	0.76	172	5	0.03	11.65 ± 0.13	0.0609 ± 0.0019	531.0 ± 5.9	638 ± 67	16.8
17	0.48	140	3	0.02	10.88 ± 0.14	0.0621 ± 0.0022	566.6 ± 6.7	679 ± 73	16.6
18	5.31	333	8	0.02	12.29 ± 0.12	0.0583 ± 0.0029	504.3 ± 4.6	542 ± 105	7.0
19	0.02	1890	69	0.04	9.71 ± 0.17	0.0580 ± 0.0005	631.8 ± 10.6	529 ± 20	-19.4
20	0.36	179	68	0.39	8.61 ± 0.12	0.0595 ± 0.0021	708.0 ± 9.4	586 ± 74	-20.8
22	0.44	176	18	0.11	10.00 ± 0.14	0.0589 ± 0.0021	614.5 ± 8.4	563 ± 77	-9.1
27	0.00	316	4	0.01	10.78 ± 0.15	0.0562 ± 0.0012	572.1 ± 7.4	460 ± 46	-24.4
31	0.00	113	34	0.31	7.22 ± 0.08	0.0721 ± 0.0020	836.4 ± 8.9	989 ± 55	15.4
32	0.04	112	1	0.01	10.63 ± 0.16	0.0581 ± 0.0018	579.6 ± 8.5	533 ± 68	-8.7
39	3.15	77	5	0.07	10.97 ± 0.17	0.0620 ± 0.0042	562.4 ± 8.6	674 ± 138	16.6
41	1.07	321	193	0.62	8.87 ± 0.13	0.0586 ± 0.0022	688.4 ± 9.6	553 ± 82	-24.5
43	3.35	151	4	0.03	12.15 ± 0.20	0.0586 ± 0.0031	509.9 ± 8.0	555 ± 110	8.1
44	1.37	358	312	0.89	7.37 ± 0.10	0.0552 ± 0.0030	820.0 ± 10.2	422 ± 115	-94.3
50	0.04	57	3	0.06	7.34 ± 0.19	0.0573 ± 0.0027	823.6 ± 20.4	502 ± 101	-64.1
51	0.79	1348	266	0.20	7.37 ± 0.06	0.0636 ± 0.0010	819.9 ± 6.8	728 ± 33	-12.6
53	0.00	394	28	0.07	7.49 ± 0.09	0.0680 ± 0.0012	808.2 ± 9.5	868 ± 35	6.9
55	0.31	309	47	0.16	8.40 ± 0.09	0.0634 ± 0.0015	724.8 ± 7.0	723 ± 50	-0.3
59	0.77	300	26	0.09	11.10 ± 0.13	0.0545 ± 0.0014	556.3 ± 6.3	392 ± 57	-41.9
60	0.86	404	114	0.29	8.98 ± 0.10	0.0603 ± 0.0016	680.5 ± 7.0	616 ± 57	-10.5
61	0.34	205	60	0.30	7.95 ± 0.10	0.0632 ± 0.0022	763.8 ± 9.4	715 ± 71	-6.8
62	2.68	315	130	0.42	8.35 ± 0.10	0.0591 ± 0.0026	728.8 ± 8.7	571 ± 95	-27.6
63	1.60	76	1	0.02	7.85 ± 0.18	0.0564 ± 0.0026	772.8 ± 16.7	467 ± 98	-65.5
66	1.04	232	183	0.81	6.84 ± 0.09	0.0619 ± 0.0035	880.0 ± 10.4	671 ± 117	-31.2
71	0.64	402	57	0.15	8.10 ± 0.09	0.0655 ± 0.0015	750.3 ± 7.9	793 ± 48	5.4
72	0.00	169	3	0.02	10.76 ± 0.13	0.0622 ± 0.0020	572.9 ± 6.5	682 ± 67	16.0
76	0.33	87	17	0.20	9.10 ± 0.18	0.0642 ± 0.0030	672.4 ± 12.6	749 ± 95	10.2
77	0.81	368	205	0.57	8.99 ± 0.10	0.0589 ± 0.0020	680.1 ± 7.1	566 ± 72	-20.2
81	1.74	104	3	0.03	11.20 ± 0.16	0.0619 ± 0.0033	551.4 ± 7.4	671 ± 110	17.8
83	0.00	136	3	0.02	11.59 ± 0.18	0.0585 ± 0.0021	533.3 ± 8.0	548 ± 77	2.7
84	0.00	195	2	0.01	12.08 ± 0.17	0.0574 ± 0.0017	512.5 ± 6.9	506 ± 63	-1.3
85	0.65	15	1	0.07	9.90 ± 0.40	0.0512 ± 0.0062	620.6 ± 23.6	250 ± 257	-148.3
86	0.15	70	1	0.02	11.26 ± 0.25	0.0623 ± 0.0031	548.6 ± 11.5	686 ± 102	20.0
87	0.86	177	432	2.50	7.39 ± 0.12	0.0637 ± 0.0076	818.2 ± 12.9	733 ± 235	-11.6
88	1.59	332	171	0.53	9.24 ± 0.14	0.0492 ± 0.0025	662.4 ± 9.5	160 ± 115	-314.0
93	0.80	249	28	0.11	10.15 ± 0.14	0.0658 ± 0.0019	605.5 ± 8.2	800 ± 60	24.3
94	1.93	20	4	0.20	9.61 ± 0.36	0.0482 ± 0.0076	638.2 ± 22.6	109 ± 334	-485.5
96	0.08	267	3	0.01	12.90 ± 0.17	0.0579 ± 0.0017	481.4 ± 6.2	527 ± 62	8.7
98	0.09	157	3	0.02	11.09 ± 0.17	0.0565 ± 0.0020	556.7 ± 8.3	474 ± 77	-17.5
99	0.75	386	66	0.18	8.32 ± 0.10	0.0607 ± 0.0015	731.3 ± 8.1	630 ± 53	-16.1
103	0.07	278	2	0.01	11.47 ± 0.15	0.0579 ± 0.0017	538.9 ± 7.0	525 ± 63	-2.6
104	0.00	137	13	0.10	8.16 ± 0.13	0.0636 ± 0.0021	745.0 ± 10.9	729 ± 68	-2.2
105	0.01	172	4	0.03	10.86 ± 0.16	0.0630 ± 0.0020	567.7 ± 7.9	709 ± 67	19.9
106	1.88	150	33	0.22	9.79 ± 0.18	0.0600 ± 0.0030	627.0 ± 11.1	605 ± 105	-3.6
108	1.76	193	2	0.01	11.85 ± 0.17	0.0540 ± 0.0026	522.3 ± 7.0	371 ± 105	-40.8
110	0.00	101	20	0.20	12.34 ± 0.20	0.0603 ± 0.0026	502.3 ± 7.9	614 ± 90	18.2
116	1.57	1118	918	0.84	7.72 ± 0.09	0.0635 ± 0.0018	785.5 ± 9.0	727 ± 59	-8.0
117	0.00	126	2	0.02	11.71 ± 0.20	0.0572 ± 0.0024	528.4 ± 8.9	500 ± 88	-5.7
118	1.59	74	3	0.04	11.06 ± 0.23	0.0586 ± 0.0042	557.8 ± 11.3	552 ± 148	-1.1
119	1.46	216	194	0.92	8.64 ± 0.13	0.0546 ± 0.0050	706.0 ± 10.3	395 ± 192	-78.7
121	0.05	191	4	0.02	11.65 ± 0.16	0.0565 ± 0.0021	530.9 ± 7.1	472 ± 82	-12.5
125	0.00	152	36	0.24	8.26 ± 0.13	0.0663 ± 0.0022	736.5 ± 10.9	815 ± 67	9.6
127	0.83	608	143	0.24	8.74 ± 0.11	0.0614 ± 0.0015	698.1 ± 8.6	654 ± 51	-6.8
129	0.00	309	2	0.01	10.62 ± 0.16	0.0610 ± 0.0015	580.0 ± 8.3	641 ± 52	9.5
137	0.03	237	65	0.28	8.36 ± 0.11	0.0670 ± 0.0021	728.2 ± 9.4	837 ± 65	13.0
138	0.01	42	4	0.1	9.47 ± 0.24	0.0663 ± 0.0042	646.9 ± 15.3	817 ± 127	20.8
141	0.02	57	2	0.04	11.07 ± 0.25	0.0565 ± 0.0034	557.6 ± 12.2	474 ± 127	-17.6
142	0.65	105	5	0.05	11.42 ± 0.21	0.0563 ± 0.0032	541.2 ± 9.7	465 ± 121	-16.4

Table 11. (continued)

Spot No.	$^{206}Pb_c$ [1] (%)	U (ppm)	Th (ppm)	Th/U	$^{238}U/^{206}Pb^*$ [1]	$^{207}Pb^*/^{206}Pb^*$ [1]	$^{238}U/^{206}Pb^*$ age [1] (Ma)	$^{207}Pb^*/^{206}Pb^*$ age [1] (Ma)	Disc. (%) [2]
143	0.00	34	2	0.07	10.10 ± 0.32	0.0632 ± 0.0045	608.4 ± 18.4	716 ± 145	15.0
148	1.18	153	1	0.01	11.89 ± 0.21	0.0597 ± 0.0026	520.6 ± 8.7	595 ± 90	12.5
149	0.00	71	3	0.05	8.04 ± 0.16	0.0672 ± 0.0027	755.4 ± 13.9	844 ± 81	10.5
150	0.05	387	7	0.02	11.94 ± 0.17	0.0591 ± 0.0014	518.4 ± 7.3	572 ± 50	9.4
151	0.00	64	19	0.31	9.11 ± 0.24	0.0661 ± 0.0034	671.4 ± 16.9	809 ± 106	17.0
152	1.09	654	152	0.24	9.52 ± 0.16	0.0576 ± 0.0019	643.7 ± 10.3	513 ± 71	-25.5
154	1.22	449	135	0.31	9.80 ± 0.17	0.0538 ± 0.0020	626.1 ± 10.2	364 ± 82	-72.0
159	0.10	270	6	0.02	10.58 ± 0.23	0.0596 ± 0.0020	582.2 ± 12.4	588 ± 72	1.0
160	0.00	165	5	0.03	11.94 ± 0.25	0.0570 ± 0.0023	518.4 ± 10.5	493 ± 85	-5.2
162	0.33	476	181	0.39	8.39 ± 0.13	0.0638 ± 0.0019	725.8 ± 10.3	735 ± 60	1.3
164	0.65	95	14	0.15	9.67 ± 0.19	0.0563 ± 0.0031	634.3 ± 11.7	466 ± 119	-36.1
165	0.00	289	3	0.01	11.80 ± 0.18	0.0570 ± 0.0015	524.5 ± 7.6	493 ± 57	-6.4

Errors are 1-sigma; Pb_c and Pb* indicates the common and radiogenic portions, respectively.

[1] Common Pb corrected by assuming $^{206}Pb/^{238}U$–$^{208}Pb/^{232}Th$ age-concordance.

[2] The degree of discordance for an analyzed spot indicates the chronological difference between the two ages determined by Pb–Pb and U–Pb methods, and is defined as {1-($^{238}U/^{206}Pb^*$ age)/($^{207}Pb^*/^{206}Pb^*$ age)}×100 (%) (e.g., Song et al., 1996).

Table 12. Zircon U-Pb data of sample Ts11011002A from Sudare Rock.

Spot No.	^{206}Pb$_c$^{1} (%)	U (ppm)	Th (ppm)	Th/U	^{238}U/^{206}Pb*^{1}	^{207}Pb*/^{206}Pb*^{1}	^{238}U/^{206}Pb* age^1 (Ma)	^{207}Pb*/^{206}Pb* age^1 (Ma)	Disc. (%) ^{2}
Ts11011002A									
5	0.08	853	113	0.14	11.11 ± 0.12	0.0588 ± 0.0012	555.4 ± 5.7	561 ± 45	1.0
6	0.00	20	9	0.45	11.82 ± 0.55	0.0703 ± 0.0098	523.3 ± 23.5	938 ± 262	44.2
7	0.00	697	90	0.13	10.78 ± 0.11	0.0582 ± 0.0011	571.7 ± 5.8	539 ± 40	-6.1
8	0.00	26	14	0.55	11.03 ± 0.39	0.0521 ± 0.0073	559.2 ± 18.7	288 ± 294	-94.2
10	0.23	631	103	0.17	11.71 ± 0.13	0.0561 ± 0.0017	528.2 ± 5.5	458 ± 64	-15.3
11	0.00	1002	134	0.14	11.77 ± 0.12	0.0585 ± 0.0011	525.5 ± 5.1	550 ± 38	4.5
15	0.00	517	74	0.15	11.09 ± 0.12	0.0606 ± 0.0015	556.8 ± 5.7	625 ± 52	10.9
16	0.00	1630	186	0.12	11.73 ± 0.11	0.0570 ± 0.0010	527.5 ± 4.8	493 ± 36	-7.0
17	0.18	49	5	0.11	10.81 ± 0.32	0.0532 ± 0.0056	570.3 ± 16.0	340 ± 221	-67.7
18	0.04	752	72	0.10	10.32 ± 0.12	0.0607 ± 0.0014	596.1 ± 6.6	629 ± 50	5.2
18	0.00	540	67	0.13	12.74 ± 0.15	0.0591 ± 0.0016	487.0 ± 5.4	571 ± 59	14.7
20	0.00	688	89	0.13	10.64 ± 0.11	0.0602 ± 0.0013	579.3 ± 5.6	610 ± 46	5.0
21	0.21	21	3	0.16	10.29 ± 0.40	0.0583 ± 0.0092	598.1 ± 22.2	541 ± 312	-10.6
22	0.05	667	58	0.09	11.02 ± 0.11	0.0576 ± 0.0015	559.9 ± 5.5	516 ± 56	-8.5
28	0.07	593	71	0.12	9.73 ± 0.11	0.0605 ± 0.0014	630.4 ± 6.7	621 ± 49	-1.5
29	0.00	719	65	0.09	10.41 ± 0.13	0.0598 ± 0.0014	591.1 ± 7.3	598 ± 49	1.2
30	0.02	980	123	0.13	11.41 ± 0.10	0.0578 ± 0.0013	541.5 ± 4.6	521 ± 50	-3.9
31	0.01	1318	155	0.12	11.33 ± 0.11	0.0580 ± 0.0011	545.2 ± 5.3	530 ± 40	-2.9
32	0.07	689	115	0.17	11.18 ± 0.14	0.0576 ± 0.0015	552.0 ± 6.8	514 ± 56	-7.4
33	0.04	628	56	0.09	11.16 ± 0.13	0.0598 ± 0.0015	553.4 ± 6.2	597 ± 53	7.3
38	0.31	857	119	0.14	11.35 ± 0.12	0.0550 ± 0.0014	544.5 ± 5.4	411 ± 57	-32.5
39	0.00	38	6	0.15	7.62 ± 0.27	0.0628 ± 0.0053	795.3 ± 26.0	703 ± 169	-13.1
40	0.00	846	111	0.13	10.57 ± 0.12	0.0605 ± 0.0014	582.8 ± 6.3	622 ± 48	6.3
41	0.11	893	93	0.11	11.40 ± 0.12	0.0555 ± 0.0013	542.2 ± 5.6	433 ± 52	-25.2
43	0.00	1240	124	0.10	11.87 ± 0.13	0.0584 ± 0.0010	521.3 ± 5.4	546 ± 35	4.5
44	0.00	522	78	0.15	10.82 ± 0.12	0.0588 ± 0.0015	569.9 ± 6.2	562 ± 56	-1.4
49	0.02	837	90	0.11	10.10 ± 0.12	0.0594 ± 0.0014	608.9 ± 6.7	582 ± 50	-4.6
50	0.00	681	87	0.13	11.71 ± 0.12	0.0597 ± 0.0014	528.4 ± 5.3	594 ± 49	11.0
51	0.00	481	76	0.16	10.82 ± 0.13	0.0584 ± 0.0015	570.1 ± 6.4	544 ± 54	-4.8
52	0.00	670	102	0.16	11.48 ± 0.15	0.0599 ± 0.0015	538.5 ± 6.9	601 ± 54	10.4
53	0.17	159	13	0.08	9.50 ± 0.17	0.0586 ± 0.0030	645.4 ± 10.8	552 ± 107	-16.9
54	0.00	884	99	0.11	11.32 ± 0.14	0.0613 ± 0.0016	545.5 ± 6.5	650 ± 54	16.1
55	0.00	792	106	0.14	11.57 ± 0.13	0.0584 ± 0.0013	534.3 ± 5.8	547 ± 48	2.3
59	0.00	743	121	0.17	11.19 ± 0.14	0.0602 ± 0.0014	552.0 ± 6.8	612 ± 51	9.8
60	0.00	52	7	0.13	8.85 ± 0.29	0.0640 ± 0.0051	690.1 ± 21.3	744 ± 160	7.3
61	0.00	699	112	0.16	11.59 ± 0.12	0.0608 ± 0.0015	533.3 ± 5.2	632 ± 52	15.6
62	0.00	876	110	0.13	11.88 ± 0.14	0.0576 ± 0.0012	520.9 ± 5.8	515 ± 45	-1.2
63	0.00	725	101	0.14	11.39 ± 0.13	0.0590 ± 0.0014	542.6 ± 6.2	568 ± 50	4.5
64	0.00	857	117	0.14	11.54 ± 0.15	0.0589 ± 0.0013	535.7 ± 6.6	563 ± 49	4.9
65	0.02	555	73	0.13	10.99 ± 0.15	0.0578 ± 0.0018	561.5 ± 7.6	524 ± 65	-7.2
66	0.00	27	7	0.28	4.70 ± 0.23	0.0683 ± 0.0059	1243.9 ± 54.6	877 ± 171	-41.8
72	0.00	749	102	0.14	11.74 ± 0.12	0.0580 ± 0.0012	527.0 ± 5.2	532 ± 46	0.9
73	0.00	658	99	0.15	11.39 ± 0.15	0.0602 ± 0.0014	542.7 ± 6.8	612 ± 51	11.3
74	0.01	969	105	0.11	11.60 ± 0.15	0.0597 ± 0.0013	532.9 ± 6.6	595 ± 46	10.4
75	0.00	1054	140	0.14	11.72 ± 0.13	0.0567 ± 0.0012	528.0 ± 5.8	482 ± 45	-9.5
76	0.06	489	51	0.11	11.16 ± 0.14	0.0584 ± 0.0019	553.4 ± 6.5	545 ± 71	-1.6
77	0.00	70	11	0.16	9.74 ± 0.24	0.0655 ± 0.0046	630.3 ± 14.7	792 ± 140	20.4
82	0.00	1282	154	0.12	11.61 ± 0.13	0.0587 ± 0.0011	532.7 ± 5.7	555 ± 40	4.0
83	0.00	788	109	0.14	11.37 ± 0.15	0.0562 ± 0.0013	543.5 ± 6.7	460 ± 51	-18.2
84	0.00	656	48	0.08	10.34 ± 0.13	0.0615 ± 0.0015	595.3 ± 6.9	657 ± 53	9.4
85	0.00	1440	183	0.13	11.85 ± 0.14	0.0592 ± 0.0011	522.1 ± 5.9	577 ± 39	9.5
86	0.06	705	107	0.16	11.47 ± 0.14	0.0593 ± 0.0018	538.9 ± 6.4	580 ± 65	7.1
87	0.00	964	133	0.14	10.90 ± 0.13	0.0604 ± 0.0014	565.7 ± 6.3	618 ± 48	8.5
88	0.00	1078	112	0.11	11.92 ± 0.14	0.0557 ± 0.0014	519.4 ± 5.9	441 ± 53	-17.8
93	0.19	331	35	0.11	11.11 ± 0.16	0.0600 ± 0.0023	555.8 ± 7.7	605 ± 83	8.1
94	0.07	567	52	0.09	11.14 ± 0.13	0.0609 ± 0.0017	554.0 ± 6.3	635 ± 59	12.8
95	0.00	22	6	0.29	7.74 ± 0.34	0.0634 ± 0.0073	783.3 ± 32.1	722 ± 228	-8.5
96	0.00	679	98	0.15	11.37 ± 0.14	0.0586 ± 0.0013	543.3 ± 6.5	552 ± 49	1.6
97	0.08	504	64	0.13	11.76 ± 0.14	0.0575 ± 0.0019	526.0 ± 6.0	510 ± 73	-3.1
98	0.05	615	98	0.16	11.61 ± 0.13	0.0601 ± 0.0018	532.5 ± 5.8	607 ± 63	12.3
99	0.00	705	78	0.11	11.58 ± 0.14	0.0594 ± 0.0016	533.9 ± 6.0	583 ± 56	8.4
103	0.01	818	86	0.11	10.80 ± 0.13	0.0582 ± 0.0015	570.6 ± 6.6	537 ± 57	-6.3
104	0.00	35	8	0.23	5.84 ± 0.24	0.0775 ± 0.0056	1018.3 ± 38.4	1134 ± 138	10.2
106	0.12	67	10	0.15	7.92 ± 0.20	0.0668 ± 0.0045	766.1 ± 18.4	832 ± 133	7.9
107	0.00	628	73	0.12	10.89 ± 0.13	0.0616 ± 0.0012	566.2 ± 6.2	662 ± 41	14.5
108	0.01	850	161	0.19	11.29 ± 0.14	0.0612 ± 0.0018	546.9 ± 6.5	647 ± 64	15.5
109	0.00	781	109	0.14	11.63 ± 0.14	0.0578 ± 0.0014	531.9 ± 6.1	524 ± 52	-1.5
110	0.00	1808	8	0.00	10.04 ± 0.10	0.0606 ± 0.0009	611.9 ± 5.8	627 ± 30	2.4
115	0.00	568	95	0.17	10.87 ± 0.13	0.0582 ± 0.0014	567.4 ± 6.4	537 ± 53	-5.7
116	0.09	1454	178	0.13	11.31 ± 0.12	0.0568 ± 0.0011	545.9 ± 5.7	485 ± 42	-12.6
118	0.00	524	86	0.17	11.12 ± 0.17	0.0569 ± 0.0014	555.3 ± 8.4	488 ± 55	-13.8
119	0.00	775	104	0.14	11.74 ± 0.17	0.0563 ± 0.0014	527.2 ± 7.2	463 ± 56	-13.9
120	0.00	1428	170	0.12	11.82 ± 0.15	0.0578 ± 0.0011	523.5 ± 6.3	521 ± 40	-0.5
121	0.00	11	5	0.45	8.41 ± 0.55	0.0597 ± 0.0112	723.9 ± 44.9	592 ± 364	-22.3
125	0.04	120	5	0.04	9.85 ± 0.21	0.0581 ± 0.0033	623.5 ± 12.5	533 ± 121	-17.0

Table 12. (continued)

Spot No.	$^{206}Pb_c$ [1] (%)	U (ppm)	Th (ppm)	Th/U	$^{238}U/^{206}Pb^{*1}$	$^{207}Pb^{*}/^{206}Pb^{*1}$	$^{238}U/^{206}Pb^{*}$ age[1] (Ma)	$^{207}Pb^{*}/^{206}Pb^{*}$ age[1] (Ma)	Disc. (%) [2]
126	0.05	1008	124	0.13	11.68 ± 0.14	0.0595 ± 0.0014	529.4 ± 6.0	585 ± 49	9.5
128	0.00	96	13	0.14	10.32 ± 0.26	0.0540 ± 0.0036	596.3 ± 14.5	371 ± 144	-60.7
129	0.00	974	128	0.13	11.76 ± 0.14	0.0583 ± 0.0012	526.1 ± 5.8	540 ± 44	2.6
131	0.00	934	117	0.13	11.31 ± 0.15	0.0578 ± 0.0012	546.0 ± 6.9	521 ± 45	-4.8
132	0.00	769	122	0.16	11.11 ± 0.13	0.0580 ± 0.0012	555.6 ± 6.3	530 ± 45	-4.8
137	0.08	906	101	0.11	11.65 ± 0.13	0.0566 ± 0.0015	530.9 ± 5.8	478 ± 59	-11.1
138	0.05	775	107	0.14	11.46 ± 0.15	0.0572 ± 0.0016	539.5 ± 6.6	500 ± 61	-7.9
139	0.01	683	83	0.12	10.18 ± 0.12	0.0584 ± 0.0017	604.3 ± 7.0	547 ± 63	-10.5
140	0.00	472	38	0.08	10.62 ± 0.14	0.0571 ± 0.0017	580.1 ± 7.5	497 ± 64	-16.7
141	0.01	656	95	0.15	11.30 ± 0.14	0.0587 ± 0.0017	546.7 ± 6.4	557 ± 61	1.9
142	0.00	1060	125	0.12	11.58 ± 0.12	0.0576 ± 0.0010	533.8 ± 5.3	514 ± 39	-3.9
147	0.00	947	102	0.11	11.97 ± 0.15	0.0583 ± 0.0012	517.1 ± 6.3	541 ± 43	4.4
148	0.81	492	36	0.07	11.26 ± 0.16	0.0623 ± 0.0018	548.5 ± 7.3	687 ± 61	20.2
149	0.00	1519	152	0.10	11.51 ± 0.13	0.0601 ± 0.0010	537.3 ± 5.9	607 ± 35	11.5
150	0.00	665	98	0.15	10.76 ± 0.13	0.0580 ± 0.0013	573.0 ± 6.8	532 ± 50	-7.7
151	0.00	536	77	0.15	11.83 ± 0.16	0.0554 ± 0.0016	523.2 ± 6.8	429 ± 63	-22.0
152	0.00	628	83	0.14	11.35 ± 0.14	0.0617 ± 0.0016	544.3 ± 6.6	663 ± 54	17.9
153	0.00	27	1	0.06	8.87 ± 0.36	0.0743 ± 0.0076	688.4 ± 26.6	1050 ± 194	34.4
154	0.00	1005	129	0.13	11.52 ± 0.14	0.0582 ± 0.0012	536.5 ± 6.1	537 ± 45	0.1
159	0.00	19	3	0.17	9.28 ± 0.43	0.0852 ± 0.0100	659.8 ± 29.1	1320 ± 212	50.0
160	0.00	1114	137	0.13	11.04 ± 0.13	0.0574 ± 0.0012	559.0 ± 6.1	508 ± 43	-10.0
161	0.00	716	83	0.12	11.26 ± 0.13	0.0605 ± 0.0014	548.3 ± 6.3	621 ± 51	11.7
163	0.00	552	98	0.18	11.50 ± 0.15	0.0568 ± 0.0017	537.4 ± 6.8	486 ± 64	-10.6
164	0.00	424	52	0.13	10.67 ± 0.18	0.0606 ± 0.0018	577.3 ± 9.4	626 ± 62	7.8
169	0.00	905	108	0.12	11.56 ± 0.14	0.0569 ± 0.0012	535.0 ± 6.3	489 ± 45	-9.4
170	0.00	45	4	0.09	9.12 ± 0.27	0.0708 ± 0.0059	670.9 ± 18.5	951 ± 162	29.5
172	0.00	720	115	0.16	11.33 ± 0.15	0.0579 ± 0.0014	545.3 ± 6.8	528 ± 51	-3.3
173	0.16	711	104	0.15	11.73 ± 0.15	0.0563 ± 0.0017	527.4 ± 6.7	466 ± 63	-13.2
174	0.00	1013	149	0.15	11.47 ± 0.13	0.0569 ± 0.0012	539.0 ± 5.9	490 ± 46	-10.0
175	0.00	27	9	0.32	9.43 ± 0.39	0.0825 ± 0.0098	649.4 ± 25.8	1259 ± 215	48.4
176	0.21	645	86	0.14	12.27 ± 0.13	0.0535 ± 0.0017	505.0 ± 5.1	352 ± 70	-43.5
181	0.00	14	1	0.04	8.77 ± 0.45	0.0546 ± 0.0110	696.3 ± 34.1	397 ± 397	-75.4
183	0.00	1647	212	0.13	11.56 ± 0.13	0.0560 ± 0.0008	534.9 ± 6.0	455 ± 33	-17.6
184	0.00	960	113	0.12	11.51 ± 0.14	0.0567 ± 0.0013	537.1 ± 6.2	480 ± 49	-11.9
185	0.00	24	3	0.12	7.19 ± 0.32	0.0587 ± 0.0075	839.4 ± 35.5	556 ± 258	-51.0
186	0.00	591	67	0.12	11.42 ± 0.15	0.0590 ± 0.0016	541.0 ± 6.6	569 ± 58	4.9
187	0.00	14	4	0.30	9.68 ± 0.53	0.0636 ± 0.0116	633.8 ± 32.9	728 ± 345	12.9
191	0.27	36	6	0.16	10.07 ± 0.45	0.0713 ± 0.0089	610.4 ± 25.8	967 ± 235	36.9
192	0.00	507	58	0.12	12.04 ± 0.14	0.0569 ± 0.0017	514.2 ± 5.6	487 ± 65	-5.6
193	0.00	636	106	0.17	11.01 ± 0.15	0.0568 ± 0.0015	560.2 ± 7.4	484 ± 56	-15.8
194	0.00	670	76	0.12	11.19 ± 0.12	0.0570 ± 0.0016	551.8 ± 5.8	493 ± 60	-11.9
195	0.13	486	57	0.12	10.72 ± 0.14	0.0572 ± 0.0017	574.7 ± 7.0	501 ± 63	-14.7
196	0.09	480	70	0.15	11.27 ± 0.15	0.0581 ± 0.0020	547.9 ± 7.2	534 ± 72	-2.6
197	0.00	718	105	0.15	10.85 ± 0.15	0.0566 ± 0.0016	568.3 ± 7.4	475 ± 61	-19.6
198	0.00	736	74	0.10	11.79 ± 0.16	0.0563 ± 0.0013	524.8 ± 7.0	465 ± 51	-12.9
203	0.08	665	104	0.16	11.66 ± 0.14	0.0580 ± 0.0015	530.6 ± 5.9	531 ± 55	0.1
204	0.00	623	59	0.10	11.61 ± 0.16	0.0591 ± 0.0017	532.7 ± 7.1	571 ± 61	6.7
205	0.00	878	141	0.17	11.49 ± 0.13	0.0595 ± 0.0014	538.0 ± 6.0	584 ± 51	7.9
207	0.00	1135	173	0.16	11.39 ± 0.13	0.0597 ± 0.0011	542.3 ± 5.8	594 ± 38	8.7
208	0.00	34	2	0.06	9.57 ± 0.33	0.0518 ± 0.0069	640.9 ± 21.0	278 ± 279	-130.5
209	0.00	712	100	0.14	11.32 ± 0.15	0.0586 ± 0.0014	545.8 ± 6.8	553 ± 53	1.3
213	0.00	20	5	0.27	8.36 ± 0.37	0.0482 ± 0.0085	728.5 ± 30.2	109 ± 370	-568.4
214	0.00	36	9	0.24	9.46 ± 0.37	0.0714 ± 0.0066	647.6 ± 23.9	970 ± 179	33.2
215	0.04	1009	137	0.14	11.27 ± 0.14	0.0591 ± 0.0014	548.0 ± 6.6	573 ± 52	4.4
216	0.00	549	66	0.12	9.83 ± 0.12	0.0600 ± 0.0016	624.8 ± 7.0	605 ± 56	-3.3
217	0.00	1059	141	0.14	11.76 ± 0.14	0.0591 ± 0.0011	526.1 ± 5.9	570 ± 41	7.7
218	0.00	24	4	0.19	9.45 ± 0.44	0.0563 ± 0.0083	648.5 ± 28.5	467 ± 297	-38.9
219	0.00	32	5	0.15	10.63 ± 0.38	0.0498 ± 0.0066	579.7 ± 19.9	186 ± 281	-211.7
220	0.11	1607	198	0.13	12.64 ± 0.11	0.0586 ± 0.0012	490.7 ± 4.2	554 ± 43	11.4

Errors are 1-sigma; Pb_c and Pb* indicates the common and radiogenic portions, respectively.

[1] Common Pb corrected by assuming $^{206}Pb/^{238}U–^{208}Pb/^{232}Th$ age-concordance.

[2] The degree of discordance for an analyzed spot indicates the chronological difference between the two ages determined by Pb–Pb and U–Pb methods, and is defined as $\{1-(^{238}U/^{206}Pb^{*}\ \text{age})/(^{207}Pb^{*}/^{206}Pb^{*}\ \text{age})\}\times 100$ (%) (e.g., Song et al., 1996).

Table 13. Zircon REE data of metabasites from Tenmondai Rock and Sudare Rock, the LHC.

Spot No. (REE)	Spot No. (U-Pb)	La (ppm)	Ce (ppm)	Pr (ppm)	Nd (ppm)	Sm (ppm)	Eu (ppm)	Gd (ppm)	Tb (ppm)	Dy (ppm)	Ho (ppm)	Er (ppm)	Tm (ppm)	Yb (ppm)	Lu (ppm)
Ts11021106A															
003	8	0.117	1.313	0.154	1.178	0.896	0.287	1.334	0.349	3.287	0.723	2.565	0.456	3.695	0.747
004	10	0.016	0.458	0.022	0.087	0.183	0.166	1.572	0.397	2.488	0.639	2.329	0.367	3.465	0.743
005	18	0.063	1.019	0.166	1.018	0.450	0.355	0.667	0.245	1.184	0.305	0.933	0.158	1.557	0.285
007	32	0.003	0.146	0.003	-	0.214	0.328	2.361	0.728	5.179	0.892	1.814	0.237	1.229	0.187
009	83	0.008	0.448	0.018	0.144755	0.284	0.346	2.779	0.786	6.870	1.858	7.230	1.316	12.797	2.340
010	84	0.052	2.852	0.050	0.516	1.303	0.263	6.900	2.711	36.052	15.882	86.366	21.835	255.02	56.452
016	117	0.143	2.025	0.222	1.472	1.364	0.582	1.602	0.299	2.752	0.732	2.423	0.545	3.915	0.597
018	129	0.004	0.443	0.008	0.090	0.238	0.312	2.800	0.793	5.738	1.206	3.385	0.493	3.448	0.519
019	150	0.011	0.729	-	0.169	0.424	0.213	2.932	1.143	11.951	3.450	13.955	2.898	24.704	5.028
020	160	0.073	0.546	0.037	0.247	0.155	0.174	1.859	0.643	6.718	2.018	8.198	1.986	20.727	4.753
Ts11011002A															
003	5	-	2.449	0.003	0.097	0.516	0.325	1.900	0.729	9.199	2.956	12.272	2.044	16.547	2.794
004	7	0.008	1.798	0.016	0.129	0.084	0.246	2.245	0.703	7.007	2.155	8.233	1.258	11.307	1.934
007	11	0.000	2.546	0.011	0.035	0.236	0.253	2.178	0.783	9.109	3.046	12.474	2.336	19.787	3.423
008	16	-	2.220	0.008	0.153	0.364	0.277	2.919	0.956	11.868	4.537	21.418	4.473	42.626	8.052
010	18	0.294	3.229	0.106	0.960	0.826	0.254	2.236	0.672	6.838	2.483	9.314	1.826	14.847	2.725
013	22	-	1.692	0.008	0.077	0.389	0.128	1.425	0.466	6.124	2.031	9.169	1.737	15.334	2.296
015	28	0.000	2.300	0.002	0.202	0.590	0.278	1.992	0.693	5.999	1.709	5.882	1.053	6.287	0.863
016	29	0.007	3.117	0.006	0.112	0.130	0.250	2.279	0.867	9.503	2.725	11.560	1.592	17.109	2.637
017	31	0.048	2.685	0.019	0.326	0.273	0.093	1.608	0.591	7.846	2.570	11.388	2.290	22.300	3.915
018	32	0.015	2.922	0.021	0.354	0.521	0.312	2.277	0.870	12.067	3.658	15.508	3.015	25.978	4.706
020	33	0.016	1.810	0.013	0.104	0.469	0.262	1.693	0.699	8.652	2.422	8.176	1.484	10.962	1.998
024	40	-	1.461	0.004	0.180	0.052	0.142	1.651	0.627	5.715	1.814	6.968	1.189	10.986	1.652
026	43	0.016	2.480	0.005	0.263	0.564	0.202	2.124	0.810	11.632	4.867	22.114	4.875	47.909	9.565
028	51	0.003	1.808	0.014	0.072	0.726	0.219	1.882	0.628	5.273	1.976	5.995	1.005	6.656	0.781
033	59	0.000	2.420	0.004	0.257	0.230	0.109	1.992	0.816	9.224	3.239	11.813	1.902	19.833	3.723
034	55	-	2.925	0.028	0.233	0.660	0.551	3.400	1.247	13.474	3.963	14.591	2.922	20.411	3.088
036	60	0.009	0.273	-	0.108	0.104	0.098	0.697	0.302	3.315	0.941	3.835	0.704	6.222	1.261
037	62	0.006	2.786	0.006	0.219	0.658	0.336	2.207	1.098	11.592	3.498	11.837	2.000	17.049	2.780
038	99	0.348	4.466	0.490	3.788	2.793	0.785	5.136	1.492	20.716	8.308	38.020	7.765	82.153	16.464
039	65	-	2.682	0.009	0.283	0.332	0.240	1.970	0.762	7.895	2.792	10.705	1.950	14.005	2.753
040	72	0.052	3.053	0.062	0.738	0.806	0.355	2.809	1.164	10.568	3.227	11.379	1.867	14.343	2.411
050	85	0.007	2.379	0.006	0.344	0.148	0.228	2.638	1.460	16.726	8.171	38.001	8.761	89.184	19.014
053	87	-	1.706	0.001	0.003	0.434	0.180	1.665	0.537	7.256	2.068	6.852	1.089	10.004	1.788
056	95	-	0.117	0.006	0.026	0.059	0.055	0.415	0.192	3.272	1.325	5.110	0.833	8.163	1.198
057	96	0.006	2.809	0.013	0.133	0.554	0.188	1.776	0.764	8.080	2.423	9.045	1.480	10.945	1.613
058	97	-	1.615	0.001	0.289	0.349	0.207	1.835	0.528	5.253	1.628	7.243	1.006	8.712	1.217
066	147	0.001	2.605	0.015	0.187	0.567	0.308	2.498	0.826	10.495	3.222	11.530	1.958	15.679	2.904
067	109	0.006	2.617	0.015	0.019	0.414	0.106	2.022	0.775	7.718	2.943	11.789	2.301	18.705	3.419
078	131	0.012	2.500	0.015	0.271	0.199	0.090	2.700	1.335	17.098	7.404	34.688	6.871	70.003	13.367
079	132	0.204	3.278	0.095	0.632	0.538	0.232	1.109	0.620	6.169	2.164	9.478	1.726	18.020	3.191
083	18	0.001	3.075	0.006	0.234	0.160	0.264	3.467	1.185	10.092	3.311	11.243	1.557	13.010	1.891
086	141	0.002	1.182	0.016	0.171	0.212	0.258	1.694	0.867	8.967	3.230	14.719	3.354	31.423	6.900
087	142	-	2.539	0.005	0.160	0.238	0.160	2.455	0.844	11.472	4.642	21.959	5.031	49.031	9.909
088	150	0.006	2.615	0.012	0.067	0.485	0.134	2.394	0.813	8.579	2.843	11.447	1.725	16.536	2.693
099	164	0.006	2.391	0.006	0.190	0.556	0.250	2.721	0.954	9.750	3.357	14.436	2.611	22.444	3.912
104	172	0.004	1.543	0.004	-	0.518	0.329	1.721	0.653	7.719	2.510	10.969	2.419	22.385	4.690
106	174	-	3.431	-	0.400	0.266	0.519	1.821	0.941	10.713	2.992	11.994	2.087	15.740	2.784
115	186	0.017	0.655	0.012	0.129	0.127	0.110	0.953	0.564	7.286	2.523	11.486	2.179	21.803	4.431
119	192	0.221	3.495	0.246	1.427	1.237	0.473	2.971	0.955	8.701	2.970	8.221	1.783	12.857	2.381
120	196	0.037	3.076	0.026	0.231	0.636	0.408	2.839	1.010	10.284	3.749	12.566	2.468	23.557	4.049
127	203	-	3.559	0.002	0.210	0.545	0.487	3.256	1.262	12.896	3.356	11.864	1.920	13.641	2.224
130	207	-	2.999	0.017	0.357	0.236	0.314	2.953	1.180	11.093	3.577	12.290	2.074	17.203	2.534
137	215	-	2.597	0.016	0.248	0.476	0.330	3.107	1.122	10.817	4.154	16.594	3.154	29.366	5.071
138	216	0.007	2.823	0.011	0.153	0.812	0.253	4.012	0.978	13.742	4.758	15.768	2.899	22.027	4.514